SLAC-248
UC-34
(A)

OPTICAL PUMPING AND PHOTOLUMINESCENCE DETECTION OF SPIN-POLARIZED ELECTRONS IN UNIAXIALLY STRESSED GALLIUM ARSENIDE*

Paul Zorabedian
Stanford Linear Accelerator Center
Stanford University
Stanford, California 94305

March 1982

Prepared for the Department of Energy

under contract number DE-AC03-76SF00515

Printed in the United States of America. Available from National Technical Information Service, U.S. Department of Commerce, 5285 Port Royal Road, Springfield, VA 22161. Price: Printed Copy - A06; Microfiche - A01.

---

* Ph.D. dissertation.

ABSTRACT

This work describes the development and application of an optical pumping and photoluminescence experiment for electron spin polarization measurements on semiconductor photocathode materials. We discuss the spin polarization increase that is produced by applying a uniaxial compression to a gallium arsenide crystal and selectively optically pumping the transition between the upper strain-split valence band and the conduction band.

The electron spin polarization is measured by analysing the circular polarization of the photoluminescence. The relation between luminescence and spin polarizations is given by

$$P_\sigma = P_h P_s \frac{\tau_s}{\tau_s + \tau_r}$$

where P_σ is the luminescence circular polarization, P_s is the spin polarization, and P_h is the hole coupling factor. For band edge excitation P_h is identical to P_s. In this expression, τ_s and τ_r are the spin relaxation and luminescence recombination times, respectively. From our data we infer an increase in P_s from 50% at zero stress to 70% for an applied [001] stress of 4.0×10^9 dyn cm^{-2} in a 1×10^{18} p-type GaAs crystal at T = 100°K. For comparison, the maximum theoretical polarization at infinite stress is 80%.

Our results show that the observed increase in polarization can be fit to a model function of the ratio δ_s/E_k where δ_s is the strain splitting energy and E_k is the energy of the initial valence state measured from the band edge. For band edge excitation the best-fit value for E_k of 0.017 eV agrees reasonably well with the calculated value of V_{rms}, the rms potential energy fluctuation of the band edge due to the ionized impurity potentials. From the known dependence of V_{rms} on doping and temperature, device operating curves are proposed which predict the relation between spin polarization and applied stress for various values of impurity concentration p and temperature T.

The tunable infrared dye laser that was built to optically pump the gallium arsenide samples is compatible with the pulsed operation of the gallium arsenide spin-polarized electron source at SLAC. We give tuning curves and discuss the operating characteristics of this laser.

ACKNOWLEDGEMENTS

The authors wishes to thank his research advisor, Dr. Edward L. Garwin, for providing the resources of the Physical Electronics Group at SLAC in support of this work and for valuable suggestions on the design of experimental apparatus and presentation of results, and Dr. Charles K. Sinclair for the use of the flashlamp dye laser, for many suggestions on matters of vacuum, optics, and electronics, and for a critical reading of the manuscript. He also wishes to acknowledge the support of Mssrs. Jerry Collet, Jack Humphries, and Don Fraser for technical assistance, Mrs. Deborah Phillips for typing much of the initial draft, and Mr. Tony Roder for facilitation in general; also the contributions of many others, too numerous to mention individually, on Dr. Garwin's and Dr. Sinclair's staffs, in the SLAC Central Lab Machine Shop, Library, Technical Illustrations, and Technical Typing.

Finally, an expression of appreciation and gratitude goes to many students and faculty of the Ginzton Laboratory of Applied Physics at Stanford for their advice, encouragement, and the loan of several essential pieces of apparatus.

TABLE OF CONTENTS

Chapter		Page
I	INTRODUCTION	1
II	BAND STRUCTURE OF GALLIUM ARSENIDE	6
	2.1. Overview	6
	2.2. The k•p Method	9
	2.3. Interaction Matrices for k•p, Spin-Orbit and Strain	11
	2.4. Band Structure Near Γ	18
	2.5. Model Wave Function for the Complete Hamiltonian	21
III	OPTICAL PUMPING AND POLARIZED PHOTOLUMINESCENCE . .	24
	3.1. Density Matrix Description of Electron Spin Polarization	24
	3.1.1. General formalism	24
	3.1.2. Density matrix for interband optical absorption	25
	3.2. Spin Polarization for Optical Pumping Near the Band Gap	31
	3.3. Luminescence Polarization	33
IV	EXPERIMENTAL EQUIPMENT	38
	4.1. System Overview	38
	4.2. GaAs Sample Preparation	38
	4.3. Uniaxial Stress Apparatus	42
	4.4. Tunable Infrared Dye Laser	47
	4.5. Optical System	52
	4.6. Detection Electronics	60

Chapter		Page
V	DATA AND DISCUSSION	64
	5.1. Photoluminescence Lineshape	64
	5.1.1. Recorded spectra	64
	5.1.2. Relation between luminescence and absorption spectra	66
	5.1.3. Determination of absorption edge from luminescence spectrum	68
	5.2. Strain Splitting of Linearly Polarized Photoluminescence	70
	5.2.1. Recorded spectra	70
	5.2.2. Valence band strain splitting	74
	5.3. Stress and Spectral Dependence of Polarized Luminescence	79
	5.3.1. Complete spectra	79
	5.3.2. Circular polarization at low stress	81
	5.3.3. Circular polarization at high stress	81
	5.3.4. Stress dependence of maximum luminescence polarization	85
	5.4. Spin Polarization Analysis of Polarized Luminescence	88
	5.4.1. Approach	88
	5.4.2. Spin relaxation	88
	5.4.3. Hole coupling factor	89
	5.4.4. Electron spin polarization	90
	5.5. Calculation of V_{rms}	98
	5.6. Effect of Self Absorption on the Polarization of Photoluminescence	99
VI	CONCLUSIONS	102
	6.1. Polarization vs Stress Operating Curves	102
REFERENCES*		108

LIST OF ILLUSTRATIONS

Fig. 2.1. Band structure and constant energy surfaces for GaAs without strain (a), and with uniaxial strain (b).

Fig. 3.1. Conventions for designating optical polarization.

Fig. 3.2. Dependence of spin polarization on angle between the spin quantization axis of the initial state wave functions and the pump beam direction.

Fig. 3.3. Dependence of spin polarization on the parameter ratio δ/E for optical pumping of light-hole (V2) and heavy-hole (V1) valence bands at 90^{o} to the stress axis.

Fig. 3.4. Dependence of spin polarization on δ/E for optical pumping parallel to the stress axis.

Fig. 4.1. Photographs of the diamond wire saw and translation stage (a) and the polishing disc (b) used for preparation of GaAs samples.

Fig. 4.2. Drawing of the low temperature stress apparatus.

Fig. 4.3. Photograph of stress apparatus.

Fig. 4.4. Near infrared dye laser resonator and optical system.

Fig. 4.5. Dye laser tuning curves for optical pumping at 705nm.

Fig. 4.6. Oscilloscope traces of flashlamp and i.r. dye laser pulses at 0.5 μsec/div (a), and gated integrator input and output signals at 2.0 μsec/div.

Fig. 4.7. Ray tracing of luminescence beam through the imaging telescope.

Fig. 4.8. Schematic of circular polarization asymmetry caused by a fixed retardation plate when the input beam polarization is reversed.

Fig. 4.9. Block diagram of signal detection electronics.

Fig. 5.1. Photoluminescence spectra for laser excitation at 6328Å (a), and 8200Å (b).

Fig. 5.2. Absorption edge calculated from measured luminescence spectrum by the van Roosbroeck-Shockley relation. Luminescence spectrum corrected for PMT sensitivity.

Fig. 5.3. Linearly polarized luminescence components at low stress.

Fig. 5.4. Linearly polarized luminescence components at intermediate stress.

Fig. 5.5. Linearly polarized luminescence components at high stress.

Fig. 5.6. Stress splitting of polarized luminescence peaks.

Fig. 5.7. Stress splitting of upper $P_{3/2}$ valence band edges.

Fig. 5.8. Spectra of circularly polarized luminescence components (hand-smoothed) for optical pumping at 8217Å at high stress.

Fig. 5.9. Dependence of circular polarization at luminescence peak on laser photon energy at low stress. Open circles, $\sigma+$ excitation; filled circles, $\sigma-$ excitation.

Fig. 5.10. Dependence of circular polarization at luminescence peak on laser photon energy at high stress. Open circles, σ_+ excitation; filled circles, σ_- excitation.

Fig. 5.11. Spectral dependence of luminescence polarization at high stress for several laser wavelengths (the luminescence peak is at ≃ 8300Å).

Fig. 5.12. Stress dependence of circular polarization at the luminescence peak for optical pumping at 8220Å. Open circles, σ_+ excitation, filled circles, σ_- excitation.

Fig. 5.13. Model of spatially fluctuating band edges due to ionized impurities and the resulting density of states band tails.

Fig. 5.14. Model of stress-split absorption edges.

Fig. 5.15. Spin polarization calculated from luminescence polarization data and theoretical spin polarization curves for several values of the kinetic energy parameter of Eq. (3.17a).

Fig. 6.1. Spin polarization vs compressive stress for band edge optical pumping at 90^{o} to the stress axis.

Fig. 6.2. Spin polarization vs tensile stress for band edge optical pumping parallel to the stress axis.

Chapter I

INTRODUCTION

Spin-polarized conduction electrons produced by optical pumping of direct band gap III-V semiconductors of the zinc blende structure can be detected by measuring the degree of circular polarization of recombination luminescence.[1,58,73] The electron spin polarization P_s is defined as

$$P_s = \frac{n\uparrow - n\downarrow}{n\uparrow + n\downarrow} \qquad (1.1)$$

where $n\uparrow(n\downarrow)$ is the number of electrons with spin parallel (antiparallel) to the direction of the incident beam of circularly polarized light. Spin-polarized electrons are generated by the transfer of angular momentum from the absorbed photons to the electrons. The degree of spin polarization is governed by dipole selection rules which depend on the crystal symmetry and the point in $\vec{k}$-space at which the electrons are excited. Although nonzero values of P_s are possible at several symmetry points in $\vec{k}$-space, its value at the Γ point, where $k = 0$, was the first observed and has been intensely studied in experiments on spin relaxation dynamics. The value of $P_s(k = 0)$ is 0.5 or 50% in zinc blende crystals at the instant of excitation. Measurement of luminescence circular polarization P_σ gives the ratio of τ_s, the spin relaxation time, to τ_r, the recombination time. Application of a transverse magnetic field (Hanle effect) allows the independent determination of τ_s and τ_r.

A new technical importance has been given to optically pumped semiconductors by the fact that a high quantum yield for photoemission is exhibited by crystals which have been activated to negative electron affinity (NEA) by a monolayer coating of Cs and O in an ultrahigh vacuum environment on an atomically clean surface. The combination of a large spin polarization and efficient photoemission at Γ led to the proposal that an optically pumped NEA GaAs cathode could be used as an intense source of spin-polarized electrons.[2] Photoemission of spin-polarized electrons from GaAs was subsequently observed.[3] Laboratory sources of spin-polarized electrons using GaAs cathodes have been constructed and used to obtain significant results from studies of parity violation in the deep inelastic scattering of polarized electrons from hydrogen and deuterium targets,[35] polarized low energy electron diffraction (PLEED) on ferromagnetic surfaces, and of spin-orbit and spin-exchange effects in atomic physics.[4] After the initial development of the GaAs polarized source, photoemission of spin polarized electrons from $ZnSiAs_2$ and $ZnGeAs_2$, crystals with the chalcopyrite structure, was observed although spin polarization had not previously been optically detected.[5] GaAs photoemission sources are capable of producing an electron beam polarization of $\simeq$40%. Sources operating with even higher spin polarizations, ideally 100%, are clearly very desirable, especially in experiments in which the spin-dependence of the observed quantities is very weak.

The requirements for developing new spin-polarized photocathode materials can be understood within the framework of the three-step model for photoemission introduced by Spicer.[6] The three steps consist of optical excitation in the bulk, transport to the surface, and finally

escape across the surface into the vacuum. In the excitation step, the initial spin polarization $P_s(k)$ is determined by the photon energy $h\nu$ which in turn selects $\vec{k}$ according to the relation

$$h\nu = E_c(\vec{k}) + E_g - E_v(\vec{k}) \qquad (1.2)$$

where E_v and E_c are the initial and final state energies measured from their respective band edges. Vertical transitions in $\vec{k}$-space are assumed. During transport, spin relaxation can occur. Finally, during escape across the surface, spin flip via spin exchange with atoms in the activation layer is possible. Thus, the photoemission process may be viewed as two successive bulk processes followed by a surface process, any of which can affect the final spin polarization.

To evaluate other semiconductors for use as spin-polarized cathodes, one can use band structure models to select a potential semiconductor crystal and an appropriate excitation energy $h\nu$, cool the crystal to increase the spin relaxation time, and develop a suitable NEA surface activation process to allow spin-polarized electrons to escape from the surface. It should be noted that spin-polarized cathodes generally require large p-type doping densities, typically $\underline{5} \times 10^{18}$ cm^{-3} to 4×10^{19} cm^{-3}, to achieve band bending which assists the lowering of the vacuum level and to minimize the bending width in which hot electron scattering into adjacent X and L minima can occur.

We have pursued photoluminescence detection of conduction electron spin polarization as a means to evaluate photocathode materials prior to NEA photoemission experiments. Since photoluminescence can usually be treated as a purely bulk phenomenon, it allows the study of the optical

pumping and spin relaxation processes without regard to surface activation or spin-flip. The purely optical technique also offers considerable experimental simplicity over a photoemission experiment. The spin polarization measured by photoluminescence is in general lower than the photoemitted spin polarization, if surface depolarization is not significant. This is simply because photoemitted electrons spend less time inside the crystal than do electrons which finally recombine. Thus, a crystal that shows a high spin polarization by photoluminescence should be a promising candidate for polarized source development. The question of surface spin depolarization has not been completely resolved, and differing accounts of its severity have appeared.[7,8] The more complete study,[8] in which the spin polarization was measured before and after photoemission using the same crystal, reports no observable surface spin depolarization. For gallium arsenide, the two types of measurements agree within a few percent at 100°K.

In this work, we describe the band edge optical pumping and photoluminescence detection of spin-polarized electrons in crystals of gallium arsenide subjected to large uniaxial deformations. As we will describe, the changes in the band structure which result from the strain can lead to a significant increase in the spin polarization when the sign and orientation of the stress and the photon energy $h\nu$ of the pump light are suitably chosen.[9,10] The stressed gallium arsenide experiment we performed makes use of commercially available single crystal material and is compatible with existing GaAs polarized electron source technology. Furthermore its band structure serves as a model for chalcopyrite semiconductors and, more directly, for epitaxially grown films which are

strained due to lattice mismatch with their substrates. The experiment we used gave control over the amount of stress, which was valuable in correlating data and model calculations. Thus the technique allowed flexibility to obtain information that should be useful in future polarized source development work.

In Chapter II we discuss the band structure of gallium arsenide and the effects of strain within the Kane[12] band model. A model wave function is proposed to characterize the angular momentum properties of valence electrons in states affected by both strain and k·p terms in the Hamiltonian. In Chapter III the spin density matrix formalism is presented and applied to the model wave function to compute the strain and kinetic energy dependence of the optically pumped spin polarization. Chapter IV gives a description of the experimental equipment, and Chapter V discusses the experimental data. In Chapter VI a comparison between the data and the model is presented.

Chapter II

BAND STRUCTURE OF GALLIUM ARSENIDE

2.1. Overview

In this chapter we discuss the band structure of gallium arsenide near Γ within the framework of the k•p representation of the one-electron eigenvalue equation. This method has been described by several authors.[11-13] Anticipating the solutions we shall outline in this chapter, the band structures of gallium arsenide with and without an external strain are shown schematically in Fig. 2.1. The doubly degenerate valence bands are labeled in the notation V_1, V_2, V_3 which corresponds, at zero strain, to the commonly used labels of heavy-hole, light-hole, and spin orbit-split bands, respectively. The distinction with respect to effective mass disappears under large deformations. In this connection, Fig. 2.1 also shows the shapes of the surfaces of constant energy, which determine the density of states effective masses.

Explicit eigenfunctions for the conduction and valence bands are necessary to calculate the spin polarization produced by optical pumping. The conduction band wave functions have the symmetry of s-orbitals and are assumed to be unaffected by strain. The valence band wave functions are derived from p-orbitals with an admixture of s-character. We shall show that the nature of the linear combination of atomic-like orbitals which describe the cell-periodic portion of the valence band Bloch functions changes markedly with strain. It is this stress-related

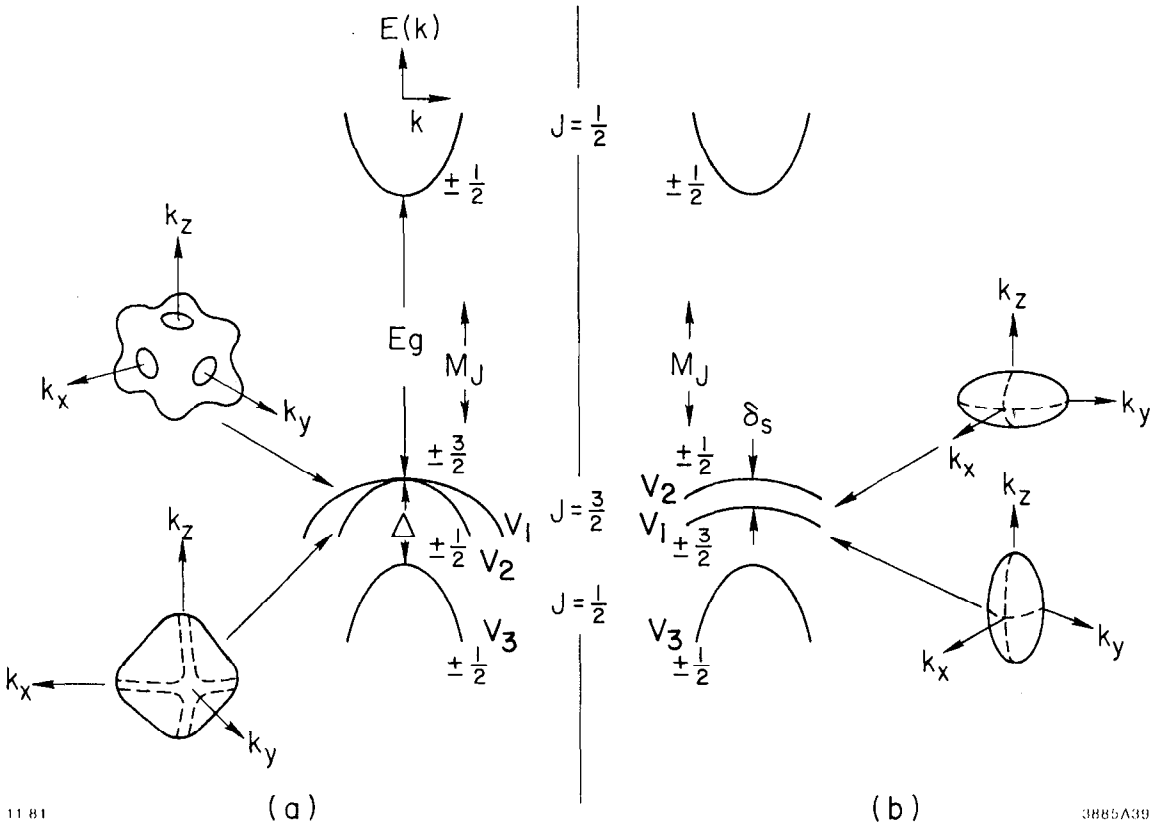

Fig. 2.1. Band structure and constant energy surfaces for GaAs without strain (a), and with uniaxial strain (b).

property that allows the spin polarization to be altered from its zero strain value depending on the relative orientation of the optical and strain fields and the sign of the strain.

The standard treatment of direct bandgap III-V semiconductor band structure is the model introduced by Kane to describe InSb.[12] Within this model, exact solutions exist for the valence band eigenfunctions in the limits of zero and "infinite" strain. The intermediate case is, however, analytically intractable. We have found no published calculations which are useful in considering eigenstates for which the strain and kinetic energy contributions to the Hamiltonian are comparable. Although a numerical solution is in principle possible, it requires diagonalization of an 8×8 matrix with no simplication possible for arbitrary $\vec{k}$-direction, and the symmetry properties would be unidentifiable from such a calculation. We therefore present a model form for the wave functions of the V_1 and V_2 bands which is a linear combination of the limiting case eigenfunctions of known transformational properties.

We also give a discussion of the effect of strain on the V_1 and V_2 constant energy surfaces near $k = 0$. This material is introduced because it affects the application of existing band-tail models to stressed gallium arsenide crystals. These models and their relation to the problem of spin polarization by optical pumping will be discussed in Chapter VI.

2.2. The k•p Method

In the single electron approximation, the eigenvalue equation for an electron moving in a periodic potential $V(\vec{r})$ is given by

$$H\psi_n = \left\{ \frac{p^2}{2m} + V(\vec{r}) \right\} \psi_n = E_n \psi_n \, . \tag{2.1}$$

Introducing the Bloch wave function

$$\psi_n = e^{i\vec{k}\cdot\vec{r}} \, u_{nk}(\vec{r}) \tag{2.2}$$

where $u_{nk}(\vec{r})$ has the periodicity of the crystal lattice, Eq. (2.1) becomes

$$\left\{ \frac{p^2}{2m} + \frac{\hbar}{m} \vec{k}\cdot\vec{p} + \frac{\hbar^2 k^2}{2m} + V \right\} u_{nk} = E_n u_{nk} \, . \tag{2.3}$$

It is well known that the functions u_{nk} form a complete set for any fixed $\vec{k}$. Since the eigenvalues and eigenstates near $k = 0$ are of interest, the chosen basis is taken to be the set of functions which are the solutions to the equation

$$H_o u_{no} = \left\{ \frac{p^2}{2m} + V \right\} u_{no} = E_{no} u_{no} \, . \tag{2.4}$$

The solutions to Eq. (2.3) are expanded in the basis formed by the solutions to Eq. (2.4)

$$u_{nk} = \sum_{n'} c_{nn'}(k) \, u_{n'o} \, . \tag{2.5}$$

Substituting Eq. (2.5) in Eq. (2.3), multiplying both sides of the result by u_{no}, and integrating over the unit cell, the resulting matrix eigenvalue equation is

$$\sum_{n'} \left[\left(E_{no} + \frac{\hbar^2 k^2}{2m} \right) \delta_{nn'} + \frac{\hbar}{2m} k \cdot P_{nn'} \right] c_{nn'} = E_{nk} c_{nn} \qquad (2.6a)$$

where

$$P_{nn'} = \int_{\text{unit cell}} u^*_{no}(r) \, Pu_{n'k}(r) \, dr \, . \qquad (2.6b)$$

The general method used to solve Eq. (2.6) is known as Löwdin perturbation theory.[14] The basis states are separated into two classes, A and B, in which states in A interact strongly with each other, but only weakly with states in B. The solution proceeds in two steps. First, the interaction between A and B is removed by normal perturbation theory. Second, the remaining interaction matrix within the A manifold is diagonalized exactly.

The transformation properties of the solutions of Eq. (2.4) are determined by the symmetry of the crystal lattice. For states adjacent to the band gap in diamond or zinc-blende lattices, the basis of strongly interacting states are the functions S, X, Y, and Z, which have the symmetry properties of s- and p-orbitals. In the following sections we review the application of this procedure to the band structure of gallium arsenide and its extension to include spin-orbit and strain terms.

2.3. Interaction Matrices for k·p, Spin-Orbit and Strain

In the absence of spin-orbit or strain terms, the interaction matrix within the s-p manifold is given by

$$
H_{k\cdot p} = \begin{array}{c} \\ S \\ \\ X \\ \\ Y \\ \\ Z \end{array}
\begin{bmatrix}
\begin{array}{c} Ak^2 + E_c \\ + \frac{\hbar^2 k^2}{2m} \end{array} & \begin{array}{c} Bk_y k_z \\ + iPk_x \end{array} & \begin{array}{c} Bk_x k_z \\ + iPk_y \end{array} & \begin{array}{c} Bk_x k_y \\ + iPk_z \end{array} \\
\begin{array}{c} Bk_y k_z \\ - iPk_x \end{array} & \begin{array}{c} L^2 k_x^2 + M(k_y^2 + k_z^2) \\ + E_V + \frac{\hbar^2 k^2}{2m} \end{array} & Nk_x k_y & Nk_x k_z \\
\begin{array}{c} Bk_x k_y \\ - iPk_y \end{array} & Nk_x k_y & \begin{array}{c} L^2 k_y^2 + M(k_x^2 + k_z^2) \\ + E_V + \frac{\hbar^2 k^2}{2m} \end{array} & Nk_y k_z \\
\begin{array}{c} Bk_x k_y \\ -iPk_z \end{array} & Nk_x k_z & Nk_y k_z & \begin{array}{c} L^2 k_z^2 + M(k_x^2 + k_y^2) \\ + E_V + \frac{\hbar^2 k^2}{2m} \end{array}
\end{bmatrix}
\tag{2.7}
$$

The definitions of the constants A, B, L, M, and N, representing the first step of the Löwdin procedure, are given by Kane.[12] In a semi-empirical approach, they are related to mass constants which can be determined from cyclotron resonance measurements. The constant P is given by the matrix element of the momentum operator

$$P = -i \frac{\hbar}{m} \langle S|P_z|z\rangle \ . \tag{2.8}$$

The definition is chosen so that P is real and positive.

The spin-orbit interaction plays an important role in the band structure of diamond and zincblende crystals; it provides the essential coupling between the spin and orbital parts of the wave function that makes possible the orientation of conduction electron spins by optical absorption of circularly polarized light. When spin is considered, the fourfold s-p basis becomes the 8-dimensional set

$$S\uparrow,\ S\downarrow,\ X\uparrow,\ X\downarrow,\ Y\uparrow,\ Y\downarrow,\ Z\uparrow,\ Z\downarrow \ .$$

In the diamond lattice, inversion symmetry guarantees double degeneracy of $\pm M_j$ (Kramers' degeneracy). In zincblende the Kramers' doublets are split, but only by small amounts, and Kramers' degeneracy shall be assumed in GaAs as well. The spin-orbit Hamiltonian is given by

$$H_{so} = \frac{\hbar}{4m^2c^2} [\nabla V \times \vec{p}]\cdot\vec{\sigma} \tag{2.9a}$$

which generates two terms when added to the k•p Hamiltonian of Eq. (2.1)

$$H_{so}^1 = \frac{\hbar}{4m^2c^2} [\nabla V \times \vec{p}]\cdot\vec{\sigma} \tag{2.9a}$$

$$H_{so}^2 = \frac{\hbar}{4m^2c^2} [\nabla V \times \vec{k}]\cdot\vec{\sigma} \ . \tag{2.9b}$$

H_{so}^2 shall be neglected because it is small compared to H_{so}^1 since $\hbar k$ is

small compared to p in the interior of the atom where most of the spin-orbit interaction occurs. In direct band gap compounds, an accurate treatment of the valence band wave functions requires the simultaneous diagonalization of the k·p and spin-orbit interactions within the full 8-dimensional manifold. Kane obtained this solution by transforming to the basis

$$|iS\downarrow\rangle' \;,\quad \left|\frac{(X-iY)\uparrow}{\sqrt{2}}\right\rangle' \;,\quad |Z\downarrow\rangle' \;,\quad \left|\frac{(X+iY)\uparrow}{\sqrt{2}}\right\rangle'$$

$$|iS\uparrow\rangle' \;,\quad \left|-\frac{(X+iY)\downarrow}{\sqrt{2}}\right\rangle' \;,\quad |Z\uparrow\rangle' \;,\quad \left|\frac{(X-iY)\downarrow}{\sqrt{2}}\right\rangle'$$

in which the first four functions are degenerate with the last four. The primes indicate that the coordinate system is not defined by the crystal lattice but by a set of orthogonal axes with the z' axis along $\vec{k}$. The transformations between the primed and unprimed functions are given by

$$\begin{bmatrix} \uparrow' \\ \downarrow' \end{bmatrix} = \begin{bmatrix} e^{-i\phi/2}\cos\frac{\theta}{2} & e^{i\phi/2}\sin\frac{\theta}{2} \\ -e^{-i\phi/2}\sin\frac{\theta}{2} & e^{i\phi/2}\sin\frac{\theta}{2} \end{bmatrix} \begin{bmatrix} \uparrow \\ \downarrow \end{bmatrix}$$

$$\begin{bmatrix} X' \\ Y' \\ Z' \end{bmatrix} = \begin{bmatrix} \cos\theta\cos\phi & \cos\theta\sin\phi & -\sin\theta \\ -\sin\phi & \cos\phi & 0 \\ \sin\theta\cos\phi & \sin\theta\sin\phi & \cos\theta \end{bmatrix} \begin{bmatrix} X \\ Y \\ Z \end{bmatrix} \qquad (2.10)$$

$$S' = S$$

where θ and ϕ are the polar angles of z' with respect to a z-axis which is fixed in the crystal. We will take z to be defined by the optical pumping beam. With respect to this basis, the interaction matrix for the k·p and spin-orbit terms becomes

$$H_{k\cdot p} + H_{so} = \begin{bmatrix} H' & 0 \\ 0 & H' \end{bmatrix} \tag{2.11a}$$

where

$$H' = \begin{bmatrix} E_g & 0 & kP & 0 \\ 0 & -\frac{2}{3}\Delta & \frac{\sqrt{2}}{3}\Delta & 0 \\ kP & \frac{\sqrt{2}}{3}\Delta & -\frac{1}{3}\Delta & 0 \\ 0 & 0 & 0 & 0 \end{bmatrix} \tag{2.11b}$$

and

$$\Delta = \frac{3\hbar i}{4m^2c^2} \langle X \mid \frac{\partial V}{\partial x} P_y - \frac{\partial V}{\partial y} P_x \mid Y \rangle \tag{2.11c}$$

Δ = 0.34 eV in GaAs.[15] The matrix element P is nearly constant for III-V semiconductors and has the value $P = (\hbar^2/2m) \times 20$ eV.[16] The matrix H' is diagonal in the $|JM_J\rangle$ representation. The spin-orbit interaction is completely isotropic; in the absence of strain, the P term effectively orients the axis of angular momentum quantization along the linear momentum vector even for small k values. The eigenfunctions and their eigenvalues at k = 0 are displayed in Table 2.1.

TABLE 2.1

Multiplet	$\|JM_J\rangle$	$\psi(\vec{r})$	E(k=0)
$S_{1/2}$	$\|1/2,\ 1/2\rangle$	$S\uparrow$	E_g
	$\|1/2,-1/2\rangle$	$S\downarrow$	E_g
$P_{3/2}$	$\|3/2,\ 3/2\rangle$	$\frac{1}{\sqrt{2}}(X'+iY')\uparrow'$	0
	$\|3/2,\ 1/2\rangle$	$-(2/3)^{1/2}\ Z'\uparrow' + \frac{1}{\sqrt{6}}(X'+iY')\downarrow'$	0
	$\|3/2,-1/2\rangle$	$-(2/3)^{1/2}\ Z'\downarrow' - \frac{1}{\sqrt{6}}(X'-iY')\uparrow'$	0
	$\|3/2,-3/2\rangle$	$-\frac{1}{\sqrt{2}}(X'-iY')\downarrow'$	0
$P_{1/2}$	$\|1/2,\ 1/2\rangle$	$\frac{1}{\sqrt{3}}(X'+iY')\downarrow' + \frac{1}{\sqrt{3}}Z'\uparrow'$	$-\Delta$
	$\|1/2,-1/2\rangle$	$-\frac{1}{\sqrt{3}}Z'\downarrow' + \frac{1}{\sqrt{3}}(X'-iY')\uparrow'$	$-\Delta$

These eigenfunctions can be written in the following notation:[8]

$$\psi_M = \sum_\mu u_\mu D^J_{\mu M}(\theta,\phi) \tag{2.12}$$

where u_μ is a Bloch wave function corresponding to $M_j = \mu$ ($\mu = \pm 1/2$ or $\pm 3/2$), D^J is the finite rotation matrix for angular momentum J, and θ and ϕ are the polar angles of the angular momentum quantization axis z' (in this case $\vec{k}$) with respect to a fixed z axis in the crystal.

Mechanical deformation can introduce important changes into the energy bands and symmetries of the wave functions near k=0. The Hamiltonian for the deformed crystal must be expressed in terms of the undeformed coordinates so that perturbation theory can be applied using the basis functions of the undeformed lattice. This procedure introduces terms into the Hamiltonian of the form:[17,18]

$$D = \sum_{ij} D_{ij}\, \varepsilon_{ij} \tag{2.13a}$$

$$D_{ij} = \frac{\hbar^2}{m} \frac{\partial^2}{\partial x_i \partial x_j} + V_{ij} - \frac{\hbar}{m} P_i k_j \tag{2.13b}$$

$$V_{ij}(r) = \frac{\partial}{\partial \varepsilon_{ij}} V\big((1+\hat{\varepsilon})\cdot r\big)\Big|_{\hat{\varepsilon}\to 0} \tag{2.13c}$$

where the ε_{ij}'s are the components of the strain tensor $\hat{\varepsilon}$.[19] The form of the interaction matrix can be written down by symmetry considerations. For an uniaxial strain, it shall be assumed that only the interactions between the X, Y and Z basis functions need be considered because the anisotropy in the strain tensor $\hat{\varepsilon}$ will be sufficient to orient the valence band wave functions. Within this basis, the strain

interaction matrix D takes the form

$$D = \begin{bmatrix} -a\varepsilon + b(3\varepsilon_{xx}-\varepsilon) & d\varepsilon_{xy} & d\varepsilon_{xz} \\ d\varepsilon_{xy} & -a\varepsilon + b(3\varepsilon_{yy}-\varepsilon) & d\varepsilon_{yz} \\ d\varepsilon_{xz} & d\varepsilon_{yz} & -a\varepsilon + b(3\varepsilon_{zz}-\varepsilon) \end{bmatrix} \quad (2.14)$$

where $\varepsilon = \mathrm{Tr}\,\hat{\varepsilon}$, and a, b, and d are deformation potentials which determine the shift and splitting of the valence bands at k=0. These effects have been extensively studied by the technique of electroreflectance spectroscopy.[20,21] Specializing to uniaxial strain along the [001] axis, the components of the strain tensor are given by

$$\begin{aligned} \varepsilon_{zz} &= S_{11}\chi \\ \varepsilon_{xx} &= \varepsilon_{yy} = S_{12}\chi \\ \varepsilon_{xy} &= \varepsilon_{xz} = \varepsilon_{yz} = 0 \end{aligned} \quad (2.15)$$

where S_{11} and S_{12} are elastic compliance constants and χ is the uniaxial stress. Calculated values for GaAs are $S_{11} = 1.173$ and $S_{12} = -0.366$ (units of 10^{-12} dyn^{-1} cm^2).[22]

The basis functions for the valence band states are taken as the set of $|JM_J\rangle$ functions which diagonalize the spin orbit interaction. Using wave functions referred to the [001] direction, the Hamiltonian matrix for the valence bands at Γ becomes

$$D + H_{so} = \begin{array}{c} \begin{matrix} V_1 & V_2 & V_3 \end{matrix} \\ \begin{bmatrix} \frac{1}{3}\Delta - \delta_H - \frac{1}{2}\delta_S & 0 & 0 \\ 0 & \frac{1}{3}\Delta - \delta_H + \frac{1}{2}\delta_S & \frac{\sqrt{2}}{2}\delta_S \\ 0 & \frac{\sqrt{2}}{2}\delta_S & -\frac{2}{3}\Delta - \delta_H \end{bmatrix} \end{array} \quad (2.16)$$

where $\delta_H = a(S_{11} + 2S_{12})\chi$ is the shift of the band gap due to the hydrostatic component of the strain, and $\delta_S = 2b(S_{11} - S_{12})\chi$ is the linear splitting of the V_1 and V_2 bands at Γ due to the shear strain.

For $\delta_S << \Delta$ the mixing of the V_2 and V_3 bands can be neglected. The resulting interaction matrix for spin-orbit and strain at $k = 0$ is diagonalized by $|JM_J\rangle$ states quantized along the strain axis. The "center of gravity" of the $P_{3/2}$ multiplet shifts by δ_H and the fourfold degeneracy at Γ splits by δ_S into two doubly degenerate bands. The valence wave functions are again given by Eq. (2.12), but in this case θ and ϕ are the polar angles of the strain axis.

Pollak and Cardona[20] report the values $\delta_H = 3.8 \pm 0.2$ meV/kbar and $\delta_S = 6.2 \pm 0.3$ meV/kbar. For compressive strain, the V_2 band moves up, and the V_1 band moves down in energy with respect to their average energy.

2.4. Band Structure Near Γ

Under the restrictions that $\hbar^2k^2/2m\Delta << 1$ and $\delta_S/\Delta << 1$, approximate energy eigenvalues for the upper valence bands are obtained by diagonalizing the k·p, spin-orbit, and strain interactions within the four-fold $P_{3/2}$ multiplet. Pikus and Bir[18] give the following

eigenvalues:

$$E_{1,2}(k) = Ak^2 + a\varepsilon \pm \left[\varepsilon_k + \varepsilon_{sk} + \varepsilon_s\right]^{1/2} \tag{2.17a}$$

where ε_k, ε_s, and ε_{sk} are given by

$$\varepsilon_k = B^2k^4 + C^2\left(k_x^2k_y^2 + k_x^2k_z^2 + k_y^2k_z^2\right) \tag{2.17b}$$

$$\varepsilon_s = \frac{b^2}{2}\left[\left(\varepsilon_{xx} - \varepsilon_{yy}\right)^2 + \left(\varepsilon_{xx} - \varepsilon_{zz}\right)^2 + \left(\varepsilon_{yy} - \varepsilon_{zz}\right)^2\right] + d^2\left(\varepsilon_{xy}^2 + \varepsilon_{xz}^2 + \varepsilon_{yz}^2\right) \tag{2.17c}$$

$$\varepsilon_{sk} = Bb\left[3\left(k_x^2\varepsilon_{xx} + k_y^2\varepsilon_{yy} + k_z^2\varepsilon_{zz}\right) - k^2\varepsilon\right] + 2Dd\left(k_xk_y\varepsilon_{xy} + k_xk_z\varepsilon_{xz} + k_yk_z\varepsilon_{yz}\right) \tag{2.17d}$$

where the relations between the coefficients C and D in Eq. (2.17) and the components of the k•p interaction matrix in Eq. (2.7) are defined by

$$C^2 = \frac{1}{3}\left[N^2 - (L-M)^2\right] \tag{2.17e}$$

$$D^2 = C^2 + 3B^2 \ . \tag{2.17f}$$

For zero strain, the eigenvalues defined by Eqs. (2.17a) and (2.17b) reduce to the well known "warped" or "fluted" energy surfaces

$$E_{1,2}(k) = Ak^2 \pm \left[B^2k^4 + C^2\left(k_x^2k_y^2 + k_x^2k_z^2 + k_y^2k_z^2\right)\right]^{1/2} \qquad (2.18)$$

where (1) and (-) refer to the heavy hole band and (2) and (+) refer to the light hole band. Cyclotron resonance measurements give mass parameter values of A = -6.98 ± 0.02, B = 4.4 ± 0.2, C = 6.2 ± 1.0 (units of $\hbar^2/2m$).[23]

Expressions for the effective masses averaged over $\vec{k}$ directions are

$$\frac{m_1^*}{m} = \frac{1}{A-B'} \quad \text{and} \quad \frac{m_2^*}{m} = \frac{1}{A+B'} \qquad (2.19)$$

where $B' = [B^2 - C^2/6]^{1/2}$. The resulting values of $m_1^*/m = 0.52$ and $m_2^*/m = 0.08$ agree within 20% with a calculation of the density of states effective masses by Lawaetz.[24]

Under large [001] strain the tops of the valence bands decouple and the energy surfaces are given by

$$E_1(k) = \left(A + \frac{1}{2}B\right)k_\perp^2 + \left(A-B\right)k_\parallel^2 + \frac{\delta_s}{2} \qquad (2.20a)$$

$$E_2(k) = \left(A - \frac{1}{2}B\right)k_\perp^2 + \left(A+B\right)k_\parallel^2 - \frac{\delta_s}{2} \qquad (2.20b)$$

where $k_\perp^2 = k_x^2 + k_y^2$ and $k_\parallel^2 = k_z^2$.

These surfaces are ellipsoids of revolution, one oblate and the other prolate,[25] with their symmetry axes along [001]. The density of states effective masses in this case have the values

$$\frac{m_1^*}{m} = \left[\frac{1}{\left(A + \frac{1}{2}B\right)^2 (A-B)}\right]^{1/3} = 0.17 \qquad (2.21a)$$

and

$$\frac{m_2^*}{m} = \left[\frac{1}{\left(A - \frac{1}{2}B\right)^2 (A+B)}\right]^{1/3} = 0.16 \qquad (2.21b)$$

showing that under large deformation the maxima of the bands can not be distinguished as "heavy" and "light" but rather have nearly identical effective masses. The band structure and constant energy surfaces for GaAs in the presence and absence of strain are sketched in Fig. 2.1.

2.5. Model Wave Function for the Complete Hamiltonian

The valence band wave functions must in general be obtained by diagonalizing an 8×8 interaction matrix for the complete Hamiltonian

$$H = H_{k\cdot p} + D + H_{so} \,. \qquad (2.22)$$

No known author has displayed a general solution for arbitrary values of strain and linear momentum. It shall be assumed that near the band edge the wave functions have the form

$$\psi_M = \sum_\mu u_\mu \, C_{\mu M}(\vec{k}) \qquad (2.23)$$

where the u_μ are restricted to Bloch wave functions of J = 3/2 with $M_J = \mu$ ($\mu = \pm 1/2, \pm 3/2$). The Kane model solutions discussed in Sec. 2.3 for the limiting cases of $\delta_s >> E_k$ and $E_k >> \delta_s$ ($E_k = \hbar^2 k^2/2m^*$)

correspond to $C_{\mu m}(\vec{k}) = D^J_{\mu m}(\theta_s,\phi_s)$ and $D^J_{\mu m}(\theta_k,\phi_k)$, respectively, where (θ_s,ϕ_s) are the polar angles of the strain axis and (θ_k,ϕ_k) are the polar angles of $\vec{k}$ with respect to the z-axis defined by the optical pumping beam. When the strain and k·p interactions are comparable, i.e., where $E_k \simeq \delta_s$, it shall be assumed that the approximate wave functions are of the form:

$$\psi_M = a(\vec{k}) \sum_\mu u_\mu D^J_{\mu M}(\theta_s,\phi_s) + b(\vec{k}) \sum_\mu u_\mu D^J_{\mu M}(\theta_k,\phi_k) \qquad (2.24a)$$

$$\equiv a(\vec{k})\ \psi_{sM} + b(\vec{k})\ \psi_{kM} \quad . \qquad (2.24b)$$

This trial solution is a linear combination of the two wave functions which comprise the two limiting cases, which have known angular momentum properties. For a particular direction and magnitude of strain, the coefficients $a(\vec{k})$ and $b(\vec{k})$ are expected to depend on both the direction and magnitude of k. However, by analogy with perturbation theory, the admixture of ψ_{sm} and ψ_{km} is expected to be of the order E_k/δ_s. Therefore, as an educated guess, the approximately normalized amplitudes (ψ_{sm} and ψ_{km} as defined are not orthogonal), averaged over $\vec{k}$ directions, are taken to be

$$\bar{a} = \left[1 + (E_k/\delta_s)^2\right]^{-1/2} \qquad (2.25a)$$

$$\bar{b} = (E_k/\delta_s)\left[1 + (E_k/\delta_s)^2\right]^{-1/2} \quad . \qquad (2.25b)$$

Equations (2.24) and (2.25) represent an approximation to the valence band wave functions in uniaxially stressed GaAs. It is assumed that the conduction band wave functions are not significantly affected by stress and remain the spherically symmetric functions $S\uparrow$ and $S\downarrow$. In Chapter III these wave functions are applied to a calculation of the conduction electron spin polarization produced by band edge optical pumping. In Chapter V the results of the calculation are compared with the data to determine the quality of the theoretical estimate.

Chapter III

OPTICAL PUMPING AND POLARIZED PHOTOLUMINESCENCE

3.1. Density Matrix Description of Electron Spin Polarization

3.1.1. General formalism

A system of electrons which populate a set of spin states ψ_n can be characterized by a spin density operator f which is defined by[26]

$$f = \sum_n N_n \, |\psi_n\rangle \langle\psi_n| \tag{3.1}$$

where N_n is the number of electrons in state ψ_n.

Once a basis of spin states $|m\rangle$ ($m = \pm 1/2$) is chosen with respect to a particular spin quantization axis z, the representation of f in this basis forms the spin density matrix f whose matrix elements are

$$f_{mm'} = \sum_n N_n \langle m|\psi_n\rangle \langle\psi_n|m'\rangle \quad . \tag{3.2}$$

The average spin polarization of an electron in the system described by f is a vector $\vec{P}_s$ given by

$$\vec{P}_s = \frac{\mathrm{Tr}\ (f\vec{\sigma})}{\mathrm{Tr}\ (f)} \tag{3.3}$$

where $\vec{\sigma} = \hat{i}\sigma_x + \hat{j}\sigma_y + \hat{k}\sigma_z$ and σ_x, σ_y and σ_z are the Pauli spin matrices. The density matrix can conveniently be written as

$$f = \frac{N}{2}\begin{pmatrix} 1 + P_z & P_x - iP_y \\ P_x + iP_y & 1 - P_z \end{pmatrix} \tag{3.4}$$

where $N = \sum N_n$ is the total electron population. The matrix elements can also be written

$$f_{mm'} = \frac{N}{2}\left(\delta_{mm'} + \vec{\sigma}_{mm'} \cdot \vec{P}_s\right) . \tag{3.5}$$

3.1.2. Density matrix for interband optical absorption

The density matrix describing the spins of conduction electrons which are photoexcited from a state of momentum k in valence band V_n is given by

$$f^{(n)}_{mm'} = C \sum_{M_n} \langle m|d^q|kM_n\rangle \langle kM_n|d^q|m'\rangle \tag{3.6}$$

where C is a proportionality constant related to the intensity of the pump beam and d^q is the dipole moment operator for light of polarization q. The conventions for designating the optical polarization are described in Fig 3.1. The summation in Eq (3.6) is over the magnetic sublevels of the valence band V_n. These levels are assumed to be degenerate for the purposes of this discussion. The heavy-hole valence band is conventionally designated as V_1 ($M_1 = \pm 3/2$) and the light-hole band as V_2 ($M_2 = \pm 1/2$).

In Chapter II it was shown that the wave functions representing the band edge valence state $|kM\rangle$ are given by Eq. (2.8) in which (θ,ϕ) are

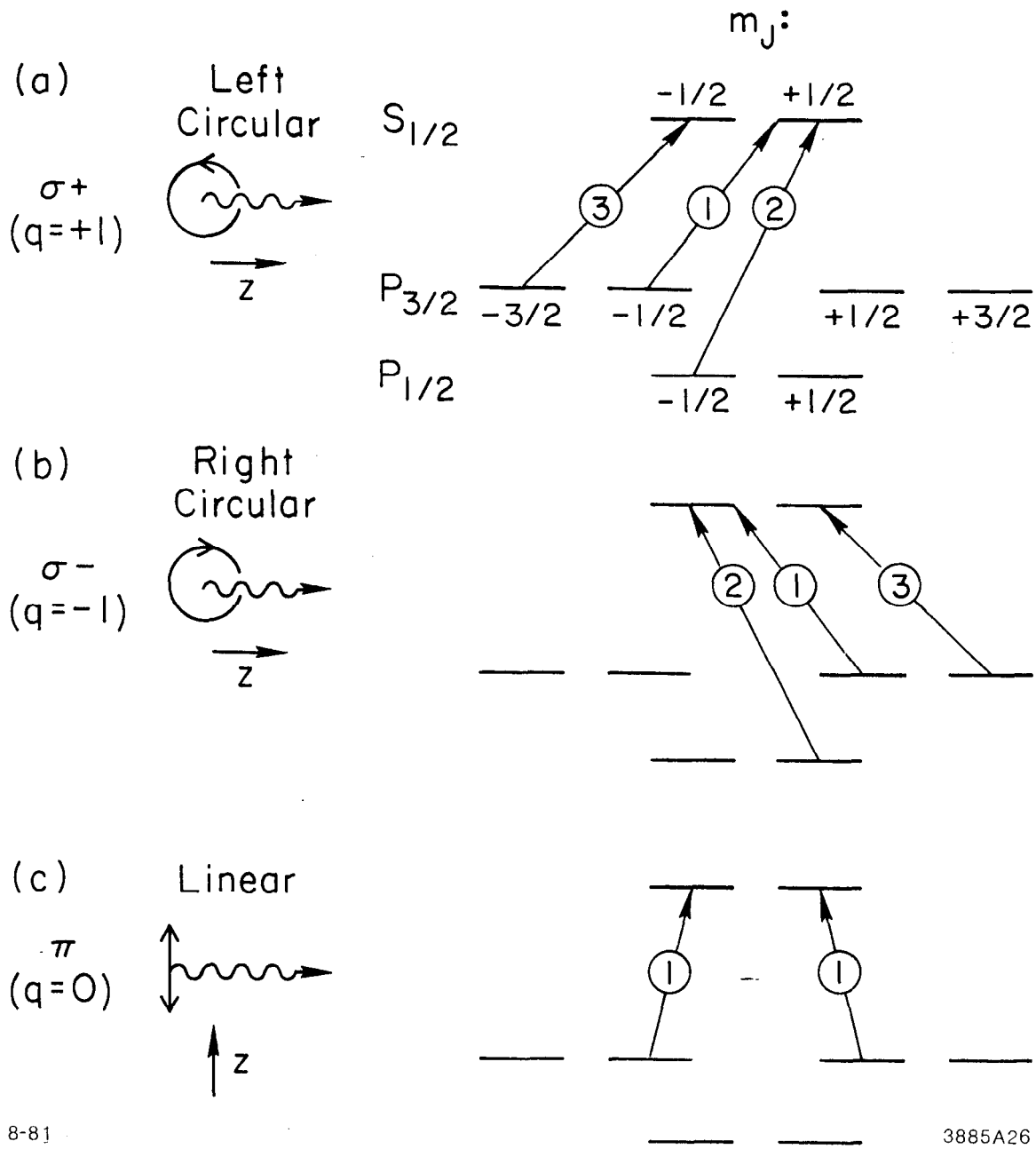

Fig. 3.1. Conventions for designating optical polarization.

the polar angles of the momentum vector $\vec{k}$ (zero stress case) or the strain axis (infinite stress case). Substitution of Eq. (2.12) in Eq. (3.6) gives an expression for the density matrix in terms of the rotation matrix $D^{3/2}$ and the Wigner 3J symbols:

$$f^{(n)}_{mm'} = \sum_M D^{3/2}_{m-q,M} D^{3/2}_{m'-q,M} (-1)^{1-m-m'} \begin{pmatrix} 1/2 & 1 & 3/2 \\ -m & q & m-q \end{pmatrix} \begin{pmatrix} 1/2 & 1 & 3/2 \\ -m' & q & m-q \end{pmatrix} \tag{3.7}$$

where $q = \pm 1$ for σ^+ and σ^- polarized incident light. Choosing $q = +1$ for definiteness, the spin density matrix for conduction electrons excited from the heavy-hole valence band is given by

$$f^{(1)} = \frac{1}{12} \begin{pmatrix} \frac{3}{4}\sin^2\theta & -\frac{3}{8}\sin 2\theta e^{i\phi} \\ \frac{3}{8}\sin 2\theta e^{i\phi} & \frac{3}{4} + \frac{9}{4}\cos^2\theta \end{pmatrix} . \tag{3.8a}$$

For light-hole band excitation the density matrix becomes

$$f^{(2)} = \frac{1}{12} \begin{pmatrix} 1 - \frac{3}{4}\sin^2\theta & \frac{3}{4}\sin 2\theta e^{i\phi} \\ \frac{3}{4}\sin 2\theta e^{i\phi} & \frac{9}{4}\sin^2\theta \end{pmatrix} . \tag{3.8b}$$

The component of the electron spin polarizaiton vector that is parallel to the optical pumping beam is given by

$$P_{sz}^{(n)} \equiv P_{sn} = \frac{\mathrm{Tr}\left(f^{(n)}\sigma_z\right)}{\mathrm{Tr}\left(f^{(n)}\right)} . \qquad (3.9)$$

Substitution of Eqs (3.8a) and (3.8b) in Eq (3.9) gives

$$P_{s1} = -\frac{2\cos^2\theta}{1+\cos^2\theta} \qquad (3.10a)$$

and

$$P_{s2} = \frac{2-6\sin^2\theta}{2+3\sin^2\theta} . \qquad (3.10b)$$

The angle θ is the polar angle between the quantization axis of the valence band state and the propagation direction of the absorbed optical beam. The expressions in Eq. (3.10) are graphically presented in Fig. 3.2.

In the optical pumping process, electrons with a variety of k-vectors contribute to the conduction electron spin polarization. Assuming conservation of momentum, the k-vector of an electron immediately after excitation is the same as that of its initial state since the momentum of the absorbed near infrared photon is negligible compared to the minimum thermal electron momentum. The total density matrix is the integral over all values of f(k) consistent with the absorbed photon energy:

$$F_{mm'} = \int \frac{d^3k}{(2\pi)^3} \sum_n \delta\left[E_c(k) + E_{V_n}(k) + E_{g_n} - h\nu\right] f_{mm'}^{(n)}(k) . \qquad (3.11)$$

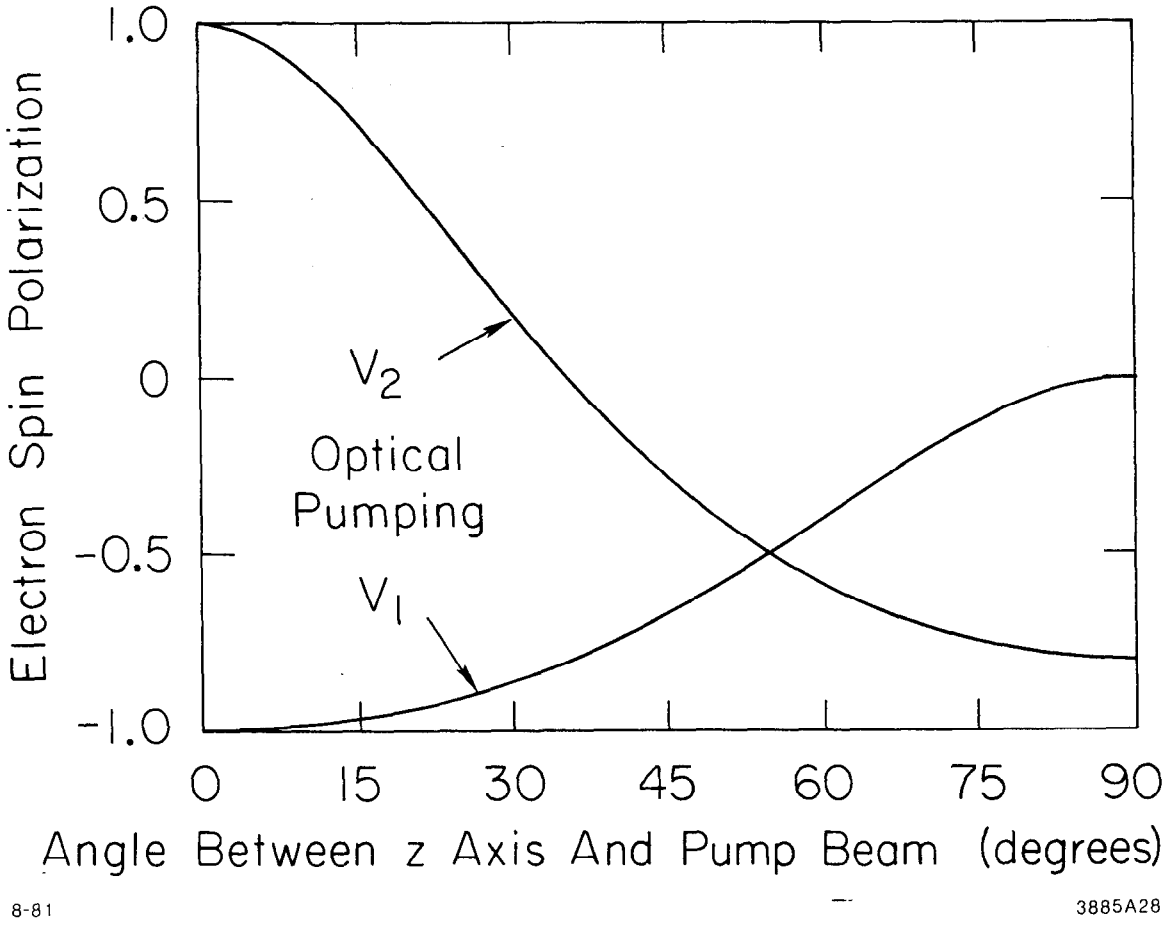

Fig. 3.2. Dependence of spin polarization on angle between the spin quantization axis of the initial state wave functions and the pump beam direction.

Let $K = Tr(F) = \sum K_n$ and $R = Tr(F\sigma) = \sum R_n$ where

$$K_n = \int \frac{d^3k}{(2\pi)^3} \delta[E_c(k) + E_{V_n}(k) + E_{g_n} - h\nu] \; Tr(f^{(n)}) \tag{3.12a}$$

and

$$R_n = \int \frac{d^3k}{(2\pi)^3} \delta[E_c(k) + E_{V_n}(k) + E_{g_n} - h\nu] \; Tr(f^{(n)}\sigma_z) \tag{3.12b}$$

where $E_c(k)$ and $E_{V_n}(k)$ are kinetic energies measured from the band edges labeled by their subscripts. The spin polarization per electron excited from V_n therefore is

$$P_{sn} = \frac{R_n}{K_n} . \tag{3.13}$$

The average spin polarization of the total system of conduction electrons P_s is given by

$$P_s = \frac{\sum_n R_n}{\sum_n K_n} = \frac{N_1 P_{s1} + N_2 P_{s2}}{N_1 + N_2} - \cdots \tag{3.14}$$

where N_n is the number of electrons excited from V_n The values of N_n are proportional to the absorption coefficients $\alpha_n(h\nu)$ for each valence band. The spin polarization values P_{sn} have a dependence on $h\nu$ because of the energy variation of the valence band wave functions which are given by Eqs. (2.24) and (2.25).

3.2. Spin Polarization for Optical Pumping Near the Band Gap

In the limiting cases of zero or infinite stress, the quantities $Tr(f_\sigma)$ and $Tr(f)$ are given by the numerator and denominator of Eq. (3.10a) for V_1 excitation and Eq. (3.10b) for V_2 excitation. At zero stress, θ is the polar angle of k. If the warping of the constant energy surfaces away from spherical shapes is neglected, the integrals in Eq. (3.12) are separable into radial and angular parts. The spin polarization functions P_{sn} defined by Eq. (3.13) are

$$P_{s1} = \frac{\int d\Omega_k \left(-2\cos^2\theta_k\right)}{\int d\Omega_k \left(1 + \cos^2\theta_k\right)} = -0.5 \qquad (3.15a)$$

and

$$P_{s2} = \frac{\int d\Omega_k \left(2 - 6\sin^2\theta_k\right)}{\int d\Omega_k \left(2 + 3\sin^2\theta_k\right)} = -0.5 \quad . \qquad (3.15b)$$

The significance of the minus sign is that the spins are oriented opposite to the angular momentum of the photons in the incident beam (the remaining angular momentum is delivered to the holes).

Equation (3.15) combined with Eq. (3.14) show that $|P_{sn}| \simeq 0.5$ or 50% in an unstressed crystal independent of the exact proportion of electrons excited from each valence band.

In the limit of infinite stress, the angle θ in Eq. (3.10) is fixed by the geometry of the stress axis and the optical pumping beam and thus

the averaging over k-vector directions in Eq. (3.12) does not affect the polarization for either band. The experimental situation which approximates this case is one in which a uniaixial stress lifts one band above the other in energy and excitation occurs from the edge of the higher band so that $N_1 >> N_2$ or vice versa. Under a compressive stress, a theoretical maximum spin polarization of -0.8 occurs for $N_2 >> N_1$ with $\theta = 90^o$. In principle, uniaxial tension and band edge excitation causing $N_1 >> N_2$ will result in a theoretical maximum of 1.0 for $\theta = 0^o$. As a practical matter, the choice of compressive stress and the 90^o geometry is dictated by the much higher strength of brittle gallium arsenide under compression compared to tension and the adaptability of the geometry to a photoemission electron source in which the surface must be exposed to ultrahigh vacuum.

To approximate the regime between the two limiting cases discussed above, the approximate wave function defined by Eq. (2.24) is substituted in the spin density matrix of Eq. (3.6), which becomes

$$f^{(n)}_{mm'}(k) = \{|a|^2 f^{(n)}_{mm'}(\theta_s,\phi_s) + |b|^2 f^{(n)}_{mm'}(\theta_k,\phi_k) + \sum_M [ab^* \langle m|d|\psi_{sM}\rangle \langle \psi_{kM}|d|m'\rangle + \bar{c}.c.]\} . \qquad (3.16)$$

The total density matrix is obained by insertion of Eq (3.16) in Eq. (3.11). In Eq. (3.16), the first and second terms have density matrix elements previously calculated for the zero and infinite stress limits. The third and fourth terms contain factors which might be expected to exhibit large phase and amplitude changes as the direction of k is varied in the integrals of Eq. (3.12) since the linear

combination of $|JM_J\rangle$ states which makes up the exact solution will vary with the direction of k. The assumption will be made that the the third and fourth terms of Eq. (3.16) can be dropped without serious error. It is noted that this assumption is suggested here for the first time to obtain an approximate expression for the stress dependence of the optical pumping spin polarization and has not been proposed or tested in any previous work.

Substituting the first terms of Eq. (3.16) in Eq. (3.11), using the values of the a and b factors given by Eq. (2.25), and making the simplifying assumption of spherical energy surfaces, the conduction electron spin polarization as a function of the ratio of energy eigenvalues for V_2 optical pumping becomes

$$P_{s2} = \frac{2 - 6\sin^2\theta_s - 2(E_k/\delta_s)^2}{2 + 3\sin^2\theta_s + 4(E_k/\delta_s)^2} \qquad (3.17a)$$

and for V_1 optical pumping is given by

$$P_{s1} = \frac{(-2\cos^2\theta_s) - 2(E_k/\delta_s)^2}{(1 + \cos^2\theta_s) + 4(E_k/\delta_s)^2} \quad . \qquad (3.17b)$$

These functions are plotted in Fig 3.3 for the case of $\theta = 90^o$ and in Fig. 3.4 for $\theta = 0^o$.

3.3. Luminescence Polarization

According to the correspondence princple, recombination luminescence can be regarded as the radiation of a dipole moment equal to the matrix element of the corresponding interband transition. The components of the E-field of the recombination radiation can therefore be

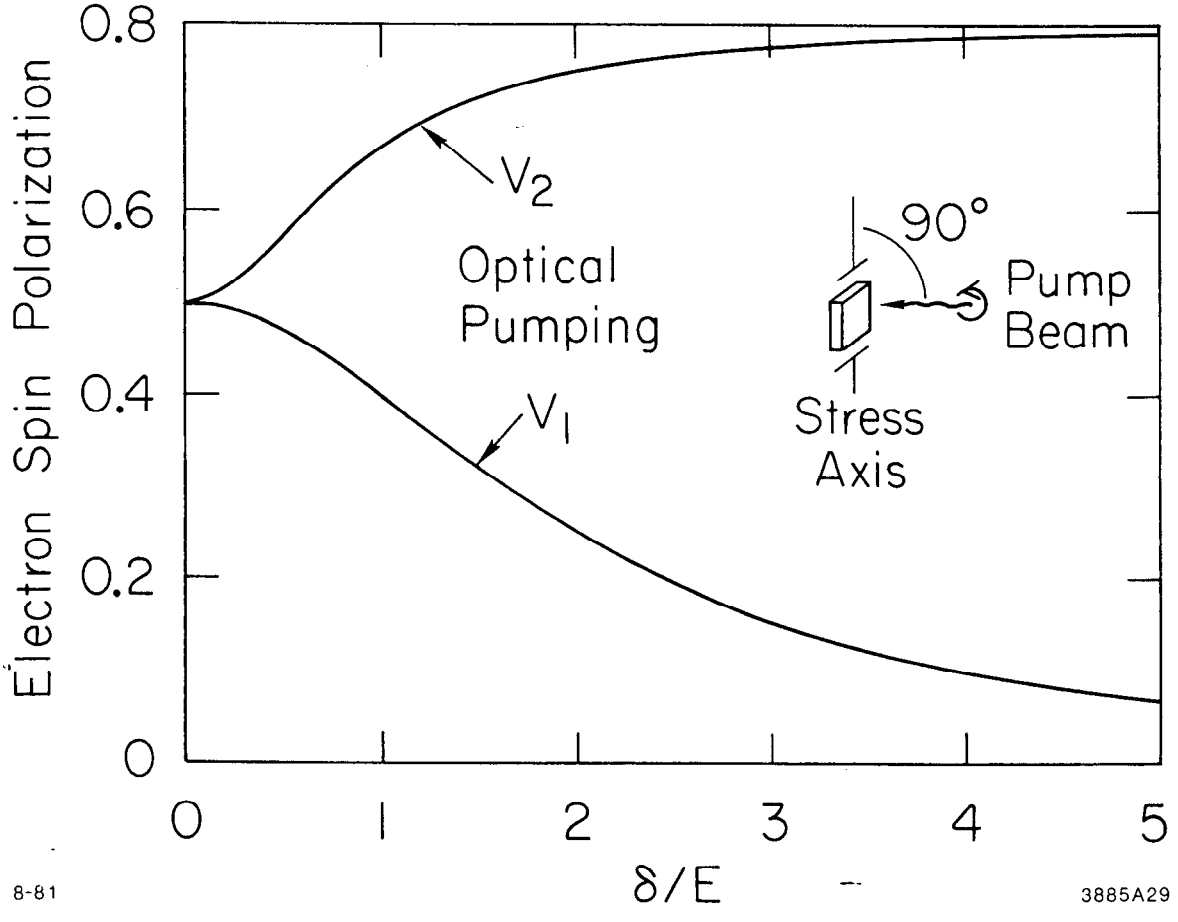

Fig. 3.3. Dependence of spin polarization on the parameter ratio δ/E for optical pumping of light-hole (V2) and heavy-hole (V1) valence bands at 90° to the stress axis.

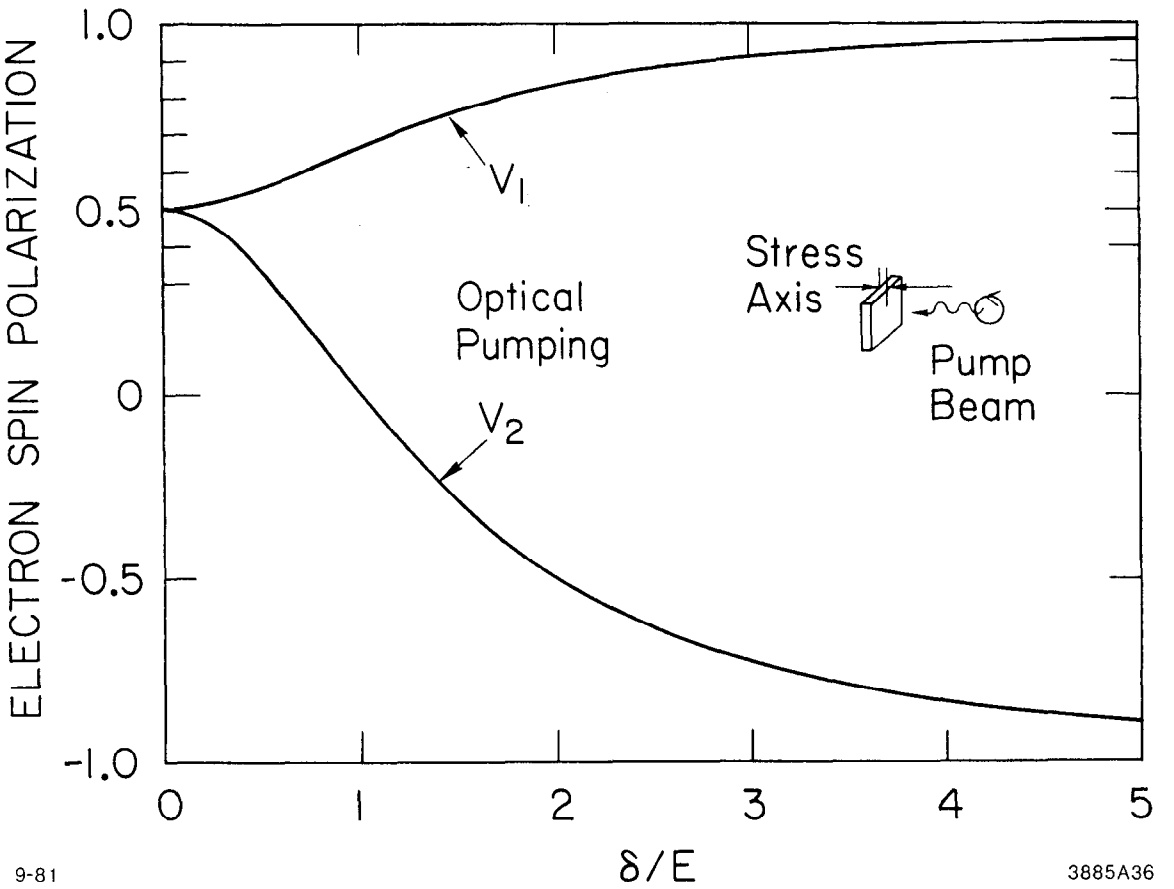

Fig. 3.4. Dependence of spin polarization on δ/E for optical pumping parallel to the stress axis.

calculated from the density matrix for the combined system of electrons and holes. For the case of weak excitation of a p-type crystal, the holes are assumed to be completely unoriented and the electron-hole density matrix reduces to that of the electron system alone.[7] Thus

$$\left(d^{q}\right)^{2} = \sum_{mm'} F_{mm'}\, d^{q}_{m\mu}\, d^{q}_{m'\mu} \tag{3.18}$$

where $F_{mm'}$ is given by Eq. (3.11) in which $h\nu$ now refers to the luminescence photons. $m(m')$ labels the state of the electrons and $\mu(\mu')$ the state of the holes which recombine to emit the luminescence. In terms of the luminescence polarization components $(d^{+1})^2$ and $(d^{-1})^2$ the luminescence circular polarization P_σ is given by

$$P_\sigma = \frac{\left(d^{+1}\right)^2 - \left(d^{-1}\right)^2}{\left(d^{+1}\right)^2 + \left(d^{-1}\right)^2} . \tag{3.19}$$

An exact relation between P_σ and P_s can be given without explicit calculation of the components of F, since P_s and F obey the general relation defined by Eq. (3.5). The partially relaxed spin polarization P_s' at the average time of recombination is related to the polarization at the instant of excitation by

$$P_s' = P_s \frac{\tau_s}{\tau_s + \tau_r} \tag{3.20}$$

where τ_s and τ_r are the spin relaxation and radiative lifetimes, respectively. Substituting Eqs. (3.5) and (3.18) in Eq. (3.19), and making the correction indicated by Eq. (3.20), the relation between luminescence circular polarization and spin polarization is given by

$$P_\sigma = P_h P_s \frac{\tau_s}{\tau_s + \tau_r} \cos\theta \ . \qquad (3.21)$$

P_h is the hole coupling factor, which is identical to the spin polarization at a value of $h\nu_{laser} = h\nu_{lum}$. θ is the angle between the optical pumping beam and the direction of observation of the luminescence.

Chapter IV

EXPERIMENTAL EQUIPMENT

4.1. System Overview

The experimental apparatus was built for the study of polarized photoluminescence in an optically pumped GaAs sample cooled with liquid nitrogen and subjected to a large uniaxial strain. The excitation light can be provided either by a pulsed, tunable infrared dye laser or by a cw helium-neon laser. The polarization of the laser light can be either linear or circular; the luminescence light can be resolved into linear or circular polarization components and recorded as a function of wavelength. Polarized photoluminescence spectra recorded under various conditions of excitation light and sample strain provides information on the shape, shift, and splitting of the absorption edge, as well as on the conduction electron spin polarization.

The components of the experimental setup are grouped into three subsystems: the GaAs sample and low temperature stress apparatus, the tunable dye laser and optical system, and the signal processing electronics. The design and performance of each subsystem will be discussed in turn.

4.2. GaAs Sample Preparation

Wafers of GaAs 2.0 mm thick and cut perpendicular to the [001] crystal axis were used.[27] p-doping with a quoted Zn impurity concen-

tration of $N_a = 1 \times 10^{18}$ cm^{-3} was used in these experiments. This value of the doping density is roughly the minimum amount required for degenerate doping with shallow acceptors and is a compromise between requirements for actual NEA cathode operation and band-tailing effects. Heavy doping is required to give a low resistivity in a cathode to support high currents and provide a narrow band-bending region near the surface.[4] On the other hand, the width of the band-tail on the density of states increases $\propto N_a^{1/2}$ (see Sec. 5.5) and is expected to limit the stress-induced increase in the optically pumped electron spin polarization.

To detect photoluminescence in the presence of scattered laser light that is tuned close to the band gap, it was necessary to use samples with highly polished, specular faces in order to reduce the scattered intensity. A chemical polishing-etch was used to prepare the surface of the entire wafer prior to dicing. The wafer was held by Nalgene tweezers, dipped in a 4:1:1 solution of H_2SO_4:H_2O:H_2O_2 at 50^oC, agitated for three minutes, then thoroughly rinsed in distilled water.[28] This method produced highly specular surfaces. Some "orange peel" ripple and etch pits were usually found because of the difficulty in getting sufficiently turbulent flow over the surface of the wafer while etching. However, the peroxide-acid etch described above produced a polish superior to that obtained either by mechanical polishing with diamond paste or by chemical-mechanical polishing with a weak solution of bromine in methanol. The etching process reduced the wafer thickness to approximately 1.65 mm.

The wafers were then sawed into rectangular chips approximately 3.5 mm by 6.5 mm with sides parallel to {001} planes. Since the {011} planes are the dominant cleavage planes in GaAs, azimuthal orientation was performed by making a test cleave in one corner of the wafer. The <001> directions were taken to be at $\pm 45^{\circ}$ to the cleaved edge.

The corners of the rectangular sample chips were required to be accurate 90° angles to prevent crushing the sample by unbalanced shear forces when stress is applied. These were produced by the motion of two transversely mounted, coupled translation stages on the table of a diamond wire saw.[29] Figure 4.1a shows the setup for sawing the wafers.

The wafer was advanced against the 0.2 mm wire by the pull of a weight hung over the side of the table. After each cut, the wafer was pushed back of the wire and stepped transverse to the cut by a lead screw. After one set of parallel cuts was made, the wafer was rotated by 90° for a transverse set of cuts.

The faces and corners ofthe samples were protected from scratching and chipping during the sawing operation by sandwiching the wafer between two 3.5 mm thick graphite slabs with a jeweler's wax. The sandwich was then bonded to a supporting slab of graphite with tooling wax, and this slab was clamped to the top translation stage. The saw was set up to cut completely across the wafer, but not through the wider supporting layers of graphite; the severed GaAs chips were thus held in place during the entire sawing operation. The melting temperatures were 60°C for the tooling wax and 90°C for the jeweler's wax, so that after one set of parallel cuts had been made, the sandwich could be warmed to 60°C, removed intact from the supporting slab, rotated by 90°, and

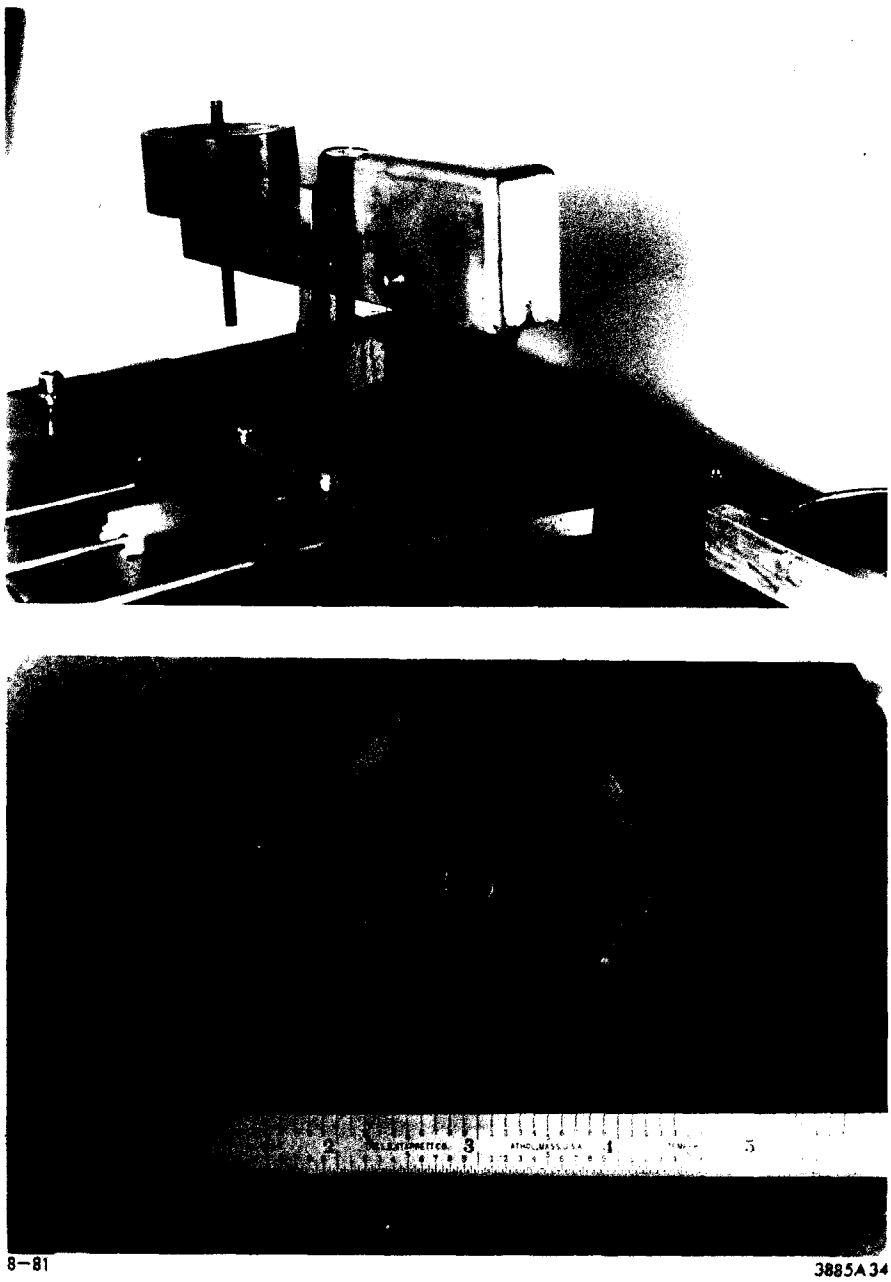

Fig. 4.1. Photographs of the diamond wire saw and translation stage (a) and the polishing disc (b) used for preparation of GaAs samples.

rebonded. Accurate 90^{o} rotation was achieved simply by using the edges of the graphite squares for alignment.

Inducing a large uniaxial strain without shattering the sample required that the opposing compressive forces be applied evenly on smooth, flat, parallel edges. After dicing, the rough-edged chips were stacked face-to-face in a circular polishing disc with three radial slots and waxed in place. The edges against which the stress would be applied were exposed above each side of the disc. Figure 4.1b shows the loaded polishing disc. The edges were ground flush to the disc surface using a water suspension of platelet alumina[30] on a glass plate with a particle size sequence of 30, 12, and 3 microns. Finer grinding or polishing was found to be unnecessary.

The dimensions of a completely prepared sample chip was typically $5.7 \times 3.5 \times 1.65$ mm. Pressure was applied to the smallest opposing edges. The dimensions of each sample were recorded prior to use to obtain an accurate stress calibration.

4.3. Uniaxial Stress Apparatus

The stress apparatus was designed to meet the following requirements: 1) accurately monitored and controlled uniaxial pressure up to at least 3×10^{9} dyn cm^{-2} (3 kbar); 2) sample cooling with liquid nitrogen or liquid helium; 3) optical access for the laser and luminescence beams; and 4) an easily detachable sample and anvil structure that could be bench-assembled prior to installation in the system.

A pneumatic stress device was machined as a cold finger attachment to a Hoffman cryostat that can use liquid nitrogen or liquid helium as a coolant.

Figure 4.2 shows a drawing of the apparatus and Fig. 4.3 is a photo of the assembly. The apparatus consists of three sections which are mated by 1.27 mm pitch machine threads. A cold plate was permanently attached to the base of the cryostat's inner chamber. The assembly containing the anvil, sample, and piston was threaded into the cold plate and secured with a lock nut. The bellows assembly was fitted directly below. The central section contained a small bellows which was used as a spring to seat the sample, anvils, and piston together.

The parts were machined from OFHC copper and were silver plated to reduce radiation heating and improve thermal contact. The anvils were made from 1.59 mm tool stock, precision ground to parallelism and 90^{o} angles. Strips of annealed gold foil were placed between the anvils and the sample to smoothly distribute the force over surface irregularities to achieve uniform pressure. Anvil squirm transverse to the direction of force was controlled by ball plungers.[31] These were tightened against the front of the anvils without twisting them out of alignment. The sample was held against the cold finger with beryllium copper tabs.

The stainless steel bellows[32] was sealed by TIG-welded stainless end plates. The bellows was purged of air and pressurized with helium gas by two 1.65 mm o.d. stainless capillaries welded into the bottom end plate. These were passed through the vacuum wall beneath the cold finger via bulkhead fittings. The tubes were coiled to reduce thermal conductance and to prevent strain on the welds. The bellows had an

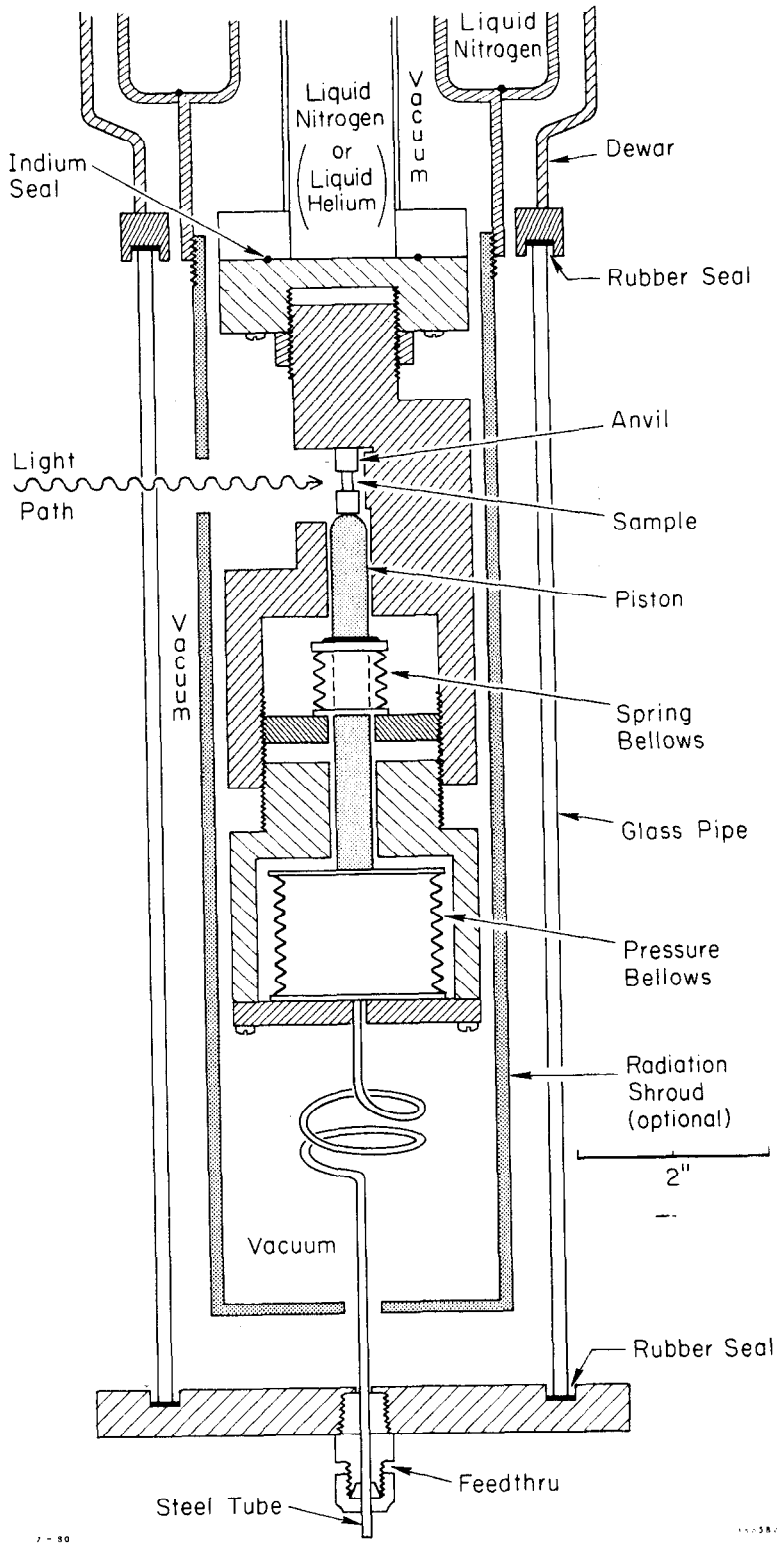

Fig. 4.2. Drawing of the low temperature stress apparatus.

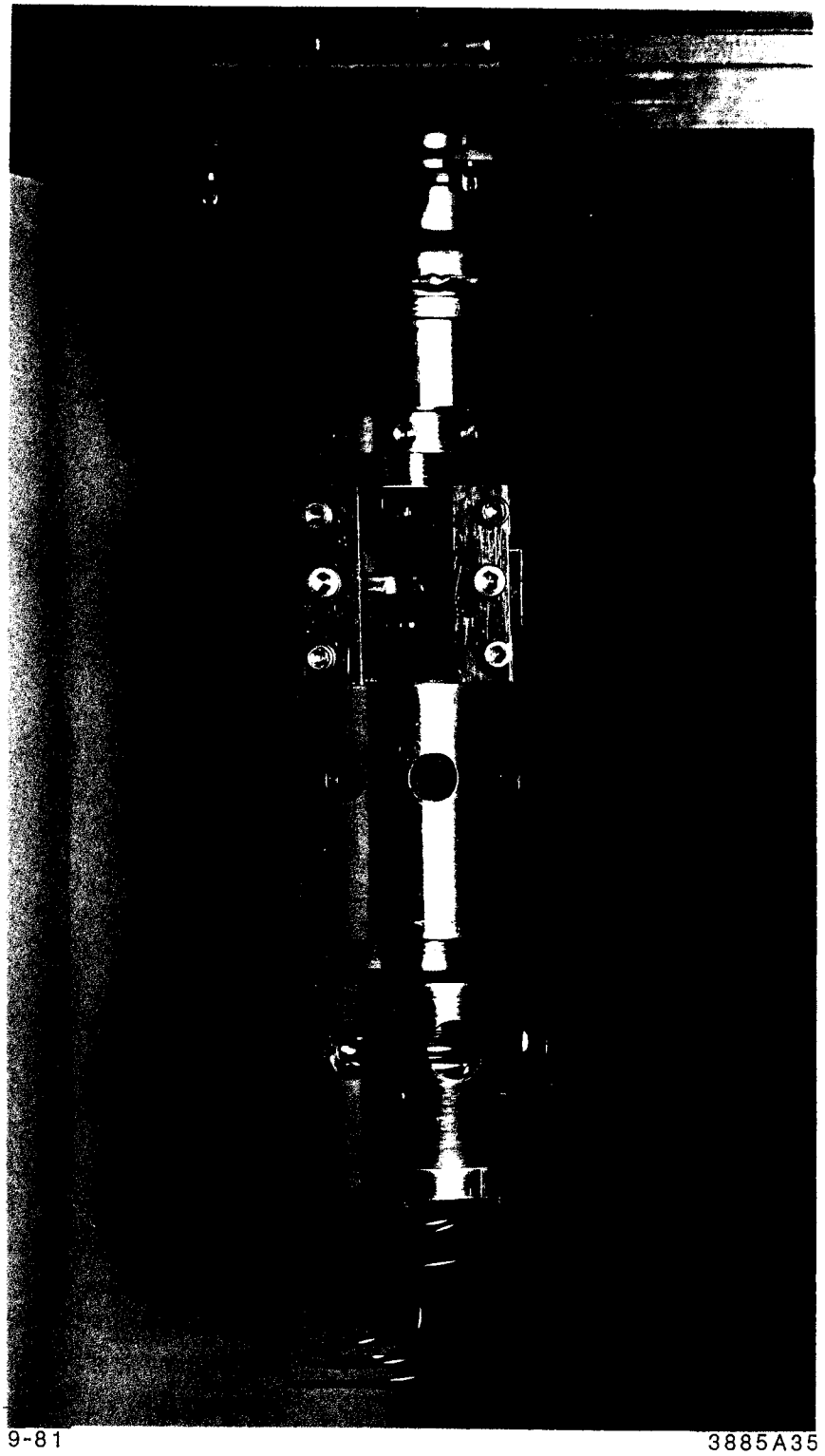

Fig. 4.3. Photograph of stress apparatus.

effective area of 15.0 cm^2 and a rated maximum working pressure of 21.5 bar. The relation between the sample stress χ inside the evacuated system and the bellows gauge pressure P_b measured on the external fill line was given by

$$\chi = \frac{A}{a}(1 + P_b) \qquad (4.1)$$

where A/a is the ratio of the bellows effective area to the sample edge area. For a typical sample edge area of 6.4 mm^2, the system gave a pressure amplification factor of 233x. With careful assembly, sample pressures in excess of 4 kbar (4×10^9 dyn cm^{-2}) were reached. The typical sample breaking pressure in this system corresponded to about 1/3% strain. The intrinsic breaking strain of GaAs is about 1.2%.[33] The breakage mechanism of samples in the system was probably due to anvil squirm under high load.

The temperature of the cold finger was measured using either a forward biased diode or a carbon resistor as a thermometer. The temperature of the gallium arsenide sample was estimated within $\pm 10^{\circ}C$ from the peak position of the luminescence band using the Varshni equation.[57] Presumably because of the limitations of the thermal contacts within the system, liquid nitrogen cooled the cold finger to $\simeq 90^{\circ}C$ and the sample to $\simeq 100^{\circ}C$. Liquid helium brought the cold finger to $20^{\circ}C$ but the sample temperature only dropped to $80^{\circ}C$. Adequate measurements were possible with liquid nitrogen and all data reported pertain to a sample temperature of $\simeq 100^{\circ}C$.

4.4. Tunable Infrared Dye Laser

A light source tunable from 8000Å to 8500Å was required for band edge optical pumping of GaAs p-doped in 10^{18} cm^{-3} range at 100°K. A design goal of a bandwidth at least ten times narrower than the maximum valence band splitting was set. Tests showed that uniaxial stress of 3 to 4 kbar would be feasible, resulting in a splitting of 15 to 20 meV. By the criterion stated above, this required a bandwidth of 10Å or less at a wavelength of 8000Å. An additional requirement was established from early helium-neon laser excited photoluminescence measurements. Using a slit resolution of 20Å, the scattered intensity at 6328Å was $\simeq 10^3$ brighter than the peak of the luminescence band. The background intensity of the light source was therefore required to be $\simeq 10^{-5}$ below the peak intensity to allow a luminescence polarization measurement accuracy of 1%.

These requirements could most easily be satisfied by a tunable dye laser. Since the ultimate goal of the experiment is the development of a pulsed photocathode compatible with SLAC operating requirements,[34,35] a pulsed dye laser was constructed. A flashlamp dye laser[36] was available from the SLAC PEGGY II polarized electron source. However, since flashlamp excitation of dyes which lase at wavelengths longer than 7500Å leads to rapid photodecomposition,[37] a secondary laser was constructed to be optically pumped by the flashlamp laser output by focusing its beam at the edge of the cuvette with a cylindrical lens.

Figure 4.4 shows the ir laser resonator. It is a simplified version of the well-known "Hansch-type" dye laser.[38] Because the pump laser had a relatively low peak power (< 10 kW), a long pulse length (> 1 μsec), and the bandwidth requirement was modest, a single 30 cm

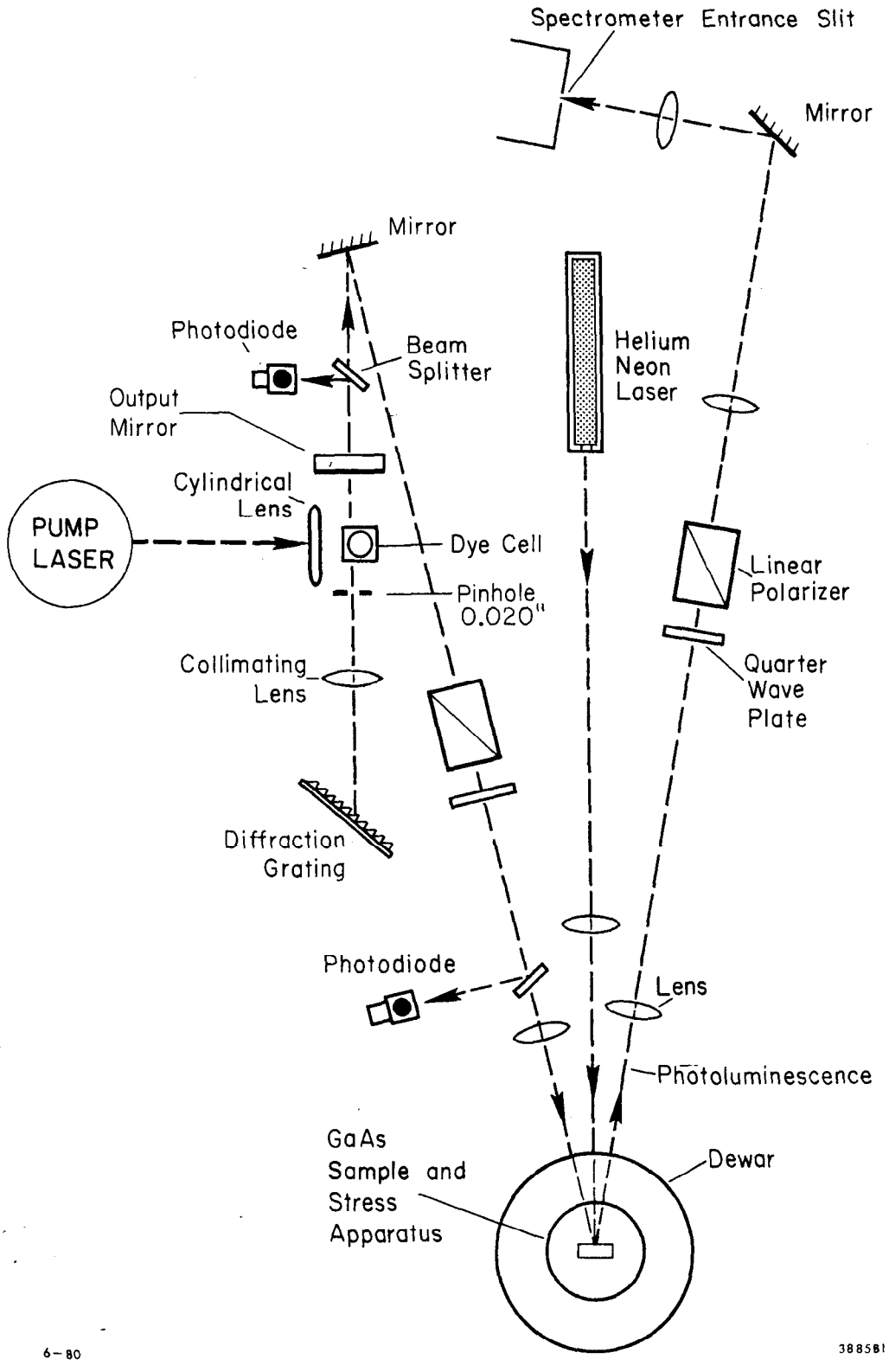

Fig. 4.4. Near infrared dye laser resonator and optical system.

focal length lens was used to expand and collimate the internal beam. The system is similar to one described by Passner and Venkatesan[39] with the addition of a 50% reflecting output mirror and a dye flow loop. Tuning was accomplished by dispersive feedback from a 1200 groove/mm gold coated diffraction grating, the center wavelength being given by the autocollimation relation $\lambda = 2d\sin\theta$, where d is the groove spacing and θ is the autocollimation angle.

The dye cell was a quartz spectrophotometer cuvette[40] with the bottom ground off. All infrared dyes are soluble in dimethyl sulfoxide (DMSO); therefore the components of the flow system were DMSO compatible materials such as teflon, silicone rubber, polyethelyne, and 304 or 316 stainless steel with passivated welds. A gear pump[41] and a 1 micron filter[42] were in the flow loop.

The ir dye was either DOTC or HITC, both at 2×10^{-4} M concentrations in DMSO. Tuning curves are shown in Fig. 4.5. The flashlamp laser was operated most often with a 7×10^{-5} M solution of oxazine 720 in methanol (710 nm, untuned). Sulfarhodamine in a 1:1 solvent mixture of methanol and water (664 nm) produced similar pumping performance.[43]

For a 9 mJ, 1.5 μsec pump pulse, the peak output was 12 μJ for DOTC and 7 μJ for HITC in a 250-500 nsec pulse. Figure 4.6a gives an oscilloscope trace of the pulse shapes. The ir pulse was significantly shorter than the pumping pulse. Self termination of the ir pulse was probably due to perturbations of the optical path through the dye caused by shock and thermal gradients.[39]

Spatial and spectral properties of the output beam were characterized by a divergence of 20 mrad and a bandwidth of 7Å fwhm. A 0.5 mm

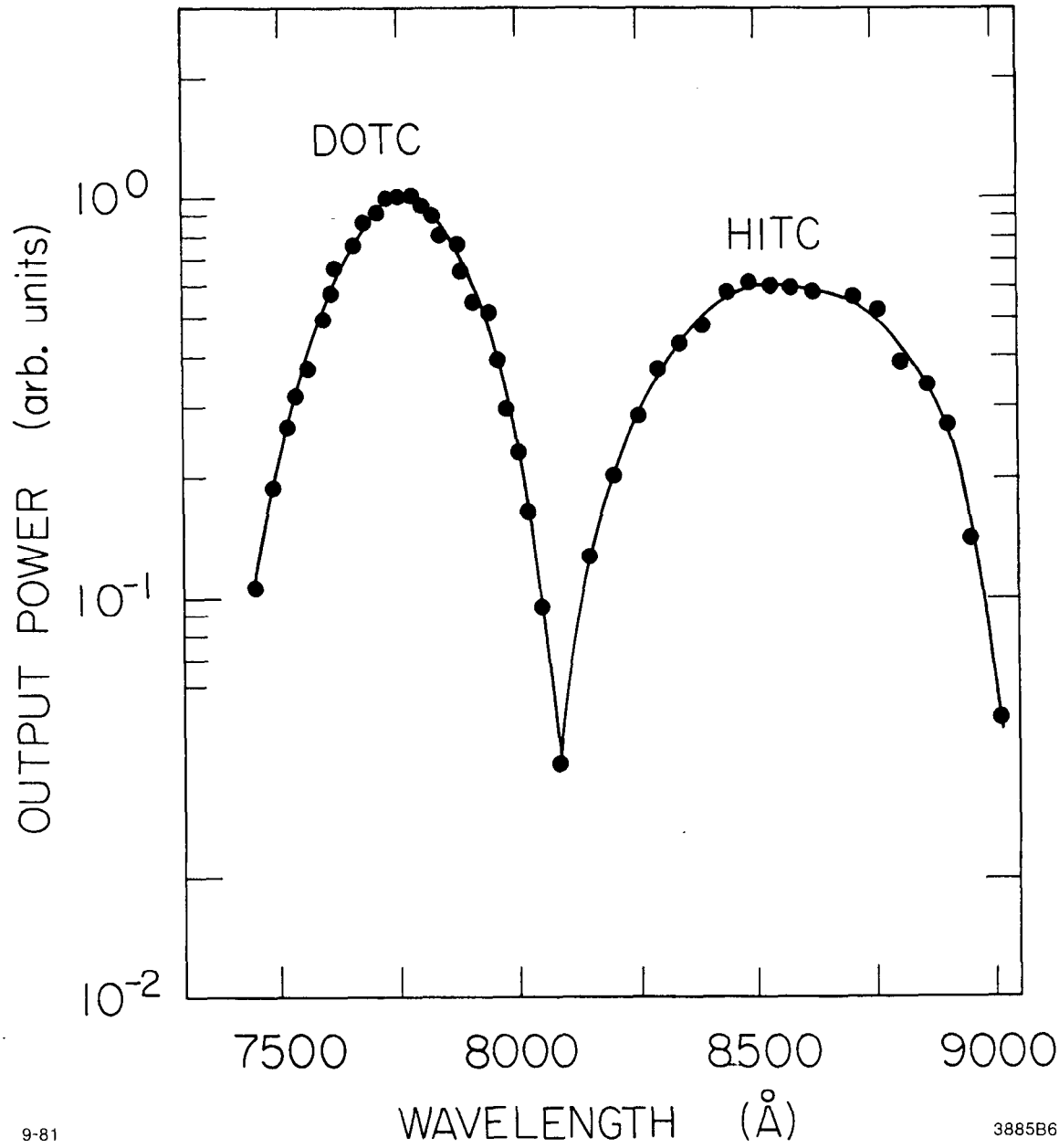

Fig. 4.5. Dye laser tuning curves for optical pumping at 705nm.

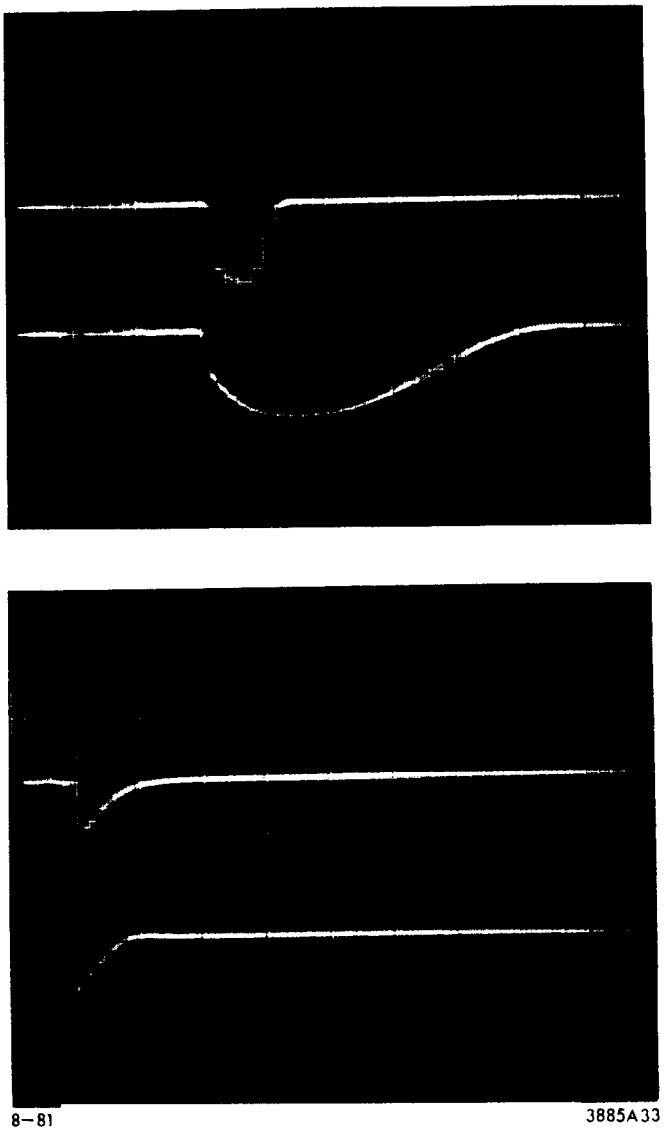

Fig. 4.6. Oscilloscope traces of flashlamp and i.r. dye laser pulses at 0.5 μsec/div (a), and gated integrator input and output signals at 2.0 μsec/div.

aperture was used next to the dye cell on the interior side of the cavity to suppress a long wavelength tail on the output spectrum. To reduce the background superfluorescence in the output beam and eliminate parasitic lasing between the cell walls, the dye cell was tilted at an angle of 5^{o} with respect to the pumping stripe. Alignment was performed by tight focusing into DOTC, which emitted visible superfluorescence. The procedure was greatly aided by the use of a hand-held infrared viewer.

After careful alignment and with fresh dye solutions in both lasers, the stability of the ir pulse was better than 20%. This figure was strongly dependent on the triggering rate of the system because of the slow flow rate at the interior wall of the ir laser cuvette. At 3 liter/min flow, the repition rate was kept below 20 pps to obtain the quoted stability.

4.5. Optical System

A schematic of the optical setup is shown in Fig. 4.4. The tunable dye laser was used for optical pumping of the gallium arsenide sample near the band gap. The helium-neon laser was used when accurate spectral lineshapes were required. The incidence angle of the dye laser beam on the sample was 20^{o} from the surface normal; the luminescence light was collected in an f/8.5 cone centered on the surface normal. A ray tracing of the luminescence beam through the imaging optics is shown in Fig. 4.7. The telescope had a magnification of $\simeq$1.3x and provided f-number matching to the f/10 spectrometer. The illuminated spot on the sample was approximately 0.25 mm fwhm. An entrance slit width of 0.5 mm was possible without occulting the image of the laser spot on the sample face. The

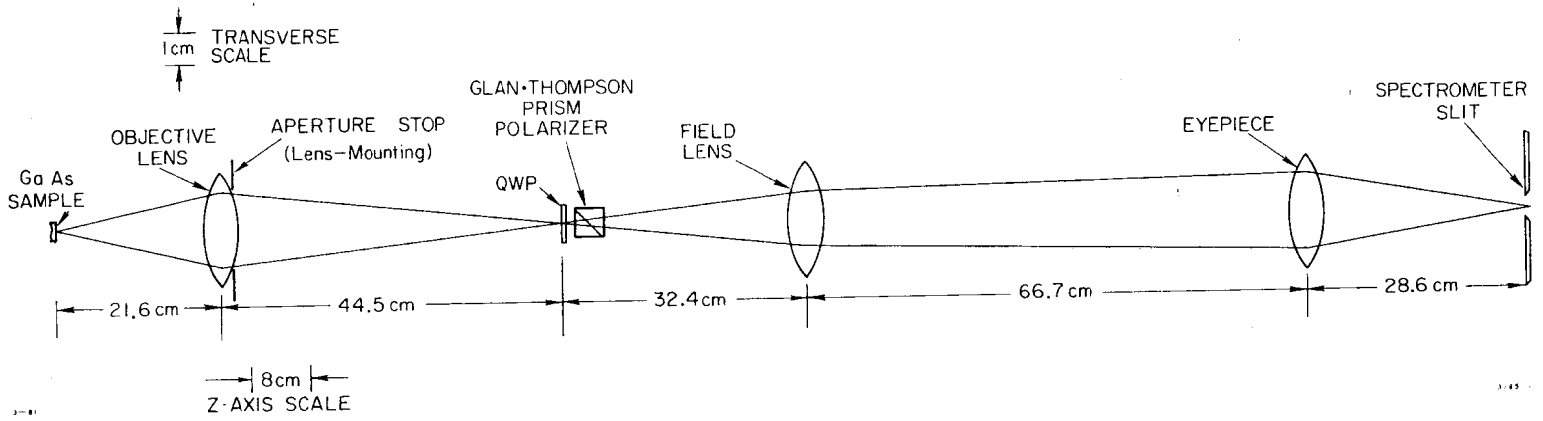

Fig. 4.7. Ray tracing of luminescence beam through the imaging telescope.

spectrometer was a one meter McPherson with a 300 groove/mm grating blazed at 7000Å. The dispersion at the exit slit was 33Å/mm.

Production and analysis of circularly polarized light was performed with standard combinations of retardation plates and linear polarizers in the laser and luminescence arms. The normal procedure for measuring luminescence polarization was to fix the position of the laser quarter wave plate and alternately position the waveplate in the luminescence arm to transmit either σ^+ and σ^- circular polarization, or vertical and horizontal linear polarization. To avoid steering the entrance slit image, the luminescence waveplate was placed at the intermediate image of the telescope. Since the cone angle was 3^o centered on the optic axis of the telescope, the effect of angular spread on the polarization measurement was negligible.

Ideally one would expect the luminescence circular polarization to change sign but not magnitude when the sense of laser polarization is reversed. There were several possible systematic error sources which could affect the polarization measurement: non-normal incidence of the optical pumping beam, non-ideal phase or angle between the fast and slow axes of the retardation plates, birefringence in the pyrex pipe vacuum jacket, and piezobirefringence in the strained gallium arsenide sample. The contribution of each of these potential effects is estimated below.

To analyse the polarization effects of an optical device, use is made of the Jones Calculus.[44] The E-vector for polarized light propagating in the z direction is represented by the Jones vector

$$E = \begin{pmatrix} a_x & e^{i\varepsilon_x} \\ a_y & e^{i\varepsilon_y} \end{pmatrix} \tag{4.2}$$

where a_x and a_y are the real values of the x and y time-averaged electric field and ε_x and ε_y are the relative phases of each component. The matrix for a non-retarding plate with principle axes in the x and y directions is

$$M_p = \begin{bmatrix} t_x^2 & 0 \\ 0 & t_y^2 \end{bmatrix} \tag{4.3}$$

where t_x and t_y are the amplitude transmission coefficients for x and y polarization components.

The matrix for a linear retarder with a fast x axis and retardation δ is given by

$$M_r = \begin{bmatrix} e^{i\delta/2} & 0 \\ 0 & e^{-i\delta/2} \end{bmatrix} . \tag{4.4}$$

The effect of a device on the polarization of the light is found by multiplying the light vector on the left by the device matrix. For a normalized Jones vector, the degree of circular polarization is given by

$$P_\sigma = 2a_x a_y \sin\delta \tag{4.5}$$

where $\delta = \varepsilon_x - \varepsilon_y$. The transmitted E-vector is related to the incident E-vector by

$$E_t = M_n \ldots M_1 E_i \quad . \tag{4.6}$$

With these equations the analysis of systematic effects can proceed.

1. Non-normal incidence of the laser beam on the sample

The absorbed beam is transmitted into the sample at an angle θ_t given by Snell's law

$$\sin\theta_t = \frac{1}{\hat{n}} \sin\theta_i \tag{4.7}$$

where $\hat{n}$ is the complex index of refraction $\hat{n} = n(1+iK)$. The imaginary part of $\hat{n}$ is related to the absorption coefficient α_o at wavelength λ_o by

$$\alpha_o = \frac{4\pi nK}{\lambda_o} \quad . \tag{4.8}$$

The change in polarization of the optical pumping beam after penetrating the crystal can be calculated using the Fresnel formulae for transmission. The real part of the refractive index in gallium arsenide is $n \simeq 3.5$. Assuming a value for the absorption of $\alpha \simeq 10^4$ cm^{-1} at $\lambda = 0.8 \times 10^{-4}$ cm, one obtains $K = 0.02$. Substitution into the Fresnel formulae with $\theta_i = 20^o$ gives the ratio of the transverse to parallel transmission amplitudes:[45]

$$\frac{t_\perp}{t_\parallel} = 0.97\, e^{-(0.0008)i} \quad . \tag{4.9}$$

If the Stokes vector for the incident light represents perfect circular polarization

$$E_i = \frac{1}{\sqrt{2}} \begin{pmatrix} e^{i\pi/2} \\ 1 \end{pmatrix} \tag{4.10}$$

then the Stokes vector for the light transmitted through the sample surface is

$$E_t = \begin{pmatrix} 0.696\ e^{i[(\pi/2)-0.0008)]} \\ 0.718 \end{pmatrix} . \tag{4.11}$$

Substitution in Eq. (4.5) gives the value $P_{\sigma t} = 0.9995$; therefore the amplitude and phase changes resulting from transmission through the surface produce a negligible change in the degree of circular polarization of the laser light. To a high degree of accuracy the crystal acts simply as a high index refractor, and the transmission angle is obtained from Eq. (4.6) by neglecting the complex part of $\hat{n}$; for $\theta_i = 20^o$, one computes $\theta_t = 5.6^o$.

The polarizaton vector for the electron spins is aligned along the axis defined by θ_t. The photoluminescence is detected along the crystal surface normal. From Eq. (3.21) the detected luminescence polarization is related to the spin polarization by

$$P_\sigma = P_h P_s \cos\theta_t = 0.995\ P_h P_s . \tag{4.12}$$

The effect of non-collinear luminescence and spin polarization axes is thus well within the experimental accuracy; furthermore it cannot cause a systematic asymmetry in the measured value, only a slight uniform reduction.

2. Nonideal waveplate retardation

From Eq. (4.5) it is seen that neither a difference in transmission for polarization components along the fast and slow axes, a deviation of δ from the ideal value of $\pi/2$, nor nonideal alignment with respect to the linear polarizer can produce a polarization asymmetry so long as the two azimuthal positions of the waveplate are exactly 90^{o} apart. With the optical rotation stages used, angular accuracy was better than $\pm 0.5^{o}$. Therefore only a uniform reduction in the degree of σ^{+} and σ^{-} polarizations could occur due to these effects. Since the degree of circular polarization of the reflected laser light was greater than 95%, the combined effect of both waveplates was less than a 5% reduction in polarization.

3. Birefringence of the vacuum window

The Pyrex pipe used as a transparent vacuum wall around the gallium arsenide sample and stress apparatus was annealed to relieve strain birefringence. After several furnace cycles, examination of the pipe between crossed polarizers showed that some strain remained. Given its fixed position in the optical system, the pipe could have produced a polarization asymmetry. This effect is represented by Fig. 4.8. However, when the system was set up to take the data reported herein, the magnitude of luminescence polarization from unstrained gallium arsenide was reproduced to within ±1% when the laser and luminescence waveplates were both flipped by 90^{o}.

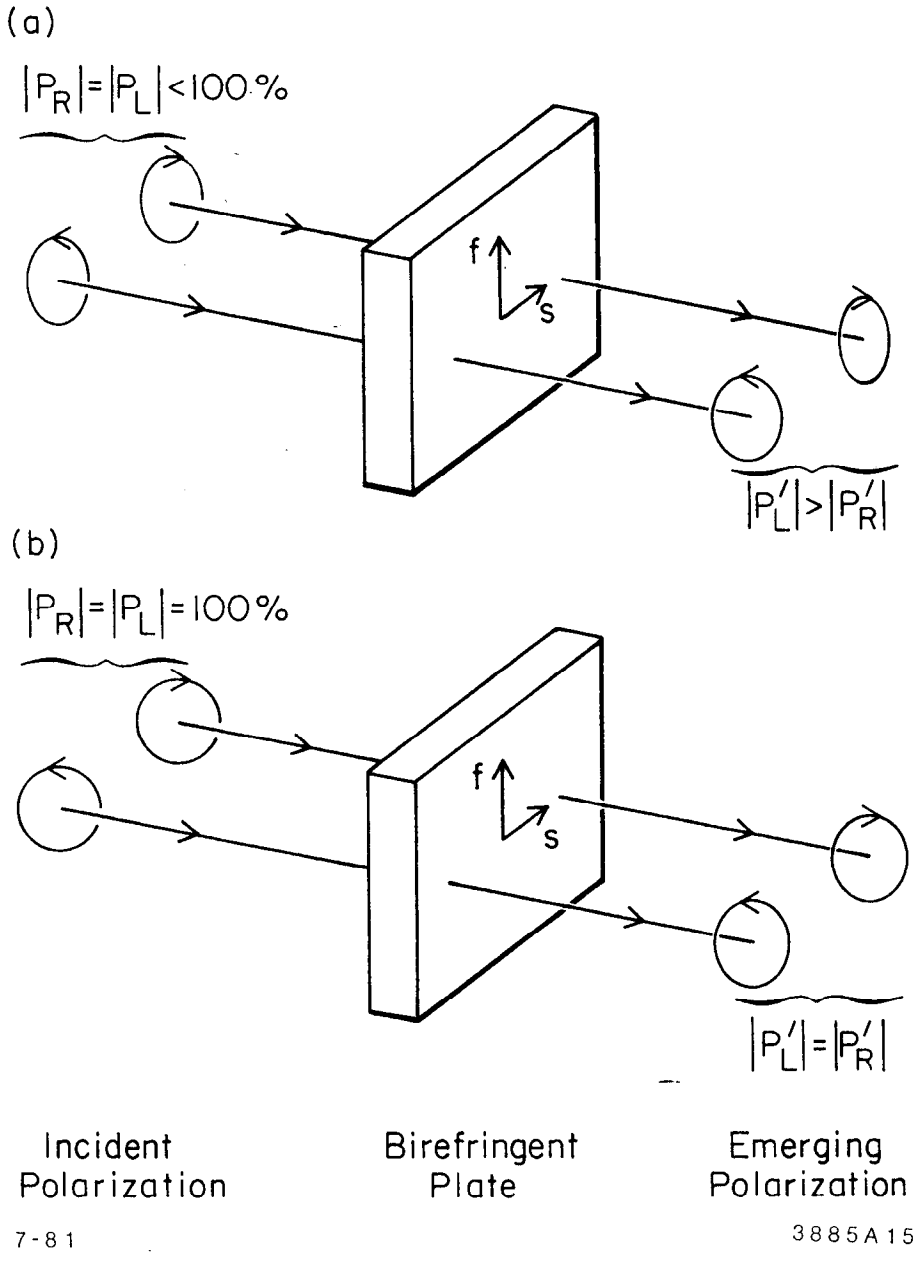

Fig. 4.8. Schematic of circular polarization asymmetry caused by a fixed retardation plate when the input beam polarization is reversed.

4. Piezobirefringence of the stressed GaAs sample

At a stress of 3.5 to 4 kbar the luminescence circular polarization showed a 4-5% asymmetry when the pump beam circular polarization was reversed. The luminescence was also slightly circularly polarized when the pump beam was linearly polarized. These effects were not observed at zero stress. We believed that they are due to stress-birefringence in the GaAs sample. Yu and coworkers[46] have measured the piezo-birefringence in p-type GaAs below the band gap at 300°K. They report a phase shift of $\simeq 130\pi$ rad cm^{-1} for $h\nu$ = 1.377 eV at 3 kbar stress. The effect of this phase shift on luminescence polarization can be estimated by considering the sample to be a retarder of thickness α^{-1}. Taking $\alpha \simeq 10^4$ cm^{-1}, the resulting retardation is $\simeq 0.04$ rad which gives a polarization asymmetry of sin(.04) = 4%. This qualitative estimate agrees quite well with the observed asymmetry in the stressed sample.

4.6. Detection Electronics

A block diagram of the detection electronics is presented in Fig. 4.9. Photoluminescence signal pulses were detected with an S1 response photomultiplier (PMT), which was either an RCA 7102 or an Amperex 150 CVP, cooled to -20°C. Laser pulses were monitored with a PIN photodiode. PMT pulses were amplified by a preamp circuit and integrated by an Evans Associates 4130 gated integrator module.[47]

Signal pulses were integrated by an identical circuit. The signal intensity was normalized on each pulse to the laser intensity by an Evan 4122 ratiometer whose output was passively filtered with a variable time constant RC low-pass filter and recorded on a chart recorder or X-Y

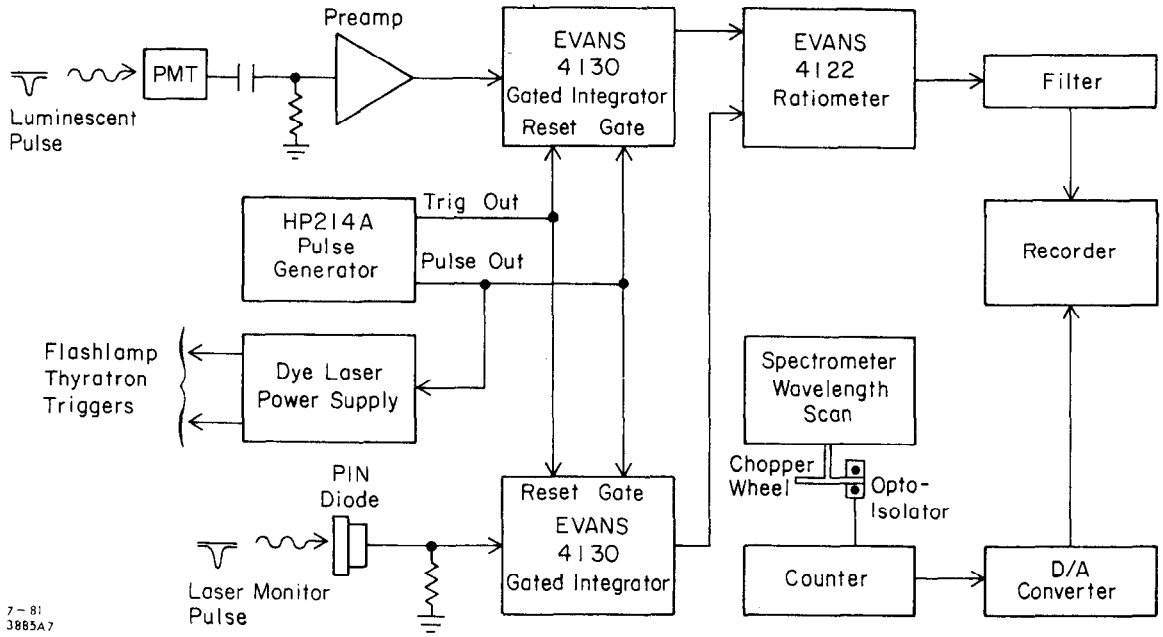

Fig. 4.9. Block diagram of signal detection electronics.

plotter. Figure 4.6b shows typical oscilloscope traces for the PMT signal and gated integrator output. The precursor pulse on the PMT cable was due to distributed pickup of rfi produced by the switching of the thyratrons in the flashlamp circuitry. This was electronically suppressed by proper adjustment of the integrator gate width and delay controls.

Low laser power at the wavelengths of interest and an erratic beam spot were the primary difficulties in the measurement. With the luminescence band peak at ≃8300Å, band edge optical pumping required the use of HITC dye on the shoulder of its tuning curve. The range of HITC excitation wavelengths available was limited to ≃8050Å on the short-λ side by power drop-off and to ≃8275Å on the long-λ side by washout of the signal by scattered laser light. At the peak of the luminescence band, using a slit width of 0.5 mm and maximum PMT gain, the signal pulse typically contained $\simeq 10^2$ photoelectrons. Pulse to pulse fluctuations were much larger than could be attributed to photoelectron statistics and were possibly due spatial noise in the laser output beam.

At 10 pps, it was empirically found that a filter time constant of at least 12 sec was required to obtain a sufficiently steady signal for the desired polarization resolution. Such a time constant required an exceedingly long scan time (> 1 hr) to record complete spectra that were free of filter distortion. When such spectra were recorded under these conditions, drifts in PMT temperature (and gain), laser power, and integrator offset commonly caused errors exceeding the desired resolution. For this reason all polarization data on dye laser excited luminescence was recorded at discrete wavelengths. The waveplate was alternately set

at each of the 2 orthogonal polarizations and the filtered output was recorded for a period of several minutes. Later, the recorder trace was sampled by hand at intervals of one filter time constant. The resulting sampling was treated as a set of independent observations of intensity of one polarization point was computed from a pair of such average intensities.

When accurate spectra were required without regard to spin orientation, as with the measurement of strain splittings, a helium-neon laser was used to excite cw luminescence. The signal was modulated with a chopper wheel and detected with a lock-in amplifier.

Chapter V

DATA AND DISCUSSION

5.1. Photoluminescence Lineshape

5.1.1. Recorded spectra

The photoluminescence spectrum for unstrained p-type GaAs at $100^{o}K$ with a quoted Zn impurity density of 1×10^{18} cm^{-3} is shown in Fig. 5.1 for excitation by a cw helium-neon laser at 6328Å and for pulsed dye laser excitation at 8220Å. The cw signal was chopped at 43 cps and synchronously detected using a PAR HR-8 lock-in amplifier. Typical conditions were a slit resolution of 10Å, a 3 sec filter time constant, and a 10Å/min scan rate. The pulsed signal occured at a 10 pps rate and was detected by 2 gated integrators and a ratiometer which produced a luminescence signal nominally normalized to the laser pulse energy. The slit resolution and scan speeds were identical to the cw conditions, but pulse-to-pulse jitter required a 2-stage low-pass filter with a time constant of about 17 sec. The luminescence was collected in a direction perpendicular to the sample surface, with pulsed and cw laser beams incident at 20^{o} and 10^{o} to the surface normal, respectively. The specularly reflected laser beam in each case passed outside the acceptance cone of the luminescence telescope objective. In the case of the dye laser excited spectrum, the intensity of the laser relative to the luminescence was greatly attenuated by setting the polarization analyser to block the major polarization component of the scattered laser light.

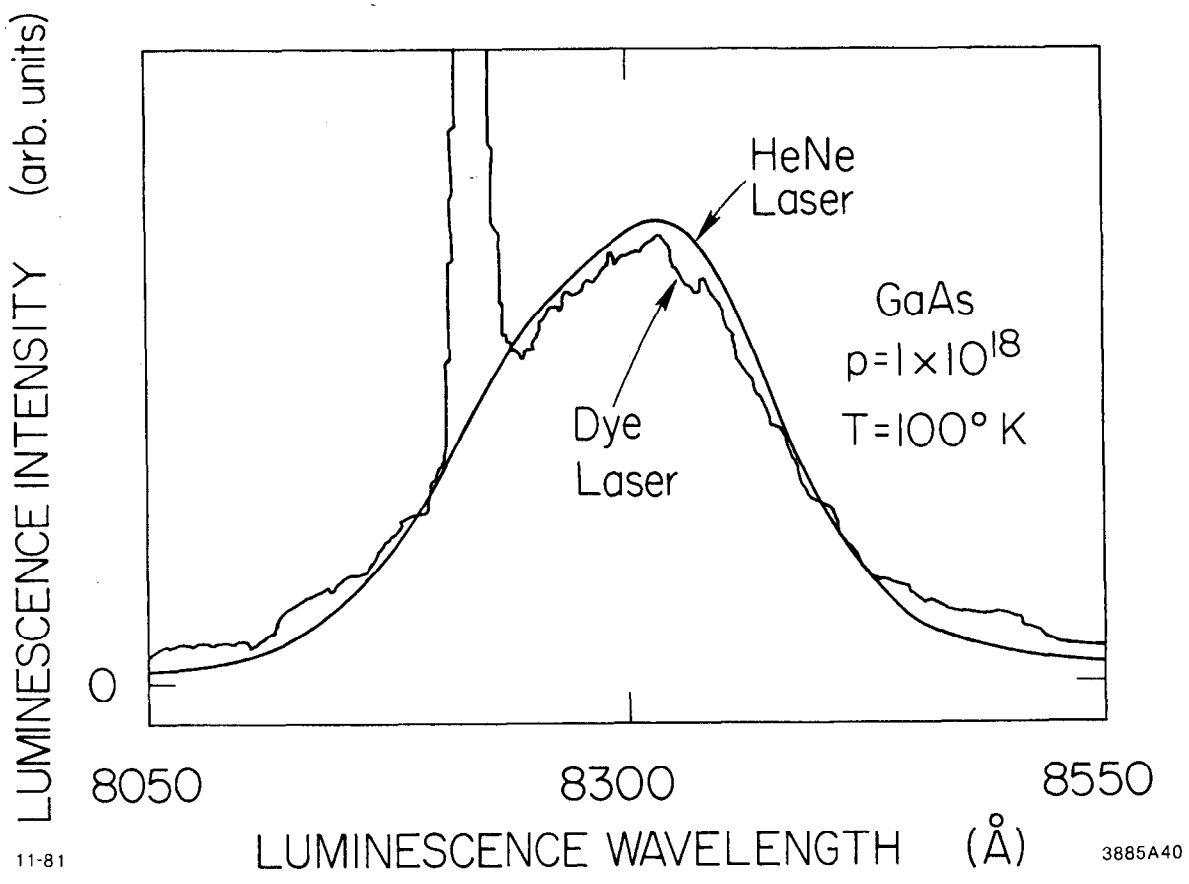

Fig. 5.1. Photoluminescence spectra for laser excitation at 6328Å (a), and 8200Å (b).

5.1.2. Relation between luminescence and absorption spectra

In a semiconductor crystal at thermal equilibrium the relation between the absorption coefficient and emission intensity is expressed by the van Roosbroeck-Shockley relation[48]

$$I^{o}(h\nu) = \frac{8\pi n^{2} (h\nu)^{2} \alpha(h\nu)}{h^{3}c^{2}\left[\exp\left(\frac{h\nu}{kT}\right) - 1\right]} \tag{5.1}$$

where $I^{o}(h\nu)$ is the emission rate in photons sec^{-1} eV^{-1}, n is the index of refraction, and $\alpha(h\nu)$ is the absorption coefficient. Since near infrared photon energies are of interest, Eq. (5.1) can be rewritten

$$I^{o}(h\nu) = \frac{8\pi n^{2}}{h^{3}c^{2}} (h\nu)^{2} \alpha(h\nu) \exp\left(-\frac{h\nu}{kT}\right) . \tag{5.2}$$

It has been pointed out[49] that for weak excitation of a crystal, the spectral shape of the emission is still given by Eq. (5.2) while the intensity increases uniformly. The scale factor can be written[50,51]

$$I(h\nu) = \frac{np}{n_{o}p_{o}} I^{o}(h\nu) \tag{5.3}$$

where n(p) is the electron (hole) density under excitation, and $n_{o}(p_{o})$ is the equilibrium density.

The requirements for this expression to be valid are that:

1) Quasi-equilibrium must be established for the carriers in each band.
2) The nonequilibrium majority carrier density must be close to its equilibrium value ($\Delta p << p_{o}$ in a p-type crystal).

The first condition will be satisfied since the thermalization time ($\simeq 10^{-13}$ sec) is much shorter than the recombination lifetime

($\simeq 10^{-10}$ sec).[49] Condition (2) must be verified by estimating the density of photo excited carriers. Let P be the power in the cw excitation beam and λ be its wavelength. The photon flux is computed to be

$$F_p = \frac{P\lambda}{2 \times 10^{-16}} \tag{5.4}$$

with F_p in photons sec^{-1}, P in watts, and λ in nm. The photocarrier density for steady excitation is[52]

$$\Delta p = \frac{(1-R)\,\alpha\,\tau_r\,F_p}{A} \tag{5.5}$$

where A is the illuminated area on the sample surface, R is the surface refelctivity, α the absorption coefficient, and τ_r the recombination lifetime. For GaAs $\tau_r \simeq 3 \times 10^{-10}$ sec and $R \simeq 0.3$.[53,54]

Using a 1 mW helium-neon laser for illumination, $\alpha \simeq 5 \times 10^4$ cm^{-1}; with a .25 mm diameter illuminated spot, we obtain $\Delta p \simeq 5 \times 10^{13}$ cm^{-3}. The excess hole density is therefore much smaller than the equilibrium value even allowing for wide variations in the assumed parameter values. For pulsed excitation, assuming a pulse width much longer than τ_r, the excitation is quasi-continuous and Eq. (5.4) can be used with P equal to the power averaged over the pulse duration. Typical dye laser pulse parameters were an energy of 1 J and a width of 500 nsec, so $P \simeq 2W$. For a wavelength of 820 nm, $\alpha \simeq 10^4$ cm^{-1}, giving $\Delta p \simeq 2.5 \times 10^{15}$ cm^{-3}. Again, the density of photo-holes is much lower than the equilibrium density. Therefore the observed spectral shape should be given by Eq. (5.2).

In agreement with the conclusions regarding the independence of the luminescence lineshape on the excitation source, Fig. 5.1 demonstrates that part of the band edge excited luminescence spectrum is emitted at a higher photon energy than the laser light, indicating that recombination occurred under quasi-equilibrium conditions. The recorded spectral shapes for cw and pulsed laser excitation are quite close; minor differences may well be attributed to the increased noise associated with pulsed as opposed to cw excitation.

5.1.3. Determination of absorption edge from luminescence spectrum

Equation (5.2) was used to calculate the absorption near the band gap from the measured photoluminescence spectrum. Since the absolute magnitude of the recorded intensity was unknown, the calculation gives $\alpha(h\nu)$ within an overall multiplicative constant. The latter was adjusted to give $\alpha = 5 \times 10^3$ cm^{-1} at the peak of the luminescence band in agreement with a model calculation of room temperature absorption and emission by Casey and Stern.[55] The result is presented in Fig. 5.2 together with the luminescence spectrum corrected for PMT sensitivity and converted to an energy scale. It is seen from the calculated curve that the absorption has a low energy exponential edge that merges with a high energy parabolic portion. In the model of Casey and Stern, this junction roughly coincides with the nominal (parabolic band) energy gap. Since the present calculation shows this point occuring roughly at the same energy as the luminescence peak, the peak position was used to monitor the strain-induced shift and splitting of E_g, as described in the next section. The calculated slope of the exponential absorption edge is in good agreement with the value of $d\ell n\alpha/dh\nu = 0.08$ meV^{-1} obtained from

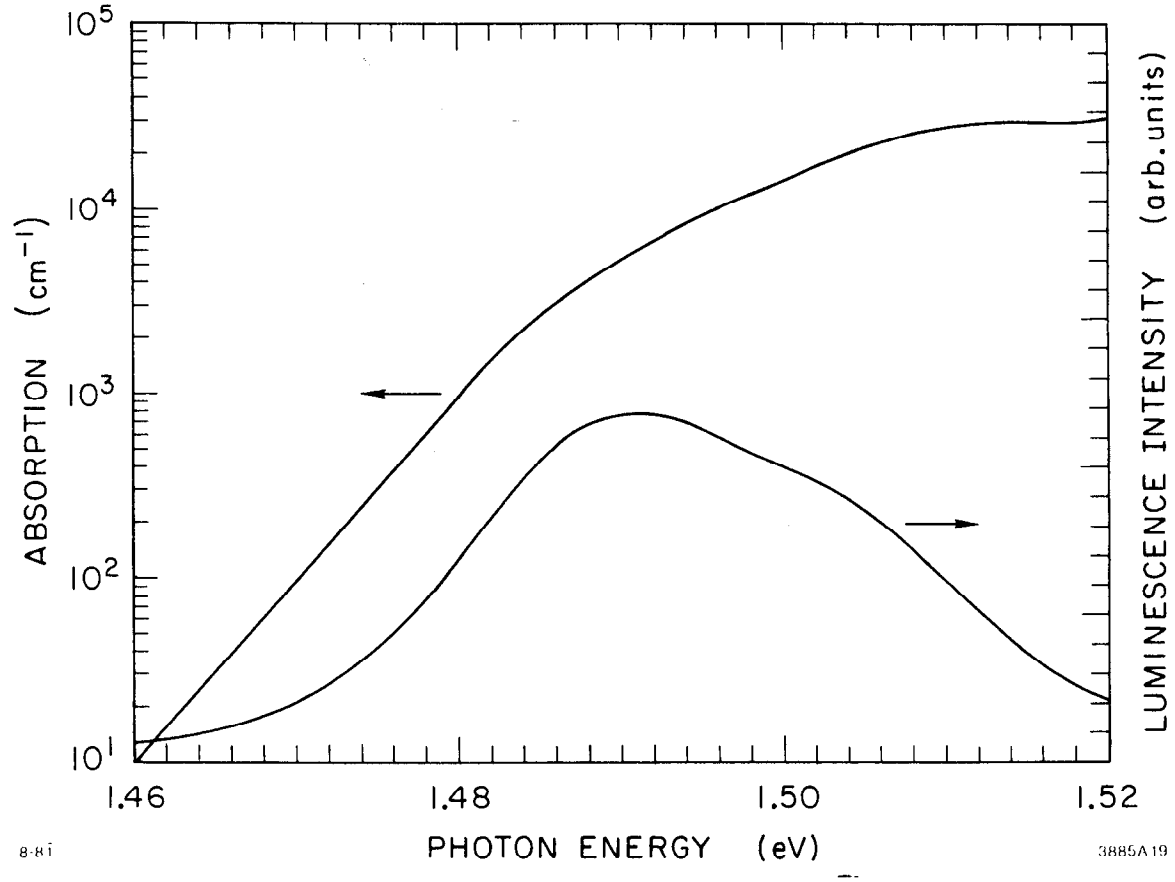

Fig. 5.2. Absorption edge calculated from measured luminescence spectrum by the van Roosbroeck-Shockley relation. Luminescence spectrum corrected for PMT sensitivity.

the data of Redfield and Afromowitz[56] for uncompensated GaAs with $p = 1.6 \times 10^{18}$ cm^{-3} at 100°K.

The temperature dependence of the band gap energy is described by the Varshni equation[57]

$$E_g(T) = E_g(0) - \frac{aT^2}{(b + T)} \quad . \tag{5.6}$$

The parameter values for GaAs are $a = 5.405 \times 10^{-4}$ eV K^{-1} and $b = 204$°K.[55] The dependence of the energy gap on the impurity concentration can be empirically included in the Varshni equation by the relation[55]

$$E_g(0) = 1.519 - 1.6 \times 10^{-8} \, p^{1/3} \text{ eV} \quad . \tag{5.7}$$

Equations (5.6) and (5.7) were used to determine the sample temperature independently of the diode thermometer attached to the cold finger. By this method the sample temperature was measured to be ≃100°K with liquid nitrogen cooling of the dewar vessel. On a few assemblies of the stress apparatus the sample was found to be at a higher temperature, which is believed to be due to a loose lock ring between the cold finger and the base of the dewar.

5.2. Strain Splitting of Linearly Polarized Photoluminescence

5.2.1. Recorded spectra

Under the conditions of zero applied stress and linearly polarized excitation light, the photoluminescence is unpolarized. Figures 5.3, 5.4, and 5.5 show the change in the luminescence spectra polarized in the vertical plane (parallel to the strain axis) and in the horizontal

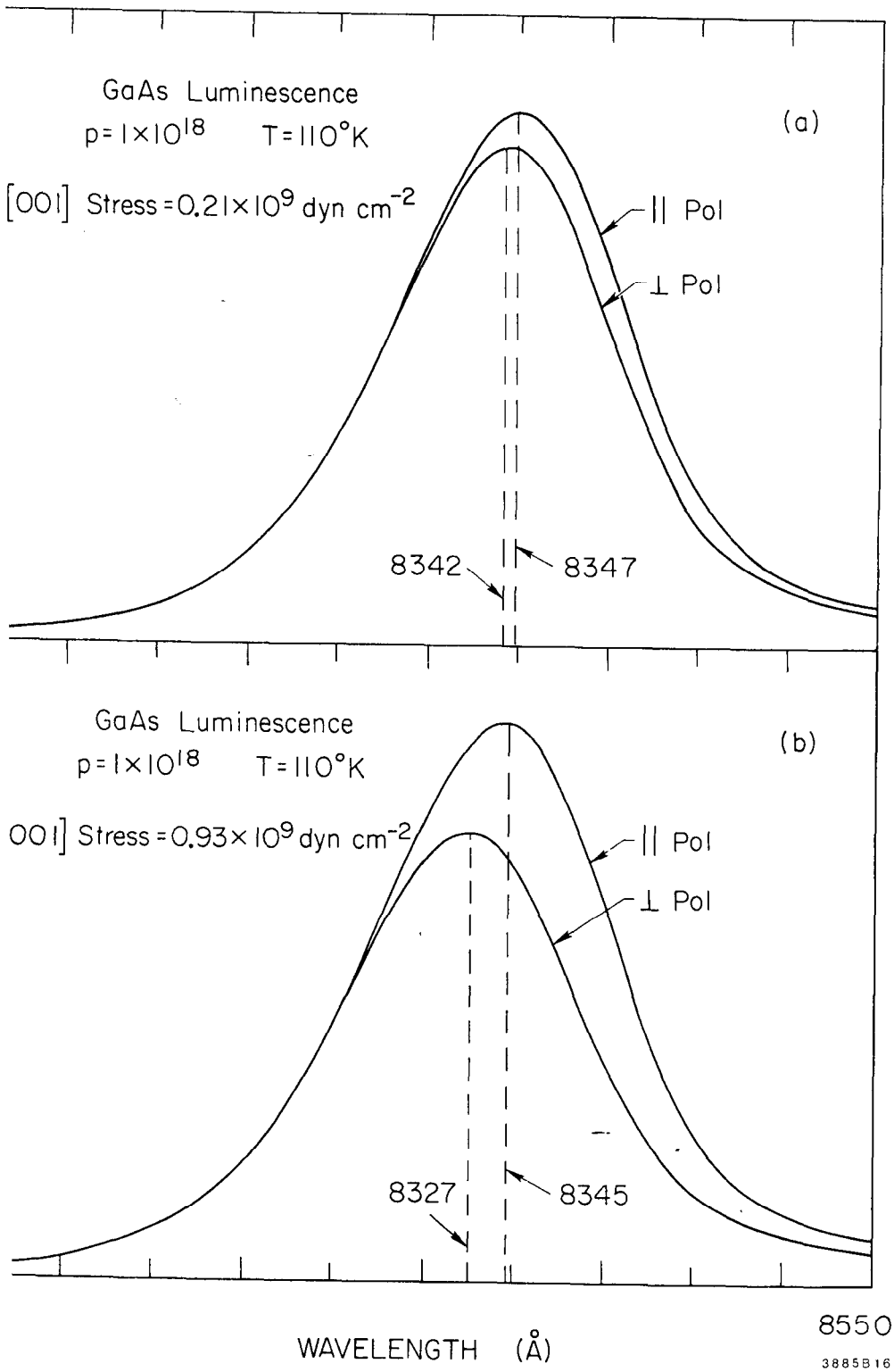

3.3. Linearly polarized luminescence components at low stress.

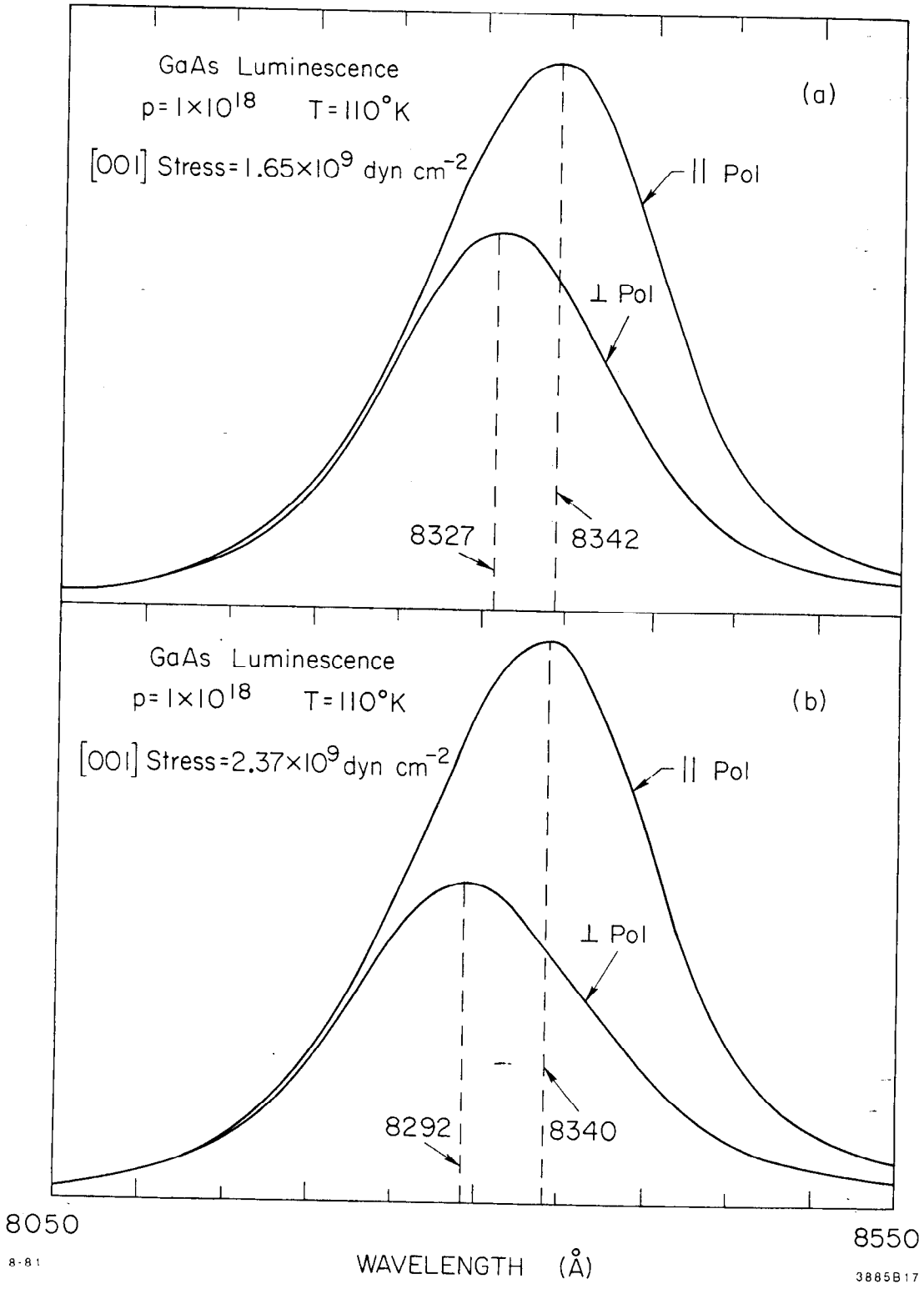

Fig. 5.4. Linearly polarized luminescence components at intermediate stress.

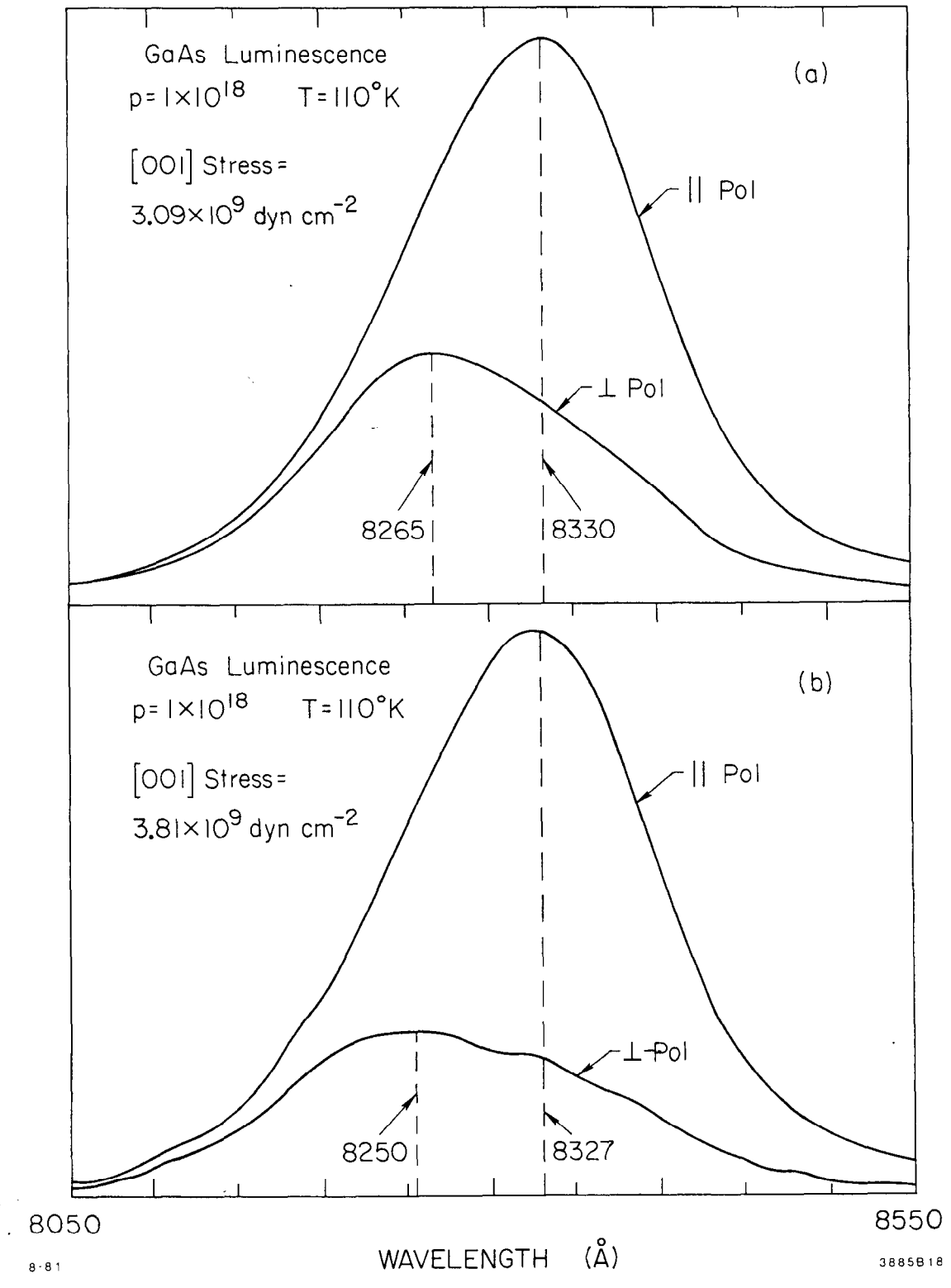

Fig. 5.5. Linearly polarized luminescence components at high stress.

plane (transverse to the strain axis). The luminescence was collected at a right angle to strain axis. Detection was as described in Sec. 5.1 for cw excitation.

The vertically polarized (∥) component preserves its lineshape while shifting toward shorter λ. The shape and intensity of the horizontally polarized (⊥) component changes significantly under applied stress; at a high stress two peaks are resolved, one aligned with the ∥ peak and one at a shorter wavelength. The separation between the ∥ and short wavelength ⊥ peaks are plotted against applied stress in Fig. 5.6. In the next section, we describe the method of calculating the band gap splitting as a function of applied stress from the data of Figs. 5.3-5.5.

5.2.2. Valence band strain splitting

The luminescence polarization is governed, via the correspondence principle, by the dipole matrix elements between the conduction band and the appropriate valence band as given in Eq. (3.18). Absorption of linearly polarized light creates no spin polarization and the normalized electron spin density matrix is obtained by setting $P_s = 0$ in Eq. (3.5), leaving

$$F = \delta_{mm'} \tag{5.8}$$

substitution of Eq. (5.8) in Eq. (3.18) gives the relative intensities of each polarization component:

$$\mathscr{E}_i^2 = \sum_m \langle m|x_i|\mu\rangle \langle \mu|x_i|m\rangle \ . \tag{5.9}$$

For heavy-hole recombination, $\mu = \pm 3/2$; for light-holes, $\mu = \pm 1/2$. Substituting the appropriate wave functions from Table 2.1 it is found

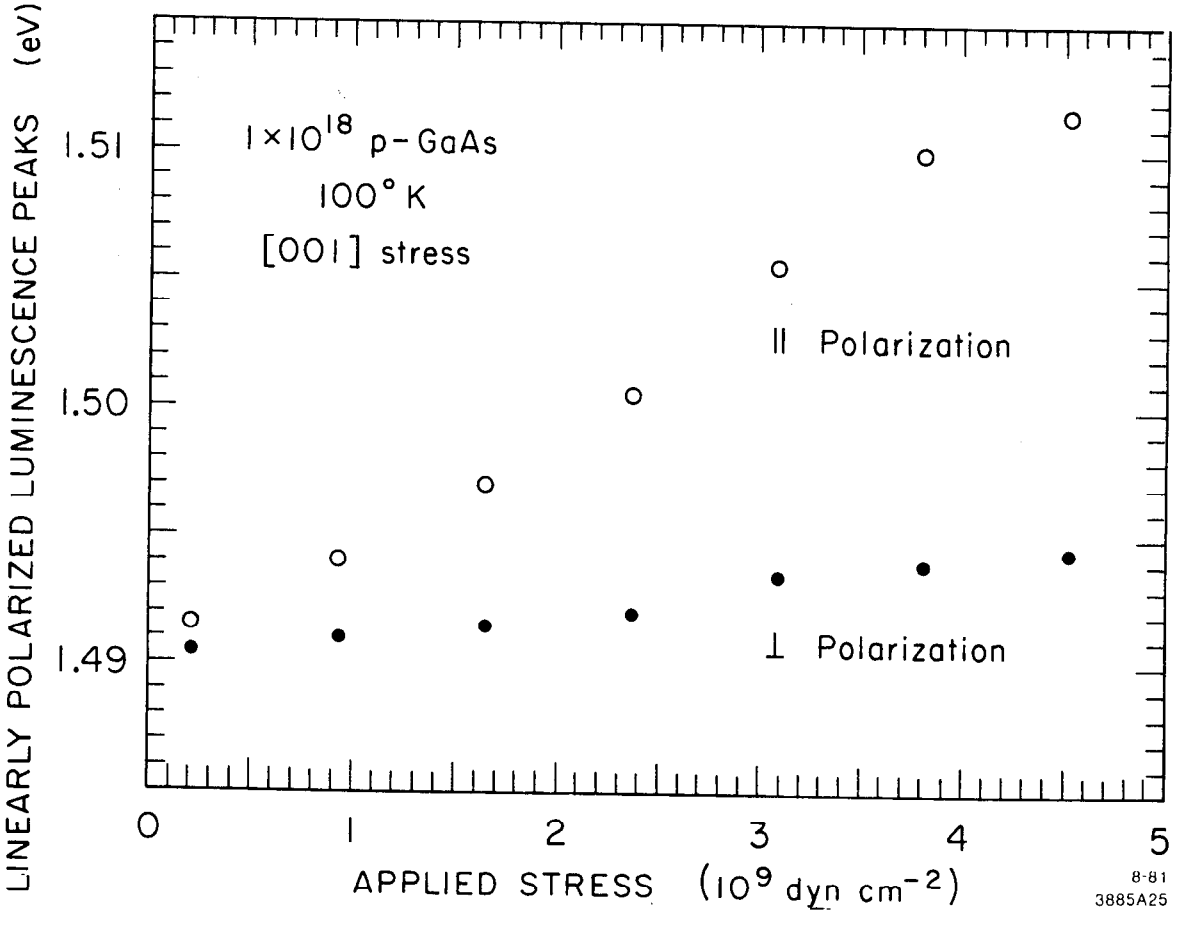

Fig. 5.6. Stress splitting of polarized luminescence peaks.

that $\mathcal{E}_i^2$ is the same for both signs of μ in each valence band and that

$$(\mathcal{E}_z^{(V_1)})^2 : (\mathcal{E}_x^{(V_1)})^2 : (\mathcal{E}_y^{(V_1)})^2 = 0 : 1 : 1 \qquad (5.10a)$$

and

$$(\mathcal{E}_z^{(V_2)})^2 : (\mathcal{E}_x^{(V_2)})^2 : (\mathcal{E}_y^{(V_2)})^2 = \frac{2}{3} : \frac{1}{6} : \frac{1}{6} \qquad (5.10b)$$

where the relative scale is the same in both ratios.

At zero strain the direction of the z-axis must be averaged over, resulting in zero net linear polarization for recombination with either band. Under a large strain the z axis is fixed, resulting in 60% vertical polarization for light-hole recombination and 100% horizontal polarization for heavy-hole recombination.

The splitting between the heavy-and light-hole valence band edges was determined from the linearly polarized luminescence spectra under the assumption of complete orientation of the z axis along the direction of strain for all non-zero values of applied stress. It is assumed that the peak of the <u>total</u> emitted luminescence intensity for each band corresponds to its respective band gap energy. The following derivation relates the total intensity to the linearly polarized components detected in the particular direction of observation.

Let z be the strain axis and y be the direction of luminescence detection. The relations between the polarized luminescence intensities detected from each band and the total emitted intensities are, using Eq. (5.10), for V_2 recombination,

$$I_{\parallel}^{(V_2)}(\lambda) = \frac{2}{3} I_{tot}^{(V_2)}(\lambda) \tag{5.11a}$$

and

$$I_{\perp}^{(V_2)}(\lambda) = \frac{1}{6} I^{(V_2)}(\lambda) \tag{5.11b}$$

and for V_1 recombination

$$I_{\parallel}^{(V_1)}(\lambda) = 0 \tag{5.12a}$$

$$I_{\perp}^{(V_1)}(\lambda) = \frac{1}{2} I^{(V_1)}(\lambda) \quad . \tag{5.12b}$$

The total linear polarization intensities are found by adding Eqs. (5.11) and (5.12):

$$I_{\parallel}(\lambda) = I_{\parallel}^{(V_1)}(\lambda) + I_{\parallel}^{(V_2)}(\lambda) \tag{5.13a}$$

$$I_{\perp}(\lambda) = I_{\perp}^{(V_1)}(\lambda) + I_{\perp}^{(V_2)}(\lambda) \quad . \tag{5.13b}$$

Finally, substituting Eqs. (5.11) and (5.12) in (5.13),

$$I^{(V_2)}(\lambda) = \frac{2}{3} I_{\parallel}(\lambda) \tag{5.14a}$$

$$I^{(V_1)}(\lambda) = 2I_{\perp}(\lambda) - \frac{1}{2} I_{\parallel}(\lambda) \quad . \tag{5.14b}$$

The V_2 luminescence lineshape is therefore given by the recorded $\parallel$ component. The V_1 luminescence spectrum was computed by subtracting 1/4 of the $\parallel$ component intensity from that of the $\perp$ component. The calculated energy gaps are plotted in Fig. 5.7 against the applied stress.

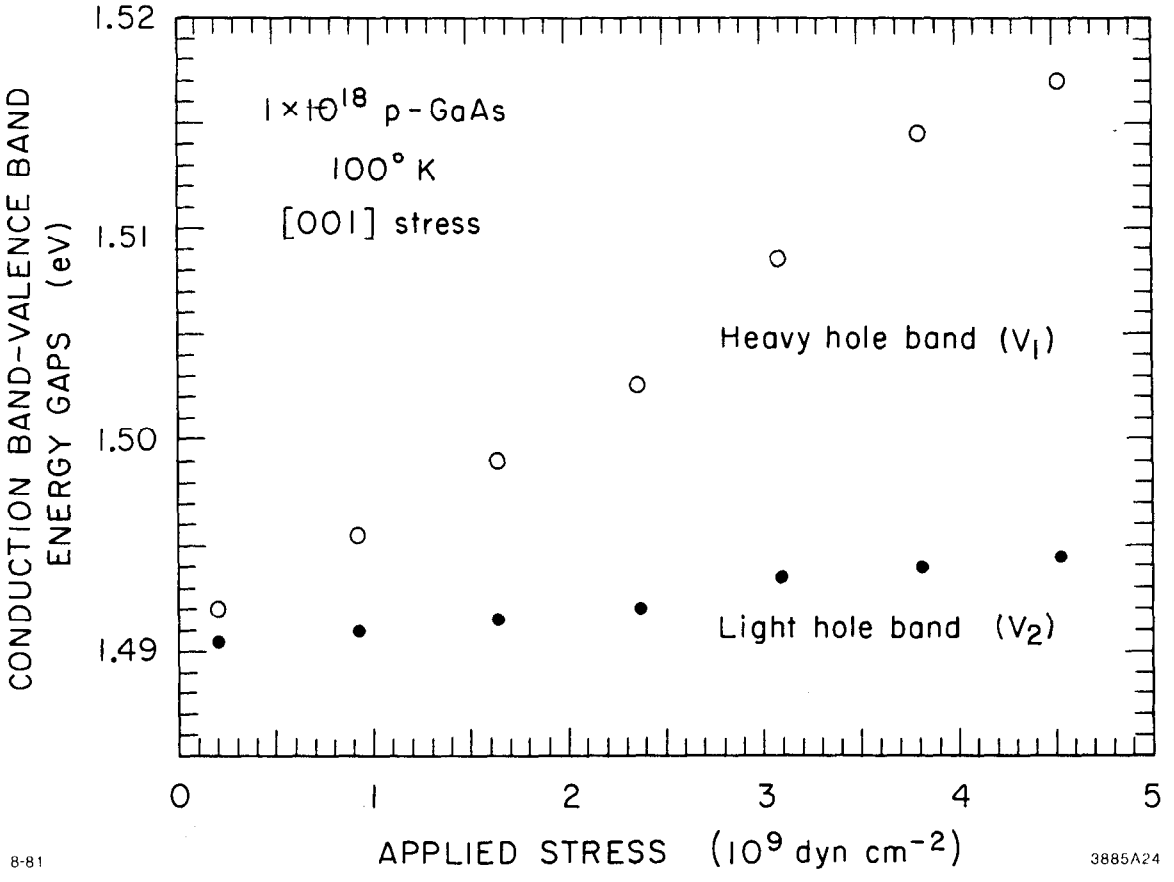

Fig. 5.7. Stress splitting of upper $P_{3/2}$ valence band edges.

An approximately linear shift of each valence band with respect to the conduction band is observed as well as a linear valence band splitting. Values for the uniaxial deformation potential were taken as the ratio of energy splitting to applied stress for each pair of data points. Using experimental uncertainties of ±1.8 meV and ±0.16 kbar the weighted mean and mean standard deviation give the experimental value of

$$\frac{\bar{\partial}}{\partial \chi} \delta_s = 4.98 \pm 0.45 \times 10^{-12} \text{ eV bar}^{-1} \quad . \qquad (5.15)$$

This value is in reasonably good agreement with the value of 6.2 ± 0.3 meV kbar^{-1} obtained by workers using electroreflectance spectroscopy on stressed GaAs crystals.[20]

5.3. Stress and Spectral Dependence of Polarized Luminescence

5.3.1. Complete spectra

The components of circularly polarized luminescence for band edge optical pumping are shown in Fig. 5.8 for a high applied stress of 3.9×10^9 dyn cm^{-2}. The lowest stress used corresponds to the minimum value obtainable in the completely assembled stress apparatus. When the bellows was at 0 PSIG referred to the room, evacuation of the dewar caused a sample stress of $\simeq 0.2 \times 10^9$ dyn cm^{-2}. For all observable features reported in this section, this low stress was equivalent to zero. The high stress value of $\simeq 4.0 \times 10^9$ dyn cm^{-2} was a somewhat arbitrarily chosen upper limit to a working range above which sample breakage was highly probable.

The luminescence peak shifted from λ = 8312Å to 8290Å as the pressure was varied from the low to high stress limits. This shift roughly

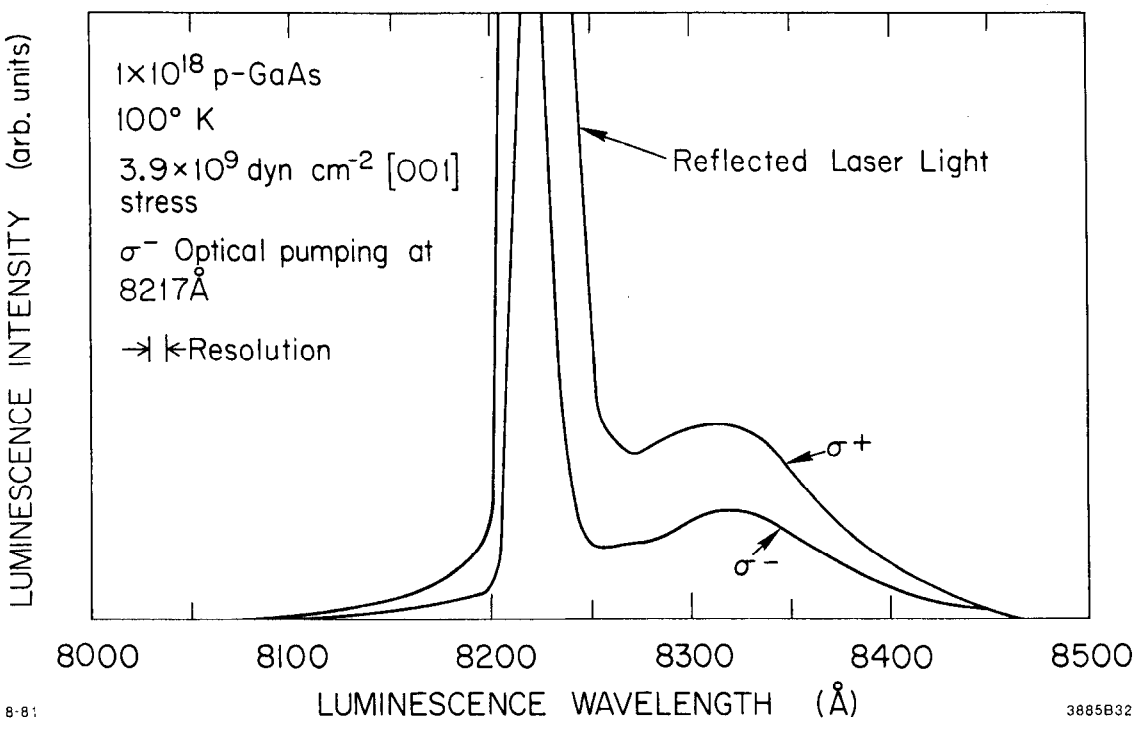

Fig. 5.8. Spectra of circularly polarized luminescence components (hand-smoothed) for optical pumping at 8217Å at high stress.

corresponded to the shift of the V_2 band gap. This is consistent with the observation (cf. Fig. 5.5b) that the hole population is predominantly in the upper valence band at high stress. Figure 5.8 shows that, for the spectrometer slit resolution used, luminescence polarization measurements were uninfluenced by the laser line outside a ≃75Å window centered at the latter. The spectrum in Fig. 5.8 is presented to show qualitative features only; all quantitative polarization measurements discussed in the remainder of this chapter were recorded pointwise at static settings of stress and wavelength by the methods described in Sec. 4.6.

5.3.2. Circular polarization at low stress

The "unstressed" polarization at the peak of the luminescence band is shown in Fig. 5.9 plotted against the photon energy of the laser. The magnitude of P_σ was preserved (within the experimental error) when the laser polarization was switched from σ^+ to σ^-. The polarization was also found to be uniform across the luminescence band. The gradual falloff in polarization we observed with increasing $h\nu_{laser}$ has also been reported by other workers using both luminescence[74] and photoemission[58] detection, and is due to the increasing admixture of the V_2 band wave function with that of the V_3 band.

5.3.3. Circular polarization at high stress

The polarization measured near the high stress luminescence peak for both σ^+ and σ^- laser polarization is plotted against laser energy $h\nu$ in Fig. 5.10. Several prominent features of this polarization-tuning curve are evident:

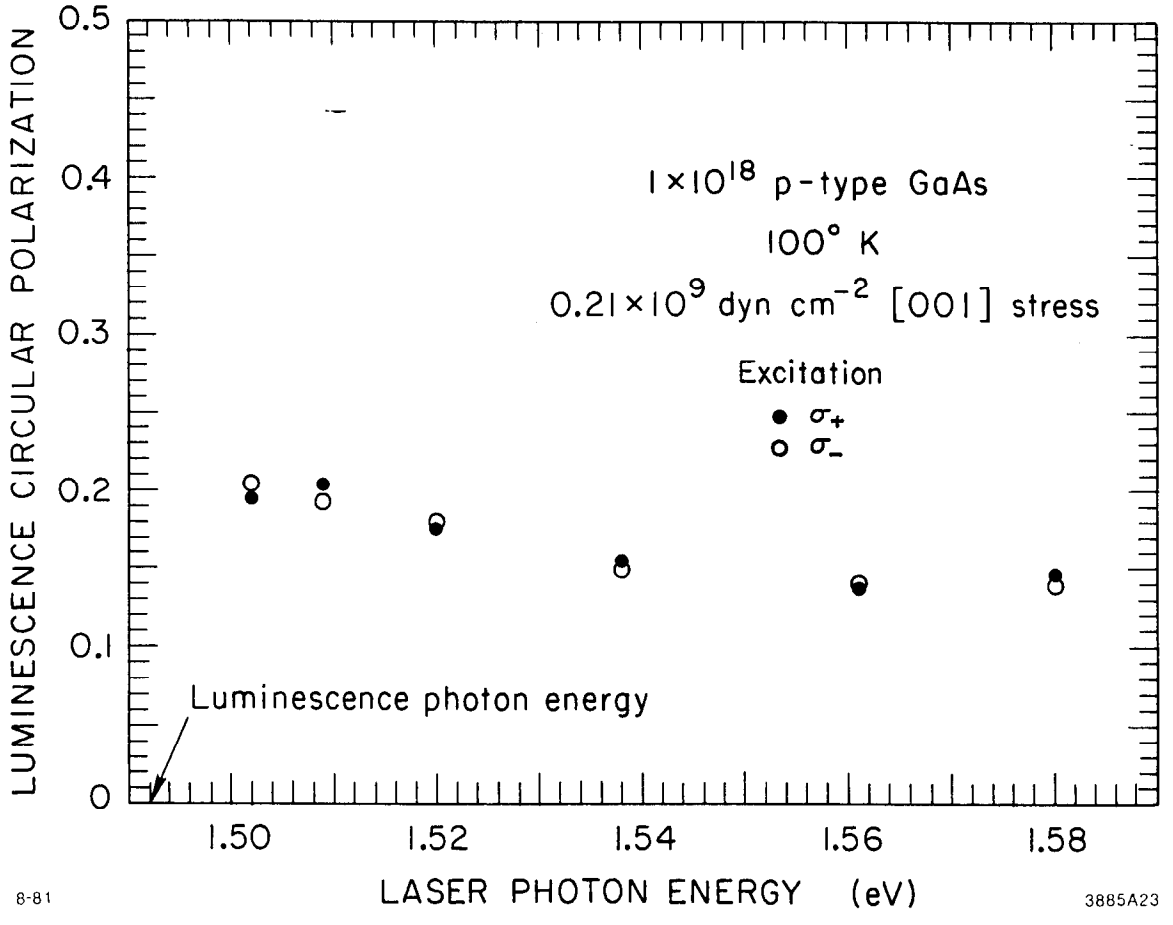

Fig. 5.9. Dependence of circular polarization at luminescence peak on laser photon energy at low stress. Open circles, $\sigma+$ excitation; filled circles, $\sigma-$ excitation.

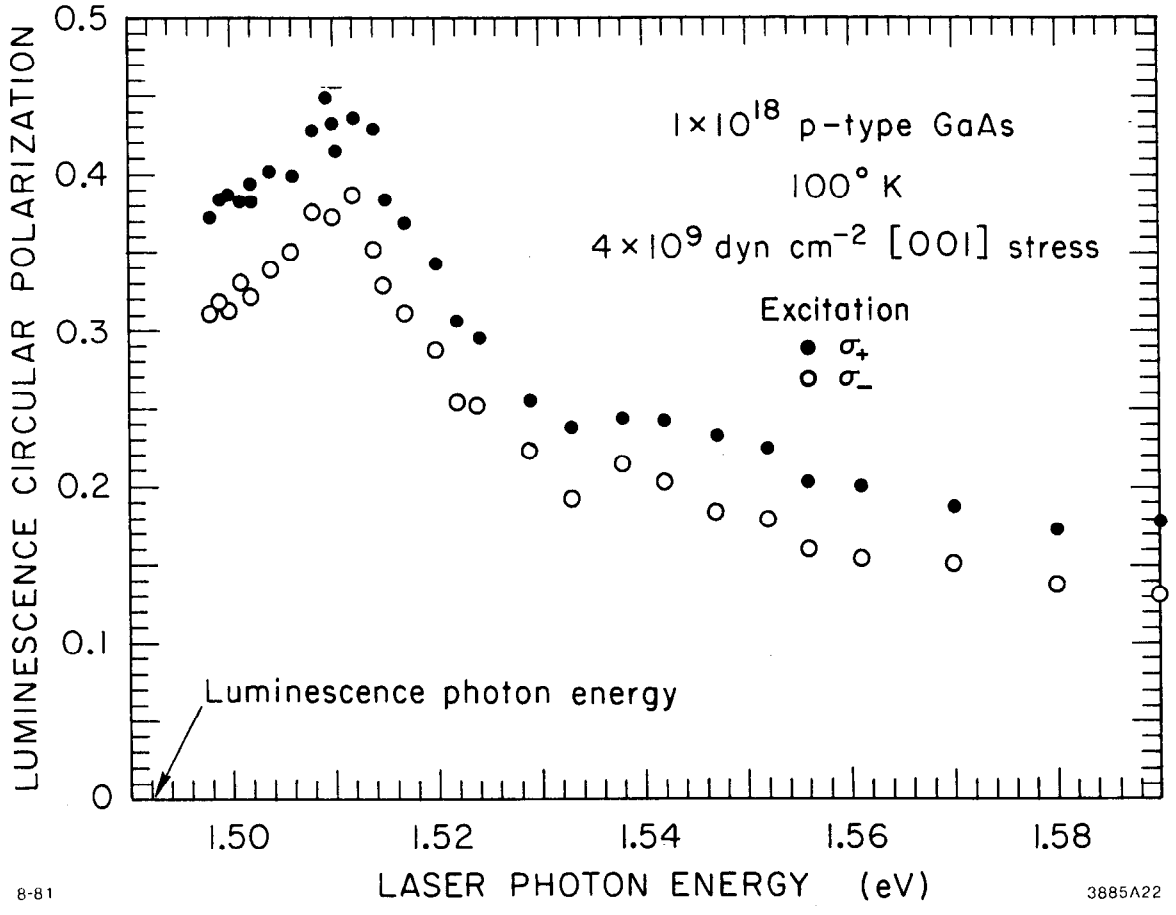

Fig. 5.10. Dependence of circular polarization at luminescence peak on laser photon energy at high stress. Open circles, σ_+ excitation; filled circles, σ_- excitation.

(a) A difference in P_σ with respect to the rotation sense of the laser circular polarization is observed. The asymmetry has a value of $\simeq$5% which is approximately uniform over most of the laser tuning shown, with a slight increase at the lowest photon energies. This asymmetry, which is not observed at zero stress, is attributed to stress birefringence in the GaAs sample. Both the laser and luminescence beams pass through a layer of the birefringent sample; however, only the effect of birefringence on the emerging luminescence beam contributes to the asymmetry. Two beams of 100% circular polarization rotating oppositely are depolarized by equal amounts by the birefringence. On the other hand, for two counterrotating beams of equal polarization magnitude less than 100%, the phase change caused by the birefringence will increase the polarization of one beam and reduce that of its counterpart. Figure 4.8 represents these situations schematically. In the discussion in Sec. 4.5 on systematic error sources, the stress birefringence and its effect on the pump light polarization was modeled by a retardation plate of thickness α^{-1} and analysed with the Jones polarization matrix formalism to demonstrate agreement with direct measurements of the piezobirefringence coefficient. Strictly speaking, the luminescence is only partially polarized (the length of its Stokes polarization vector is less than unity) and should therefore be treated by the Mueller matrix formalism.[59] However the value of the circular polarization change is the same in either calculation. The corrected value of P_σ can with little error be taken as the average of the values for left- and right-circular laser polarization.

(b) The luminescence polarization measured at the band peak shows three distinct regions in its dependence on laser tuning. Moving from high to low laser photon energy these are: a region of gradual increase, a steeply rising portion between a local minimum at 1.532 eV and a maximum at 1.512 eV, and a region of significant rolloff. The points delimiting the steep portion are separated by just the measured valence band splitting.

(c) P_σ is uniform with respect to luminescence wavelength for the laser tuning regime of $h\nu_{laser} < 1.508$ eV (corresponding to $\lambda_{laser} <$ 8225Å). For $h\nu_{laser} < 1.503$ eV (corresponding to $\lambda > 8250$Å) a distinct falloff in P_σ towards the long wavelength side of the luminescence band was observed. This falloff became increasingly pronounced as the laser was tuned to longer wavelengths. The value of P_σ averaged over the two laser waveplate settings is plotted against luminescence wavelength for several laser tuning settings in Fig. 5.11.

5.3.4. Stress dependence of maximum luminescence polarization

With the laser tuned to the position of the polarization maximum of Fig. 5.10 and the luminescence wavelength fixed at 1.492 eV (8310Å), the polarization and asymmetry were recorded as a function of applied stress. These data are shown in Fig. 5.12. The position of the polarization maximum is believed to shift with stress because this point is associated with the position of the upper valence band edge. The very slow data acquisition rate precluded production of curves similar to Fig. 5.9 and Fig. 5.10 for intermediate stress values in order to resolve a possible shift in the maximum position.

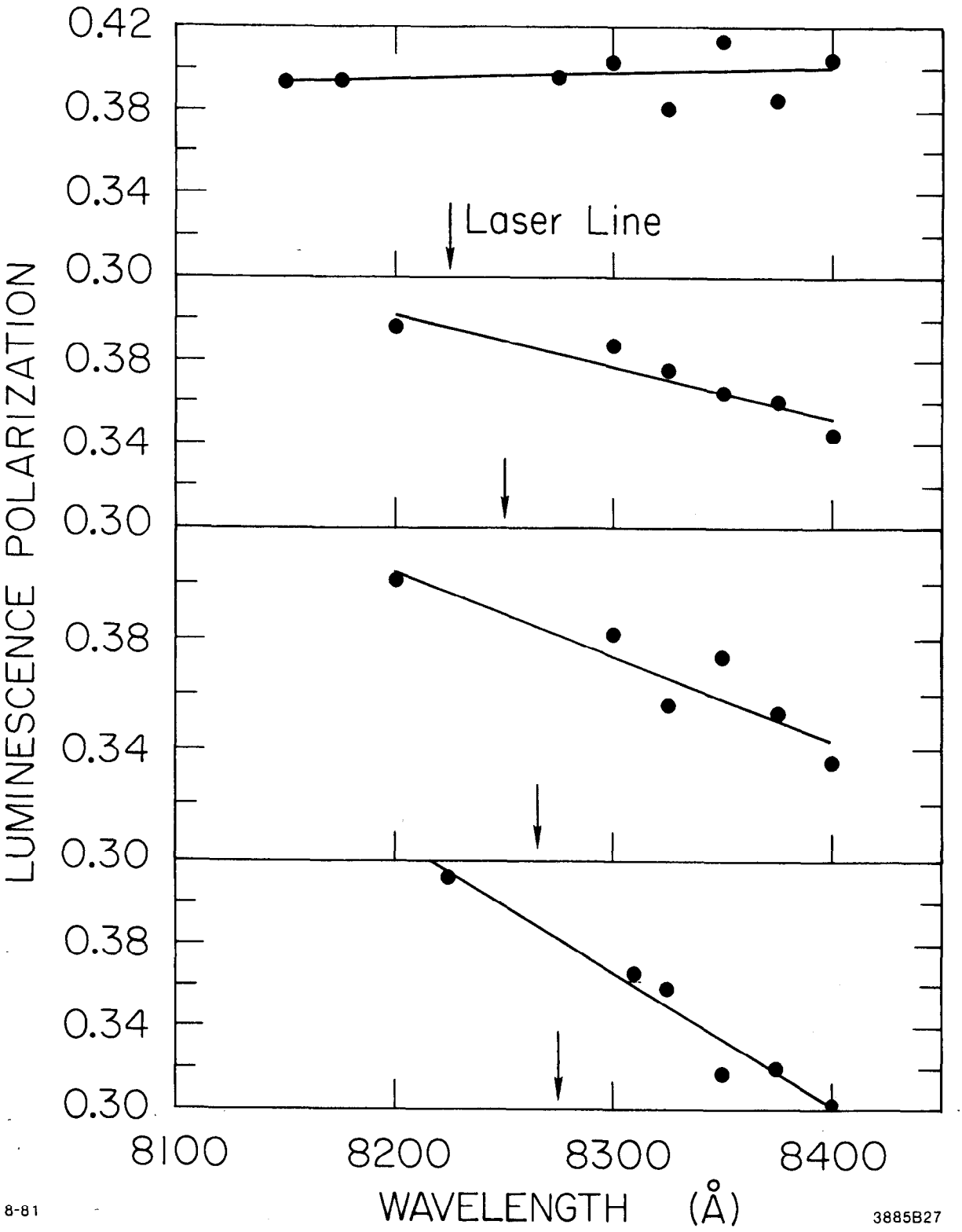

Fig. 5.11. Spectral dependence of luminescence polarization at high stress for several laser wavelengths (the luminescence peak is at ≃ 8300Å).

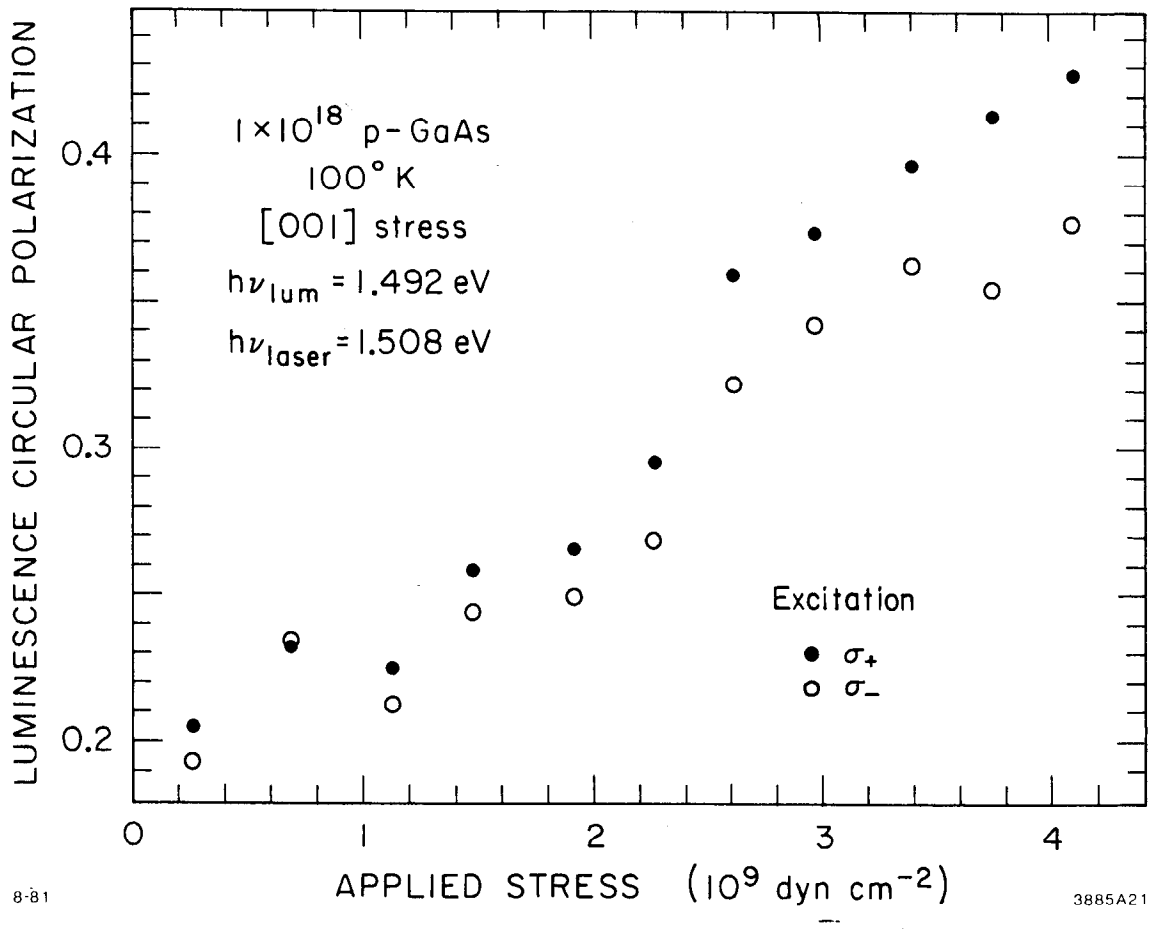

Fig. 5.12. Stress dependence of circular polarization at the luminescence peak for optical pumping at 8220Å. Open circles, σ_+ excitation, filled circles, σ_- excitation.

5.4. Spin Polarization Analysis of Polarized Luminescence

5.4.1. Approach

The recorded luminescence polarization data P_σ is, from Eq. (3.21), determined by the hole coupling constant P_h, the electron spin polarization P_s, and the spin relaxation factor $\tau_s/(\tau_s + \tau_r)$. From the dependence of P_σ on stress and laser and luminescence wavelengths the maximum value of P_s can, with certain assumptions and approximations, be extracted. In the following sections these conditions are discussed with the supporting data.

5.4.2. Spin relaxation

Given the omission of Hanle magnetic depolarization measurements[60,61] from what has been an exploratory study, the spin relaxation factor must be assumed to be independent of applied stress. The validity of this assumption may depend on which spin relaxation mechanisms are important for the doping and temperature regime of interest in this experiment. The two most important mechanisms for the parameter values of $p = 1 \times 10^{18}$ cm^{-3} and $T = 100^{o}$K are:

(a) the exchange interaction between electrons and holes, i.e. the Bir-Aronov-Pikus (BAP) mechanism,[62] and

(b) relaxation due to the k^3-spin splitting of the conduction band in III-V compounds, the D'yakonov-Perel' (DP) process.[7]

In the BAP mechanism the spin relaxation rate $\tau_s^{-1} = p_o \sigma v_{av}$, in which p_o is the hole density, σ is an exchange cross section, and v_{av} is the average electron velocity, is expected to depend to first order on p_o which is unaltered by the application of stress in a degenerately doped sample. However, the spin exchange cross section may have a large

dependence on the wave function of the states occupied by the holes, which are significantly changed by a large stress. The DP process should be relatively insensitive to stress since the structure of the conduction band is only slightly affected.[17] With this caveat, the spin relaxation factor obtained from the value of P_σ for $h\nu_{laser} < 1.510$ eV at zero stress is

$$\frac{\tau_s}{\tau_s + \tau_r} = \frac{P_\sigma}{0.25} = 0.80 \pm 0.04 \quad . \tag{5.16}$$

The error in this value is determined by the error in measuring P_σ.

5.4.3. Hole coupling factor

From the luminescence lineshapes of both stressed and unstressed samples the thermal hole distribution was observed to be unchanged by the photon energy of the laser light. Therefore, for the experimental conditions of Fig. 5.10, the hole energy distribution was completely characterized by the temperature, doping density, and the density of states. Furthermore, the spectrum of linearly polarized luminescence at high stress (Fig. 5.5b) demonstrates that the majority of holes occupy the edge of the light-hole band. The function $P_h(E_k)$ is therefore taken to be given Eq. (3.17a), where E_k is the hole kinetic energy. Finally it is noted that P_σ is uniform over the luminescence band in both unstressed and stressed samples (aside from secondary effects due to luminescence self absorption which are discussed in the following section). This leads to the assumption that the holes can be characterized by a single kinetic energy value E_k. Such an assumption would clearly be unreasonable for recombination between parabolic bands in which, for a given luminescence photon energy $h\nu$, the hole kinetic energy would

have the value

$$E_k = \frac{m_c^*}{m_c^* + m_v^*} (h\nu - E_g) \quad . \tag{5.17}$$

However, the exponential absorption edge indicates the presence of band tails which have the effect of smearing the energy of states in the edge of the bands. Several models[63-65] attribute band tailing in semiconductors with impurity concentrations $\simeq 1 \times 10^{18}$ cm^{-3} to a spatial fluctuation of the band edges. The valence band edge is considered to be a function of position $E_v(r)$. Figure 5.13 illustrates a model of spatially varying band edges and the band tails produced on the densities of states. Averaging over a macroscopic volume results in a bandtail density of states which is the sum of parabolic density of states functions starting at different energies within a range V_{rms} which characterizes the rms amplitude of the fluctuations in $E_v(r)$. In this case the hole kinetic energy can be written

$$E_k = \left\{ \left[\frac{m_c^*}{m_c^* + m_v^*} (h\nu - E_g) \right]^2 + V_{rms}^2 \right\}^{1/2} \quad . \tag{5.18}$$

Since for luminescence photons $h\nu \simeq E_g$, and $m_c^* << m_v^*$, E_k can be approximately set equal to V_{rms} to obtain the hole coupling factor

$$P_h = P_{s2}\left(\delta_s / V_{rms}\right) \quad . \tag{5.19}$$

5.4.4. Electron spin polarization

The electron spin polarization produced by the laser photon of energy $h\nu$ is given by

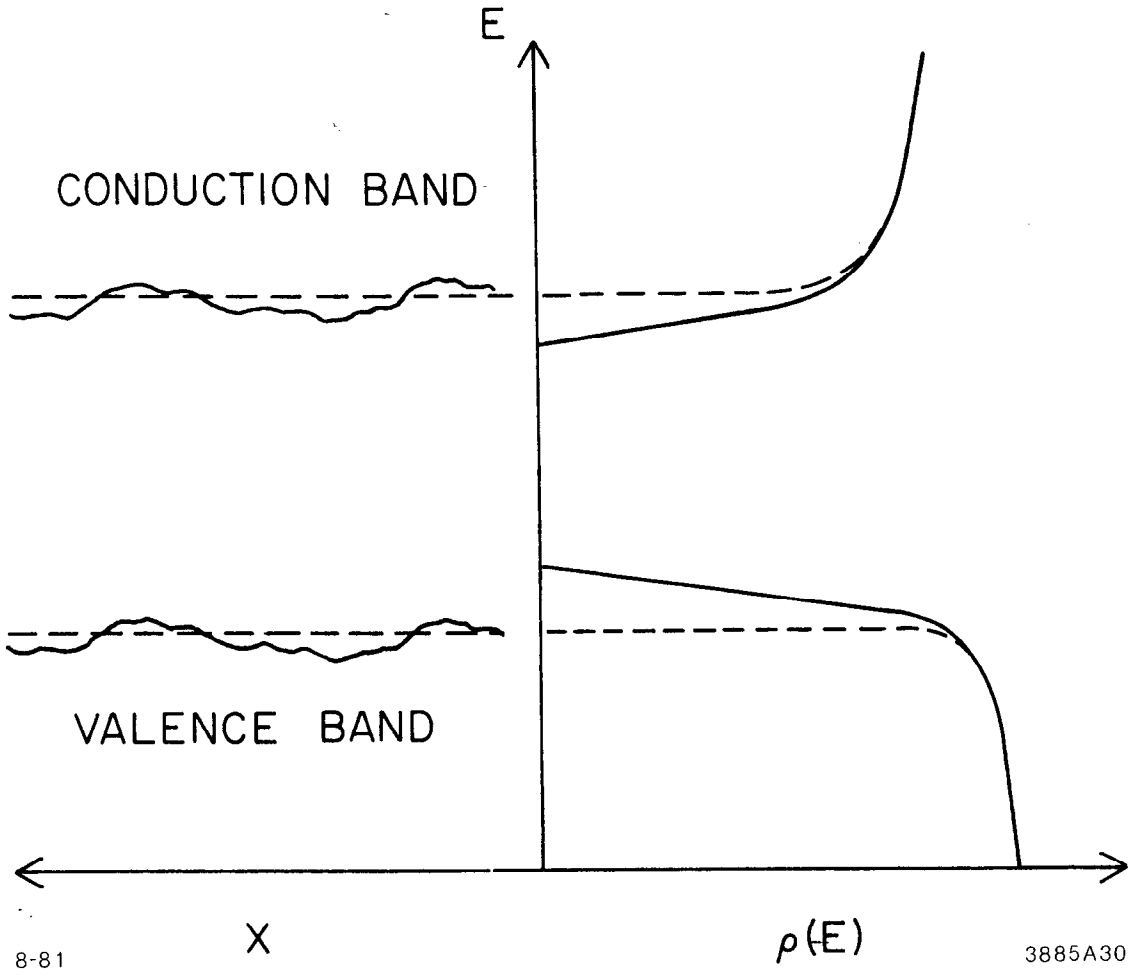

Fig. 5.13. Model of spatially fluctuating band edges due to ionized impurities and the resulting density of states band tails.

$$P_s(h\nu) = \frac{N_1(h\nu)\ P_{s1}(h\nu) + N_2(h\nu)\ P_{s2}(h\nu)}{N_1(h\nu) + N_2(h\nu)} \tag{5.20}$$

where superscripts (1) and (2) refer to electrons excited from states in the lower V_1 valence band and upper V_2 valence band, respectively. The dependence of the individual spin polarization functions on $h\nu$ is given by Eqs. (3.17a) and (3.17b) in which the expression for E_k is the same as Eq. (5.18) but $h\nu$ now refers to the laser light.

It can easily be shown that the relative values of the electron populations are given by

$$\frac{N_1(h\nu)}{N_2(h\nu)} = \frac{\alpha_1(h\nu)}{\alpha_2(h\nu)} \quad . \tag{5.21}$$

The absorption coefficient α_n between valence band V_n and the conduction band can be written

$$\alpha_n(h\nu) = \frac{q^2 |d|^2}{2\varepsilon_o m^2 C\nu} \int_{-\infty}^{\infty} \rho_c(E')\ \rho_v(E'')\ \left[f(E'')-f(E')\right]\ \delta\left(E'-E''-h\nu\right)\ dE' \tag{5.22}$$

where d is the interband dipole matrix element, ρ_c and ρ_v are the density of states functions for the conduction and valence bands, and f is the Fermi-Dirac function given by

$$f(E) = \left(\exp\left[(E-F)/kT\right] + 1\right)^{-1} \quad . \tag{5.23}$$

For a parabolic band (i.e. one with ellipsoidal energy surfaces) the density of states function is[66]

$$\rho_{pb}(E) = (2\pi^2)^{-1} \left(\frac{2m_v^*}{\hbar^2}\right)^{3/2} (E_v - E)^{1/2} . \qquad (5.24)$$

In the Kane bandtail model the density of states is represented by[55]

$$\rho_{bt}(E) = (2\eta)^{1/2} \left(\frac{m_v^*}{\pi\hbar^3}\right)^{3/2} y[(E_v - E)/\eta] \qquad (5.25a)$$

where

$$\eta = \sqrt{2}\, V_{rms} \qquad (5.25b)$$

and

$$y(x) = \frac{1}{\sqrt{\pi}} \int_{-\infty}^{\infty} (x-z)^{1/2} \exp(-z^2)\, dz . \qquad (5.25c)$$

The form of ρ_{bt} approximates ρ_{pb} at high energies and has the Gaussian form $\exp[(E_v - E)^2/\eta_c^2]$ at low energies.

The ability to make use of Eqs. (5.20)-(5.25) for a numerical calculation of $N_1(h\nu)$ and $N_2(h\nu)$ is severely limited in the present problem by the presence of strain. The bandtail model requires knowledge of the effective mass, but in the present situation the valence band effective masses are not constant with respect to energy. At the band edge we have shown in Eq. (2.21) that $m_{v1} = m_{v2} = 0.16$ m. In the high energy regime, $m_{v2}^* = 0.087$ m and $m_{v1}^* = 0.42$ m. The energy dependence of m_v^* for the parabolic case can in principle be numerically calculated from the constant energy surfaces defined by Eq. (2.17). Letting V(E) be the volume in $\vec{k}$-space enclosed within a constant energy surface E(k) = E, the density of states and the effective mass are given by

$$\rho(E) = \frac{1}{4\pi^3} \frac{dV}{dE} \tag{5.26a}$$

and

$$m^*(E) = \frac{\hbar^2}{2E} \left(\frac{3V(E)}{4\pi} \right)^{2/3} . \tag{5.26b}$$

Similar calculations have been performed for strained crystals of lightly doped Ge and Si, in which bandtailing is not significant, in connection with electron-hole droplet formation.[67] However, for heavy doping the choice of the appropriate value of m_v^* for linking ρ_{bt} to ρ_{pb} in a stressed crystal has not been addressed in the literature, and we did not attempt to apply the bandtail model quantitatively.

Although a detailed calculation of $P_s(h\nu)$ has not been done, Eqs. (5.20) and (5.21) can be used in combination with the absorption coefficient calculated from the luminescence lineshape to estimate the behavior of $P_s(h\nu)$. The absorption in Fig. 5.2 is the sum of $\alpha_{v1}(h\nu)$ and $\alpha_{v2}(h\nu)$ at zero stress. The two components of absorption contribute in the proportion $\alpha_{v1}:\alpha_{v2} = (m_{v1}^*)^{3/2}:(m_{v2}^*)^{3/2}$. The values of the zero stress effective masses give the well known result that the light hole band contributes roughly 1/3 of the total absorption.

Under stress, the band edges and their corresponding absorption edges split by δ_s. The α_{v1} and α_{v2} components are modeled in Fig. 5.14 by drawing the calculated absorption edge from Fig. 5.2 and replicating it with an energy shift of δ_s. The α_{v2} edge is the curve at lower energy. A qualitative correspondence can be made between the features of Fig. 5.10 and the labeled regions of Fig. 5.14. Segment (a) corresponds to the high energy portion of Fig. 5.10 where $\alpha_{v2} \simeq \alpha_{v1}$ and P_{s2}

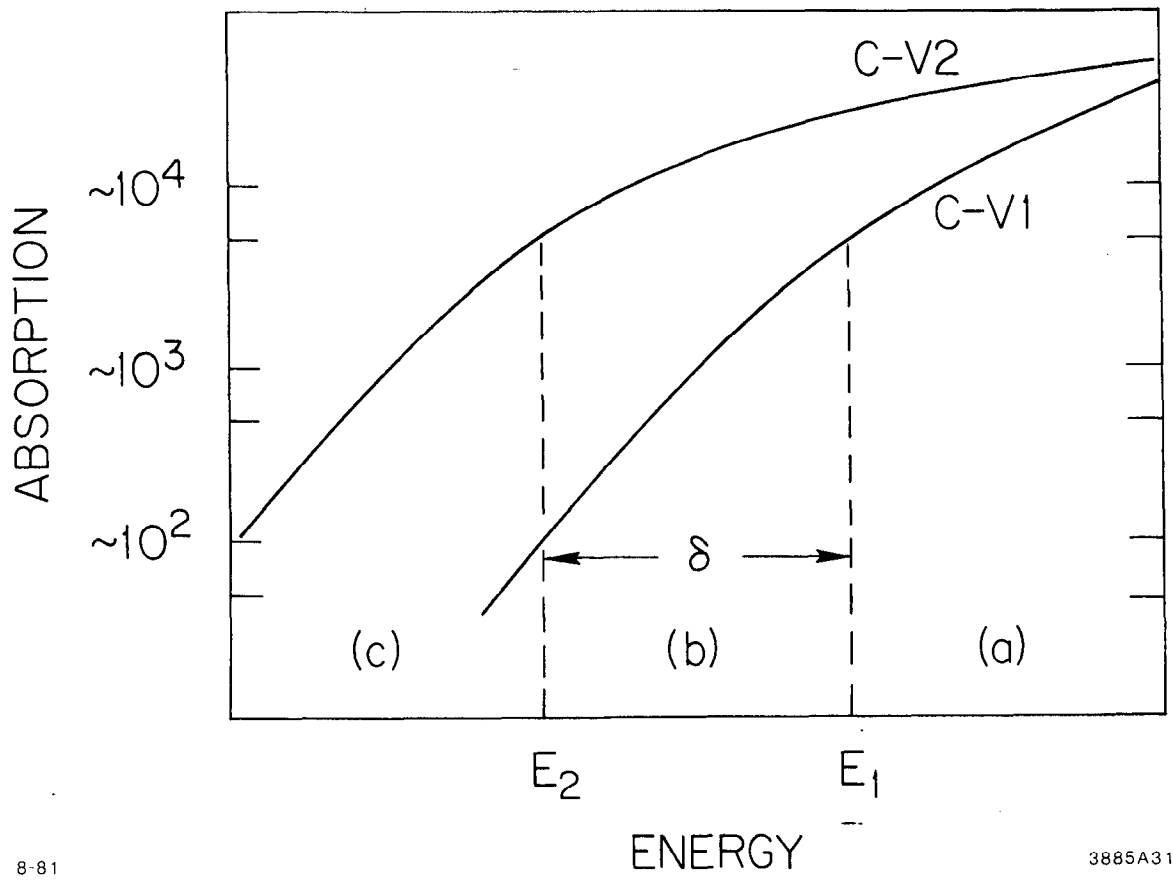

Fig. 5.14. Model of stress-split absorption edges.

and P_{s1} are near the zero stress limit $\delta_s/E_k << 1$. Point E_1 corresponds to the minimum in Fig. 5.10 near 1.532 eV, where P_{s1} approaches the value $P_{s1}(\delta_s/V_{rms})$. Below point E_1, α_1 falls exponentially and P_{s2} approaches the value $P_{s2}(\delta_s/V_{rms})$. At the point E_2, $N_2 >> N_1$. This point corresponds to the maximum of Fig. 5.10. Using Eq. (5.21), the value of P_s is taken to be given by $P_{s2}(\delta_s/V_{rms})$ at this point. The deep bandtail region (c) corresponds to the rolloff in Fig. 5.10 and is attributed to secondary effects associated with detecting spin polarization by luminescence which are discussed in Sec. 5.6.

We therefore argue that the observed polarization data and the above physical interpretation are consistent with the following assumed relation between P_σ and P_s for band edge optical pumping:

$$P_\sigma(h\nu) = 0.80 \left[P_{s2}(h\nu_{max})\right]^2 \qquad (5.27)$$

where the numerical coefficient 0.80 is the value of the spin relaxation factor. The "band edge" condition applies when $h\nu_{laser}$ is tuned to within $\simeq V_{rms}$ of E_g. We note that Eq. (5.27) is analogous to the well-known relation between P_σ and P_s for the unstressed case in which $P_h = P_s = 0.5$. The P_σ data points for each stress value were taken from Fig. 5.12 and averaged with respect to laser polarization; values for P_{s2} were then calculated from Eq. (5.27). The results are plotted in Fig. 5.15 along with theoretical curves for P_{s2} from Eq. (3.17a). In that equation we used $\theta = 90^o$ for the angle between the pump beam and the stress axis. Curves for several values of the parameter E_k are shown.

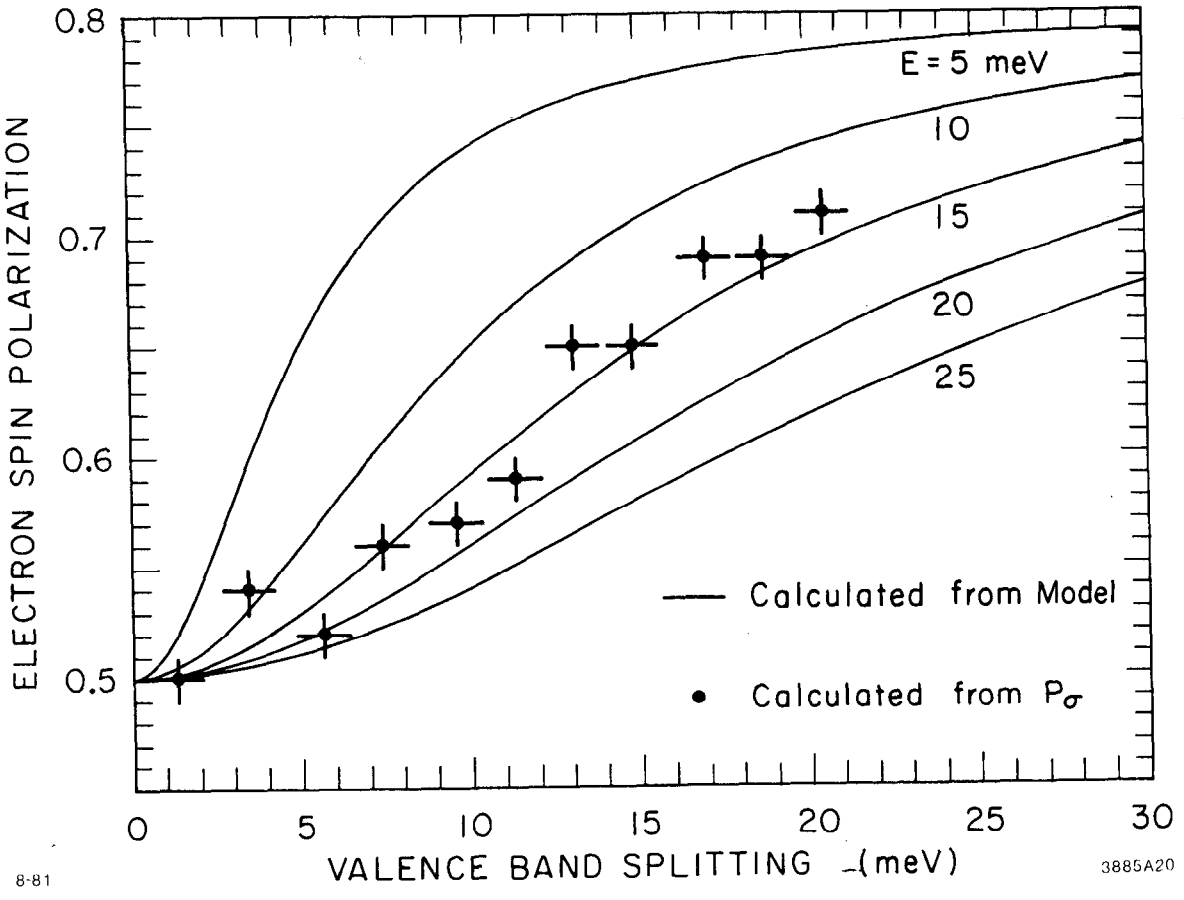

Fig. 5.15. Spin polarization calculated from luminescence polarization data and theoretical spin polarization curves for several values of the kinetic energy parameter of Eq. (3.17a).

5.5. Calculation of V_{rms}

The physical mechanism for the creation of bandtails may be due to one of several causes:[68] (a) formation of impurity bands, (b) local strains due to the accomodation of impurities which locally increase the energy gap (compressions) or decrease it (dilations), and (c) fluctuations in the Coulomb potentials of ionized impurities which are randomly distributed on lattice sites.

Casy and Stern[55] have obtained good agreement between calculated and measured room temperature absorption spectra of 1×10^{18} p-type GaAs by using the Kane bandtail model which assumes V_{rms} is due to mechanism (c) above. Mechanisms (a) and (b) are apparently not significant for Zn impurities at this concentration.

When the potential fluctuations arise from ionized impurities, the rms potential energy fluctuation is given by[64]

$$V_{rms} = \frac{q^2}{4\pi\varepsilon} \left[\left(N_a^- + N_d^+ \right) 2\pi L_s \right]^{1/2} \tag{5.28}$$

where N_a^- and N_d^+ are the ionized acceptor and donor concentrations and L_s is the screening length. The expression for the classical Debye screening length is[69]

$$L_s = \left[\frac{kT\varepsilon}{q^2 p} \right]^{1/2} . \tag{5.29}$$

The ionization energy for Zn acceptor impurities in GaAs has been shown to go to zero for $N_a = 1 \times 10^{18}$ cm^{-3}. In this case the hole population is degenerate and independent of the temperatue. Accordingly,

we take $p = N_a = 1 \times 10^{18}$. Taking $\varepsilon/\varepsilon_o = 13.1$ for GaAs,[70] the calculated values for Eqs (5.28) and (5.29) for T = 100°K are $L_s = 25 \times 10^{-8}$ cm and $V_{rms} = 0.014$ eV. This result is clearly very consistent with the value of the kinetic energy parameter obtained by fitting the slope of the experimental P_s vs stress data to the model function $P_{s2}(\delta_s/E_k)$. A least squares fit of the data gave a parameter value of $E_k = 0.017$ eV.

5.6. Effect of Self Absorption on the Polarization of Photoluminescence

The van Roosbroeck-Shockley relation Eq. (5.1) neglects the importance of self absorption on the spectrum of photoluminescence emitted from the sample surface. The generalization of Eq. (5.1) that takes self absorption into account is given by[71]

$$I(h\nu) = K\alpha_o \left(\frac{8\pi n^2}{h^3 c^2}\right)(h\nu)^2 \exp\left(-\frac{h\nu}{kT}\right) \alpha(h\nu) \times \frac{\left[\frac{S}{D} + L^{-1} + \alpha_o + \alpha(h\nu)\right]}{\left[\frac{S}{D} + L^{-1}\right]\left[\alpha_o + \alpha(h\nu)\right]\left[\alpha(h\nu) + L^{-1}\right]} \qquad (5.30)$$

where K is a proportionality constant, S/D is the ratio of the surface recombination velocity to the diffusion constant, and L is the diffusion length (not to be confused with the screening length L_s). α_o is the absorption coefficient for the excitation light, and $\alpha(h\nu)$ is the absorption coefficient of the re-emitted light of frequency ν. In the present case $S/D > 10^5$ cm^{-1} and $L \simeq 10^{-4}$ cm.

Several remarks about Eq. (5.30) are in order. The photoexcited minority carriers (electrons in this case) will diffuse from the point of creation before recombination with majority carriers (holes) which

are assumed to have a uniform depth distribution in the sample. If $\alpha_o >> L^{-1}$, the mean recombination depth is $\simeq L$, and the self absorption will be independent of α_o. On the other hand if $\alpha_o << L^{-1}$, the recombination depth will be $\simeq \alpha_o^{-1}$ and the amount of self absorption will be α_o dependent. Another related feature is that photons in the emission spectrum at a frequency corresponding to large $\alpha(h\nu)$ come only from close to the surface. Photons corresponding to small $\alpha(h\nu)$ come from deeper in the sample as well. It is proposed that these features can have a significant effect on the circular polarization of photoluminescence in stressed GaAs when the laser and luminescence are such that the luminescence lies in a portion of the spectrum where self absorption occurs. The splitting of the valence bands means that the absorption from the V_2 band will be greater than that of the V_1 band for any given laser wavelength near the band gap, i.e., $\alpha_s(h\nu) >> \alpha_1(h\nu)$. When $h\nu_{laser}$ is sufficiently close to E_g that $\alpha(h\nu) << L^{-1}$ then at the time of recombination the electrons produced from the V_1 band will still have a deeper profile into the crystal than those from the V_2 band. In the luminescence spectrum more photons with low $h\nu$ will come from recombination of N_1 electrons which have lower spin polarization than N_2 electrons. The hole distribution will be nearly uniform with respect to depth into the crystal since it is assumed that $\Delta p << p_o$. Thus, the luminescence polarization can be expected to fall in the long wavelength tail when the pump laser is tuned to values of absorption that are much less than L^{-1}. Furthermore the size of the effect should increase as α_{v1} and α_{v2} are reduced and the moments of the distributions $N_1(z)$ and $N_2(z)$ become more unequal due to the diminished effect of diffusion.

This mechanism is in qualitative agreement with the data of Fig. 5.11 which shows a progressively steeper falloff in the long wavelength luminescence polarization as the laser is tuned toward lower absorption. The luminescence wavelength at which the data in this plot was recorded was set at approximately the peak of the luminescence band in the stressed crystal.

Chapter VI

CONCLUSIONS

6.1. Polarization vs Stress Operating Curves

It has been shown that the proposed model for the stress dependence of the electron spin polarization for band edge optical pumping fits the observed data when the kinetic energy parameter is taken as the rms potential energy fluctuation of the spatially dependent band edges due to ionized impurities. The expression for V_{rms} given in Eq. (5.28) in terms of only the doping, temperature, and dielectric constant can be substituted for E_k in Eq. (3.17) to calculated polarization vs stress operating curves. The results are presented in Fig. 6.1 for the configuration of compressive stress at 90^o the pumping beam axis [using Eq. (3.17a)] and in Fig. 6.2 for tensile stress parallel to the pump axis [using Eq. (3.17b)]. The impurity concentrations given include the value used in the data given in this work and three other values representative of high doping requirements for spin polarized photocathodes. To calculate these curves it was assumed that $N_a^- = p = N_a$ independent of temperature and that L_s is given by the Debye length Eq. (5.29) throughout the temperature range shown. It is also emphasized that the calculated spin polarization values do not include a spin relaxation factor.

We point out that a tensile stress parallel to the pump beam leads to a higher spin polarization for a given stress, then does compressive stress at 90^o to the pump beam, with an infinite stress polarization

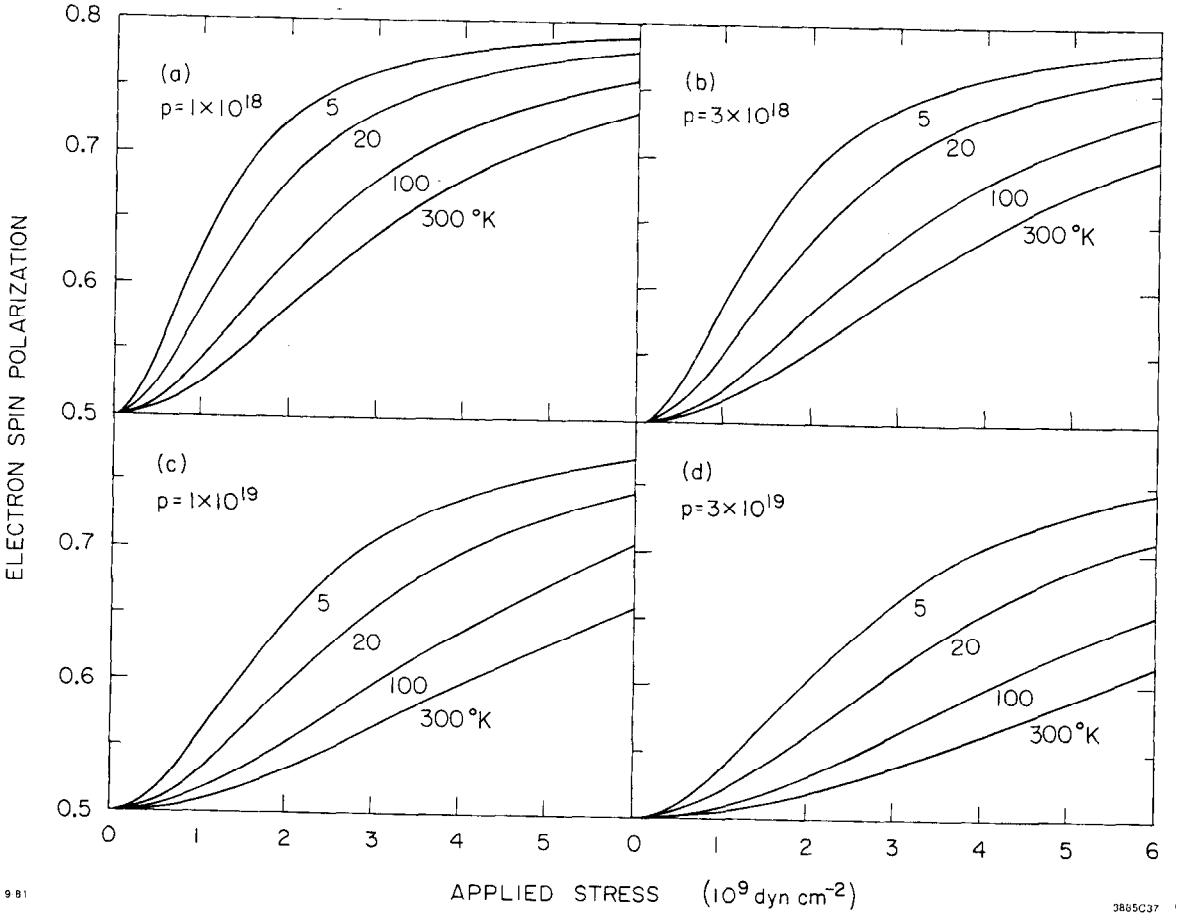

Fig. 6.1. Spin polarization vs compressive stress for band edge optical pumping at 90° to the stress axis.

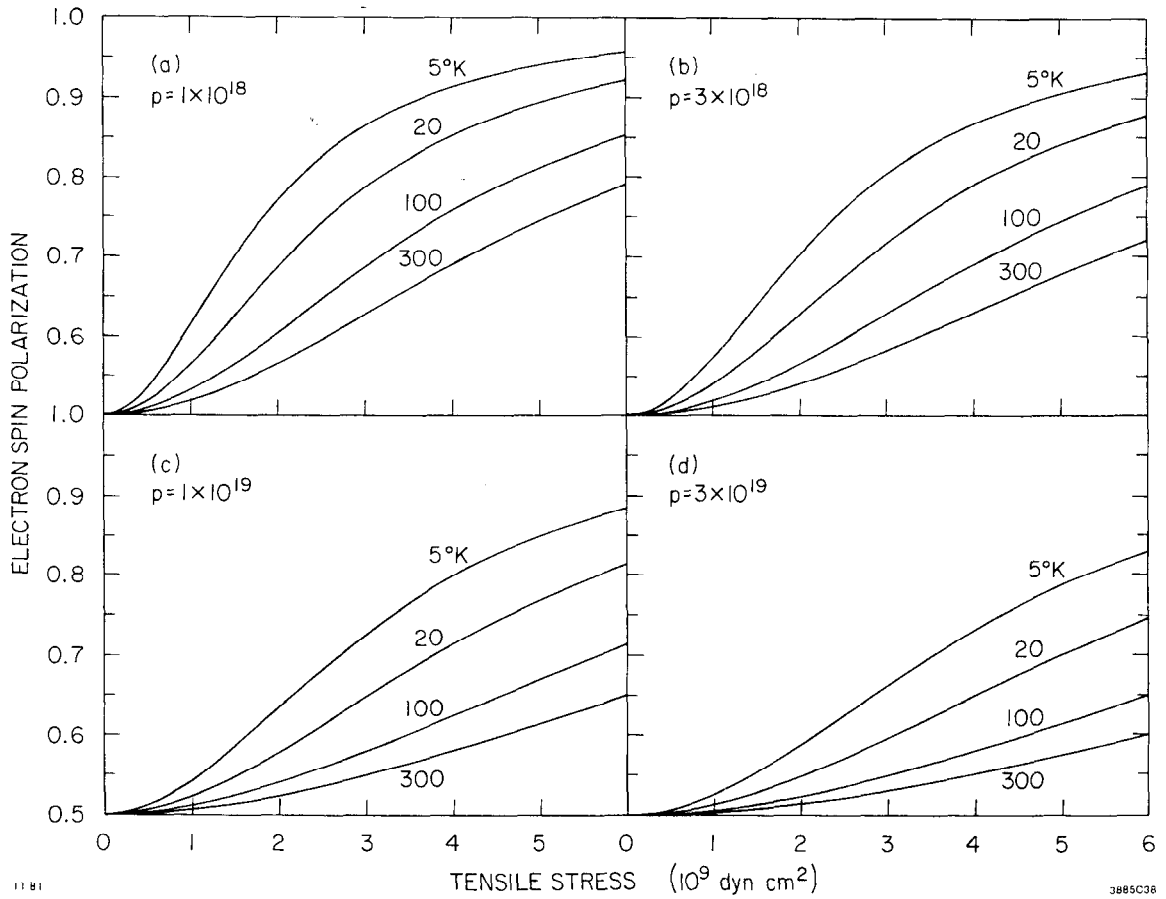

Fig. 6.2. Spin polarization vs tensile stress for band edge optical pumping parallel to the stress axis.

limit of 100%. This condition could be achieved in a geometry suitable for photoemission with the use of certain epitaxial films of III-V ternary or quartenary compounds on GaAs substrates. In these heterostructures a uniform two-dimensional stress in the film plane results from the thermal lattice mismatch between the film and the substrate as they are cooled from the growth temperature. This planar stress is equivalent to a uniaxial stress normal to the film surface. The stress can be either compressive or tensile depending on the film composition.[75] Optical pumping and photoluminescence measurements have recently been reported for GaInP and GaInAsP epitaxial films.[76] However, no determination of spin polarization stress dependence was given.

With regard to the range of validity for the assumptions underlying the calculation of V_{rms}, difficulties would be most likely to arise at low temperature. The high temperature classical expression for L_s which decreases with T eventually gives way to a low temperature limit. An expression for the low temperature screening length is given by[50]

$$L_s = \left(\frac{\pi\epsilon\hbar^2}{m^* q^2}\right)^{1/2} \left(\frac{\pi}{3p}\right)^{1/6} . \qquad (6.1)$$

The delimiting point between the two screening length regimes is the degeneracy temperature T_{deg} which is given by[72]

$$T_{deg} = \left(\frac{3}{\pi}\right)^{3/2} \frac{h^2}{8k_B m^*} p^{2/3} \qquad (6.2)$$

to compare this limit with the conditions of the present experiment, taking $m^* = 0.5$ m, values of 84^o for T_{deg} and 18Å for the low temperature screening length are obtained. For comparison at 100^oK, the Debye

length is 25Å. The sample was near the low temperature screening range by this criterion. It is also noted that at $N_a = 1 \times 10^{18}$ cm^{-3} the samples are mildly degenerate in the sense that the ionization energy is very small but not precisely known. A reduction in p below N_a may therefore occur at sufficiently low temperature. These two complications to the assumptions of constant p and classical screening will tend to offset each other, however, possibly permitting extension of the model for V_{rms} to lower temperature than would be valid for each assumption separately. Experimental support for this argument exists in the following sense. Since V_{rms} is a measure of the width of the bandtails it also determines the slope of the exponential absorption edge. It was pointed out in Sec. 5.1.2 that the absorption edge calculated from photoluminescence agreed with direct absorption measurements by Redfield and Afromowitz.[56] Those measurements, which covered the temperature range of 300°K to 5°K, show a steadily steepening edge with decreasing T. Although it would be impractical to extract the temperature dependence of V_{rms} from their published absorption curves, it encourages the use of the simple V_{rms} expression in the spin polarization model below T_{deg}. Note that the possible necessity of modifying the expression for V_{rms} does not of itself invalidate the use of the correct value of V_{rms} for the kinetic energy parameter in the expression for the spin polarization.

It is likely that the greatest interest in the operating curves will be to estimate the performance of a cathode material that is more heavily doped than 1×10^{18} cm^{-3}. For this application there is also a word of caution. Not only will T_{deg} rise with impurity concentration,

cutting off the drop in L_s with lower T, but the Fermi level will move deeper into the valence band as N_a increases in order to maintain charge neutrality between holes and ionized acceptors. A condition may occur in which the upper stress-split valence band edge, which under optical pumping would produce an enhanced spin polarization, is significantly depleted of electrons that were contributed to the impurities. Calculation of the Fermi level is complicated by the condition of degeneracy caused by heavy doping, by the stress-induced energy dependence of the effective mass, and by the presence of bandtails which alter the parabolic density of states in the vicinity of substantial hole population. It is not obvious which of the last two effects is more significant or whether both should be included in the next round of analysis. The position of the Fermi level, the shape of the bandtails, and the screening length are all connected through V_{rms}. It is clear that a comprehensive calculation of the hole distribution in the presence of a uniaxial stress in a heavily doped semiconductor must be a self-consistent, iterative approach.

REFERENCES

1. R.R. Parsons, Phys. Rev. Lett. 20, 1152 (1969).
2. E.L. Garwin, D.T. Pierce and H.C. Siegmann, Helv. Phys. Acta. 47, 343 (1974).
3. D.T. Pierce and F. Meier, Phys. Rev. B13, 5484 (1974).
4. D.T. Pierce et al., Rev. Sci. Instrum. 51, 478 (1980).
5. P. Zürcher and F. Meier, J. Appl. Phys. 50, 3687 (1979).
6. W.E. Spicer, Phys. Rev. 112, 114 (1958).
7. M. Erbudak and B. Reihl, Appl. Phys. Lett. 33, 584 (1978).
8. G. Lampel and M. Eminyan, the 15th International Conference of Physics Semiconductor, Kyoto (1980).
9. M.I. D'yakanov and V.I. Perel', Sov. Phys. JETP 33, 1053 (1971).
10. M.I. D'yakanov and V.I. Perel', Sov. Phys. Semicond. 1, 1551 (1974).
11. G. Dresselhaus, A.F. Kip and C. Kittel, Phys. Rev. 98, 368 (1955).
12. E.O. Kane, J. Phys. Chem. Solids 1, 249 (1957).
13. E.O. Kane, Semiconductors and Semimetals, (R.K. Willardson and A.C. Beer, eds.), Vol. I, Academic Press, New York, 1966.
14. P.-O. Löwdin, J. Chem. Phys. 19, 1396 (1951).
15. O. Madelung, Physics of III-V Compounds, John Wiley and Sons, New York (1964), p. 352.
16. H. Ehrenreich, J. Appl. Phys. 32, 2155 (1961).
17. W. Howlett and S. Zukotynski, Phys. Rev. B16, 3688 (1977).
18. G.E. Pikus and G.L. Bir, Sov. Phys. Solid State 1, 1502 (1959).

19. J.F. Nye, Physical Properties of Crystals, Oxford University Press, London (1964), p. 99.

20. F.H. Pollak and M. Cardona, Phys. Rev. 172, 816 (1968).

21. M. Chandrasekhar and F.H. Pollak, Phys. Rev. B 15, 2127 (1977).

22. W.A. Brantley, J. Appl. Phys. 44, 534 (1973).

23. M.S. Skolnick et. al., J. Phys. C: Solid State Phys. 9, 2809 (1976).

24. P. Lawaetz, Phys. Rev. 4, 3460 (1971).

25. J.C. Hensel and G. Feher, Phys. Rev. 129, 1041 (1963).

26. R.H. Pantell and H.E. Puthoff, Fundamentals of Quantum Electronics, John Wiley and Sons, New York (1969), p. 11.

27. Morgan Semiconductor, Garland, Texas,75041.

28. W. Kern, RCA Review 39, 278 (1978).

29. Gryphon Corp., Burbank, CA 91503.

30. Abrasives Unlimited, San Leandro, CA 94577.

31. Bay Cities Tool and Supply, Newark, CA 94560.

32. Hyspan Precision Products, San Diego, CA 92102.

33. R.N. Bhargava and M.I. Nathan, Phys. Rev. 161, 695 (1967).

34. The Stanford Two-Mile Accelerator, R.B. Neal, ed.,W.A. Benjamin, New York, 1968.

35. C.Y. Prescott et al., Phys. Lett. 77B, 347 (1978).

36. Designed after J. Jethwa and F.P. Schäjer, Appl. Phys. 4, 299 (1974).

37. N. Fletcher, Appl. Phys. 22, 231 (1980).

38. T.W. Hansch, Appl. Opt. 11, 895 (1972).

39. A. Passner and T. Venkatesan, Rev. Sci. Instrum. 49, 1413 (1978).

40. Precision Cells, Hicksville, NY 11801.

41. Micropump, Concord, CA 94524.

42. Balston Filter Products, Lexington, MA 02173.

43. Exciton Chemical Corporation, Dayton, OH 45431.

44. W. Shurcliff, Polarized Light, Oxford University Press, London (1962), p.25.

45. M. Born and E. Wolf, Optics, 4th Ed., Permagon Press, London (1970), p. 40.

46. P.Y. Yu, M. Cardona, and F. Pollak, Phys. Rev. B 3, 340 (1971).

47. Evans Associates, P.O. Box 5055, Berkeley, CA 94705.

48. W. van Roosbroeck and W. Shockley, Phys. Rev. 94, 1558 (1954).

49. C.M. Chang, Stanford University Thesis, 1964 (unpublished).

50. H.C. Casey and M.B. Panish, Heterostructure Lasers, Part A., Academic Press, New York, 1978.

51. H. Kressel and J.K. Butler, Semiconductor Lasers and Heterostructure LED's, Academic Press, New York, 1977.

52. J. Vilms and W.E. Spicer, J. Appl. Phys. 36, 2815 (1965).

53. A.N. Titkov, V.I. Safarov, and G. Lampel, Proc. 14th Int. Conf. Phys. Semicond., Edinburgh, 1978.

54. H.C. Casey and M.B. Panish, op. cit., Part B.

55. H.C. Casey and F. Stern, J. Appl. Phys. 47, 631 (1976).

56. D. Redfield and M.A. Afromowitz, Appl. Phys. Lett. 11, 138 (1967).

57. Y.P. Varshni, Physica 34, 149 (1967).

58. B.I. Zakharchenya et. al., Sov. Phys. Semicond. 13, 137 (1971).

59. E. Hecht and A. Zejac, Optics, Addison Wesley, Menlo Park, CA (1979), p. 269.

60. C. Hermann, Ann. Phys. t. 2, 5 (1977).

61. G. Fishman and G. Lampel, Phys. Rev. B 16, 820 (1977).

62. G.L. Bir, A.G. Aronov, and G.E. Pikus, Sov. Phys. JETP 42, 705 (1976).

63. V.L. Bonch-Bruevich, Semiconductors and Semimetals, (R.K. Willardson and A.C. Beer, eds.), Vol. I, Academic Press, New York (1966), p. 101.

64. E.O. Kane, Phys. Rev. 131, 79 (1963).

65. B.I. Halperin and M. Lax, Phys. Rev. 148, 722 (1966).

66. J.I. Pankove, Optical Processes in Semiconductors, Prentice-Hall, Englewood Cliffs, New Jersey (1971), p. 6.

67. L. Liu, Sol. St. Comm. 25, 805 (1978).

68. J.I. Pankove, Phys. Rev. 140, 2059 (1965).

69. J.M. Ziman, Principles of the Theory of Solids, Cambridge University Press, London (1965), p. 131.

70. I. Strzalkowski, S. Joshi, and C.R. Crowell, Appl. Phys. Lett. 28, 350 (1976).

71. C.J. Hwang, J. Appl. Phys. 40, 3731 (1969).

72. W. Shockley, Electrons and Holes in Semiconductors, Van Nostrand, New York (1950), p. 242.

73. A.I. Ekimov and V.I. Safarov, JETP Lett. 12, 198 (1970).

74. B.I. Zakharchenya et al., JETP Lett. 13, 137 (1971).

75. H.C. Casey and M.B. Panish, Hetrostructure Lasers, Part B, Academic Press, New York, 1978.

76. I.N. Arsent'ev et al., Sov. Phys. Solid State 22, 1977 (1980).